

Polarization Measurements in Macro- and Micro-Raman Spectroscopies: Molecular Orientations in Thin Films and Azo-Dye Containing Polymer Systems

Claude Sourisseau*

Laboratoire de Physico-Chimie Moléculaire, LPCM, UMR 5803-CNRS, Université Bordeaux1, 351 cours de la Libération, 33 405 Talence, Cedex, France

Received October 28, 2003

Contents

1. Introduction and Theoretical Background	3851	4.1.1. Semitransparent Plate or Notch Filter	3873
1.1. Laboratory System Axes	3852	4.1.2. Objective Lens: How To Make the Best Choice?	3874
1.2. Molecular Reference System	3853	4.1.3. Strongly Absorbing Samples ⁴²	3875
1.3. Application to a Simple Case Example	3853	4.1.4. Weakly Absorbing Samples ⁴²	3876
2. Gas and Liquid Samples: Invariants of the Second-Order Raman Tensor	3854	4.2. Intensity Measurements with Transparent Samples	3876
2.1. Depolarization Ratio in "Linear" Experiments (ρ_{lin})	3854	4.2.1. General Intensity Expressions	3876
2.2. Three Invariants of the Raman Tensor	3854	4.2.2. Application of the Intensity Expression to a Liquid Sample	3878
2.3. "Average" Raman Intensities and Depolarization Ratios	3855	4.2.3. Radial and Axial Energy Distributions within the Objective Focal Plane ⁴⁴	3879
3. Crystalline and Amorphous Thin Films: Polarization Measurements in "Macro-Raman" Experiments	3855	4.3. Optical Principles and in-Depth Sectioning with a Confocal Instrument	3880
3.1. Series Expansion of the Orientation Distribution Functions in Uniaxial and Biaxial Systems	3856	4.4. Applications, Raman Images, and Calculation of the Order Parameters	3881
3.2. Application Examples in Systems of Uniaxial Symmetry	3857	4.4.1. Uniaxial Orientation in Azopolymer Diffraction Gratings	3881
3.2.1. Photoinduced Orientation in a DR1 Dye Doped Polymer Film ^{17–20}	3857	4.4.2. Photoinduced Biaxial Orientations in Strongly Absorbing Polymer Films	3886
3.2.2. Uniaxial Orientation in Stretched Polyethylene (PE) Films ^{21,22}	3859	5. Acknowledgments	3890
3.2.3. Correlation Diagrams of $\langle P_4 \rangle$ versus $\langle P_2 \rangle$ in Uniaxial Systems ^{12,23–25}	3862	6. Appendix: Mathematical Expressions for the $P_{00}(\cos \theta)$ and $P_{lm}(\cos \theta)$ Type Legendre Polynomials and Orientation Factors	3890
3.3. Application Examples in Systems of Biaxial Symmetry	3864	7. References	3890
3.3.1. Biaxial Orientation in a Poly(ethylene terephthalate) (PET) Film ^{11–13}	3864		
3.3.2. Values of the Order Parameters in a PET Film ^{11–13}	3866		
3.3.3. Estimates of the Direction Cosines	3866		
3.4. Deformation Schemes, Theoretical Considerations, and Applications of Direct Methods via Internal Calibrations ^{13,26–33}	3868		
3.4.1. Theoretical Considerations of the Deformation Schemes	3868		
3.4.2. Applications of Direct Methods via Internal Calibrations	3869		
4. Polarization Measurements in Confocal "Micro-Raman" Spectrometry	3873		
4.1. Coupling of an Optical Microscope—Experimental Considerations	3873		

1. Introduction and Theoretical Background

It is already well established that the knowledge and understanding of molecular orientational properties are very important in various domains of advanced material sciences. For instance, polymer fibers, liquid-crystal "smart" windows, phase or interferential or polarizing filters, holographic gratings, and electrical (ferro-) or optical (chiro-) switches are typical materials where the control of the molecular orientations does play a fundamental role in the measured properties and potential applications.

During these past decades, infrared (IR), Raman, and inelastic neutron scattering (INS) vibrational spectroscopies have been extensively used, and they are among the few nondestructive, very sensitive techniques which afford a lot of information at the molecular level: this stems from the inherent directional nature of the incident photons which are propagating along a fixed direction and are often

* E-mail address: c.sourisseau@lpcm.u-bordeaux1.fr. Phone: (33) 5 40 00 69 71. Fax: (33) 5 40 00 84 02.



Claude Sourisseau was born in Penne d'Agenais (France) in 1944. He graduated from Ecole Nationale Supérieure de Chimie Bordeaux on 1966 and received a Science Doctorate (Ph.D.) in Physical Sciences from University Paris VI in 1972. He received a CNRS position, first as research scientist in the Laboratory of Infrared and Raman Spectroscopies (LASIR) in Thiais (France) from 1966 to 1983. During this period, his main topics of investigation were the spectroscopic and dynamical properties of various inorganic and organometallic complexes, using FTIR, Raman, and neutron scattering techniques. For this purpose, he spent one year (1974–75) as research associate at University of Pittsburgh, PA, U.S.A., (in Prof. F. A. Miller's group) to record Raman spectra of gaseous organometallic complexes and another six month period at University College London, U.K., (in Prof. R. J. H. Clark's group) to investigate resonance Raman spectra of metal–metal bonded solid complexes. Then, he moved to the University of Bordeaux1, Talence (France), as director scientist and head of the Laboratory of Spectroscopies of Molecules and Crystals (LSMC) during 12 years (1984–1995). Now, he is currently senior researcher in the Laboratory of Molecular Physical-Chemistry (LPCM, UMR-5803) at the same university. His more recent areas of interest are the photo-physical, photoinduced, and orientational properties of chromophores, in particular of azobenzene dye doped or grafted copolymer systems, as studied from polarization measurements with UV–visible, FTIR, and macro- and micro-Raman (confocal) spectroscopies. He is also working on the mechanisms of formation, duplication, and erasing of holographic gratings inscribed on thin polymer films and, more recently, on their nonlinear (second-order) optical properties under high electric field poling conditions. He is a member of the editorial board of *Journal of Raman Spectroscopy* and of the International Steering Committee for the organization of the international conferences of Raman spectroscopies, ICORS.

polarized in the normal plane with respect to that direction; the transmitted or scattered photons are thus collected and selected in a precise direction. A correct understanding of the interaction mechanisms between the polarized beams and a measurement of the energy exchanges in absorption–reflection (IR) or in scattering (Raman, INS) processes are thus necessary to carry out such spectroscopic studies.

Here, our purpose will be first to recall some basic knowledge, concepts, and experimental cautions to keep in mind in order to perform precise macro- and micro-Raman polarized experiments and accomplish the related data treatments. Then, we shall concentrate on the most probable orientational molecular distribution functions and their construction from polarized Raman data obtained on thin films of macromolecular materials possessing either uniaxial or biaxial symmetry properties. As illustrative examples, we shall discuss some results for various macromolecular systems and azo-dye containing polymer films, with most results being extracted from literature data or from recent studies performed in

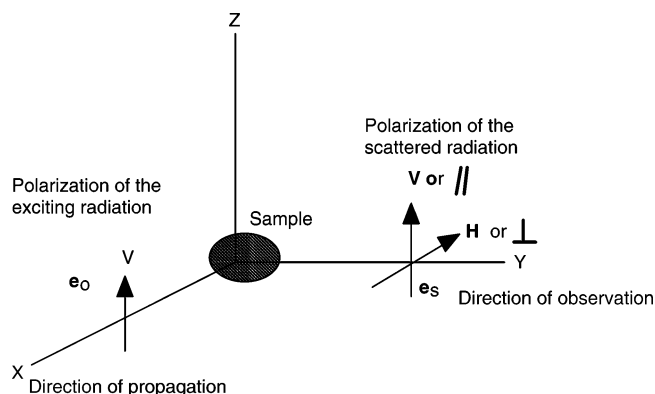


Figure 1. Traditional 90° geometry in Raman scattering.

our laboratory. In the former cases, the more important data will be extracted from macro-Raman experiments; they will be correlated with theoretical considerations about deformation schemes suggested in polymers. Also, it will be shown that direct spectroscopic methods using internal calibrations can be successfully applied to polymer systems of industrial interest. In the latter cases, emphasis will be put on the relative intensity and polarization measurements in micro-Raman spectrometry; also, the additional performances of a confocal Raman instrument will be underlined for the investigations of in-depth sectioning polymer structures and for the possibilities to perform new measurements with a quite reasonable radial resolution at a micron or submicron level, that is, at the diffraction limit.

According to Placzek (as early as 1934!) the collected intensity in Raman scattering is described by the general formula^{1–4}

$$I_{\text{Raman}(mn)} \approx KI_0 \sum_{ij} |(\alpha_{ij})_{mn}|^2 \approx KI_0 |\mathbf{e}_0 \boldsymbol{\alpha} \mathbf{e}_s|^2 d\Omega \quad (1)$$

where we have made use of the following simple notations: $K \approx CN_0(v_s)^4 \approx CN_0(v_0 \pm \Delta v_R)^4$ with N_0 the density in the scattering centers, $I_{\text{Raman}(mn)}$ is the scattered energy per unit time (intensity) collected within the solid angle $d\Omega$ for the vibrational transition from state m to state n , and I_0 is the energy per unit surface and time (irradiance) of the incident laser excitation on the sample. The unit vectors \mathbf{e}_0 and \mathbf{e}_s define respectively the direction cosines of the electric fields for the exciting and scattered radiations, and α_{ij} are the derivatives (with respect to the normal coordinates) of the molecular polarizability tensor elements due to the induced dipole in the interaction with the electromagnetic field. Note that the induced dipole is often written in matrix notation, $\boldsymbol{\mu} = [\boldsymbol{\alpha}]\mathbf{E}$, and that the boldface characters are here reserved only for vectors and matrices.

1.1. Laboratory System Axes

First, one must recall that the tensor expression is dependent on the coordinate system, and in the traditional “90° geometry” setup shown in Figure 1 we may write

$$K|\mathbf{e}_0\alpha\mathbf{e}_s|^2 = K \left\{ (001) \begin{pmatrix} \alpha_{XX} & \alpha_{XY} & \alpha_{XZ} \\ \alpha_{YX} & \alpha_{YY} & \alpha_{YZ} \\ \alpha_{ZX} & \alpha_{ZY} & \alpha_{ZZ} \end{pmatrix} \begin{pmatrix} 1 \\ 0 \\ 1 \end{pmatrix} \right\}^2 = K(\alpha_{ZX} + \alpha_{ZZ})^2 \quad (2)$$

Then, using an analyzer located on the scattered beam, we may discriminate between the polarizations,

either in the horizontal analysis,

$$I_{\text{Raman}} = K|\alpha_{ZX}|^2 = I_{\text{VH}} \text{ or } I_{\perp} \quad (3)$$

or in the vertical analysis,

$$I_{\text{Raman}} = K|\alpha_{ZZ}|^2 = I_{\text{VV}} \text{ or } I_{\parallel} \quad (4)$$

1.2. Molecular Reference System

The direct system of axes X, Y, Z (Figure 2) represents the laboratory system, but it is first necessary to work in the reference axes (x, y, z) of the molecular system. The transformation from one coordinate system to another one is carried out with the help of the three Euler angles, (θ, φ, ψ) defined in Figure 2, using the general relation

$$[\alpha_{xyz}] = [\mathbf{T}^t \alpha_{xyz} \mathbf{T}] \quad (5)$$

where

$$\mathbf{T} = \begin{pmatrix} \cos \theta \cos \varphi \cos \psi - \sin \theta \cos \psi & -\cos \theta \cos \varphi \sin \psi - \sin \theta \sin \psi & \sin \theta \cos \psi \\ \sin \varphi \sin \psi & \sin \varphi \cos \psi & 0 \\ \cos \theta \sin \varphi \cos \psi + \sin \theta \sin \psi & -\cos \theta \sin \varphi \sin \psi + \sin \theta \cos \psi & \sin \theta \sin \psi \\ \cos \varphi \sin \psi & \cos \varphi \cos \psi & 0 \\ -\sin \theta \cos \psi & \sin \theta \sin \psi & \cos \theta \end{pmatrix} \quad (6)$$

and \mathbf{T}^t denotes the transposed matrix. Therefore, for any isotropic or anisotropic medium we must consider averaged orientational quantities in the following general scattering intensity expression:

$$I_{\text{Raman}(I,J)} \approx \langle (\alpha_{IJ})^2 \rangle = \frac{1}{8\pi^2} \int_0^{2\pi} d\psi \int_0^{2\pi} d\varphi \int_{-1}^{+1} d(\cos \theta) F(\psi, \varphi, \cos \theta) [\mathbf{T}^t \alpha \mathbf{T}]^2 \quad (7)$$

Under these conditions, the orientation distribution function normalized (to 1.0) with respect to the total number of scattering centers is defined according to

$$\int \int \int F(\Omega) d\Omega = \frac{1}{8\pi^2} \int_0^{2\pi} d\psi \int_0^{2\pi} d\varphi \int_{-1}^{+1} d(\cos \theta) F(\psi, \varphi, \cos \theta) = 1.0 \quad (8)$$

and we directly retrieve the expressions for the usual cases of uniaxial symmetry:

(i) for a general uniaxial system (whatever φ)

$$F(\psi, 0, \theta) = F(\psi, \theta) \quad \text{and} \quad \frac{1}{4\pi} \int_0^{2\pi} d\psi \int_{-1}^{+1} F(\psi, \cos \theta) d(\cos \theta) = 1.0 \quad (9)$$

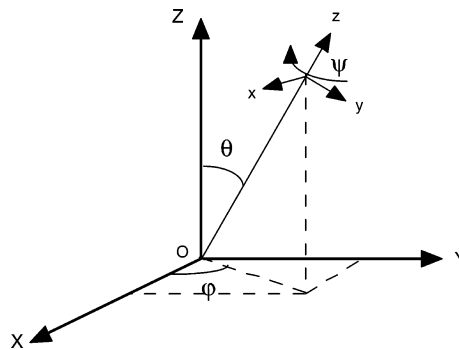


Figure 2. Definition of the three Euler angles.

(ii) for a uniaxial system containing rodlike molecules of cylindrical symmetry (whatever ψ)

$F(0,0,\theta) = F(\theta)$ so that

$$\frac{1}{2} \int_{-1}^{+1} F(\cos \theta) d(\cos \theta) = 1.0 \quad (10)$$

(iii) finally, for a totally isotropic system

(whatever θ)

$$F(0,0,0) = 1.0 \quad \text{and} \quad \frac{1}{2} \int_{-1}^{+1} F(0) d(\cos \theta) \equiv 1.0 \quad (11)$$

1.3. Application to a Simple Case Example

First, we consider the analytical intensity expressions $I_{\perp} = I_{(ZX)}$ and $I_{\parallel} = I_{(ZZ)}$ for the totally symmetric vibrations of a population of cigarlike (cylindric) molecules distributed in a system of uniaxial symmetry; their molecular polarizability tensor is

$$(\alpha_{xyz}) = \begin{pmatrix} \alpha_1 & 0 & 0 \\ 0 & \alpha_1 & 0 \\ 0 & 0 & \alpha_3 \end{pmatrix}$$

According to eq 7, we calculate the orientational averages $\langle (\alpha_{ZX})^2 \rangle$ and $\langle (\alpha_{ZZ})^2 \rangle$ and obtain

$$(\alpha_{ZX}) = \cos \varphi \sin \theta \cos \theta (\alpha_1 - \alpha_3) \quad \text{and} \quad \langle (\alpha_{ZX})^2 \rangle = \frac{2}{15} (\alpha_1 - \alpha_3)^2$$

leading after integration to

$$I_{(ZX)} \approx \frac{1}{15} (\alpha_1^2 + \alpha_3^2 - 2\alpha_1\alpha_3), \quad (\alpha_{ZZ}) = (\alpha_1 \sin^2 \theta + \alpha_3 \cos^2 \theta), \quad \text{and} \quad (12)$$

$$\langle (\alpha_{ZZ})^2 \rangle = \frac{2}{15} (8\alpha_1^2 + 3\alpha_3^2 + 4\alpha_1\alpha_3)^2$$

leading similarly to

$$I_{(ZZ)} \approx \frac{2}{15} (8\alpha_1^2 + 3\alpha_3^2 + 4\alpha_1\alpha_3) \quad (13)$$

From these expressions the theoretical ratio or “depolarization ratio” of the scattered intensities is

$$\rho_{\text{lin}} = I_{(ZX)}/I_{(ZZ)} = I_{(\text{VH})}/I_{(\text{VV})} = (\alpha_1^2 + \alpha_3^2 - 2\alpha_1\alpha_3) / (8\alpha_1^2 + 3\alpha_3^2 + 4\alpha_1\alpha_3)$$

or equivalently

$$\rho_{\text{lin}} = (r^2 - 2r + 1)/(8r^2 + 4r + 3) \quad \text{where} \\ r = (\alpha_1/\alpha_3) \quad (14)$$

Finally, it is easily checked that this depolarization ratio may take the remarkable values equal either to $1/8$ (when $\alpha_1 \gg \alpha_3$, i.e., when $r \gg 1.0$) or to $1/3$ (when $\alpha_1 \ll \alpha_3$, i.e., when $r \ll 1.0$); these values are sometimes encountered in resonance Raman studies, since they are characteristic of electric dipolar allowed electronic transitions polarized in a plane (2D dimension) or along a single direction (1D dimension), respectively.

2. Gas and Liquid Samples: Invariants of the Second-Order Raman Tensor

2.1. Depolarization Ratio in "Linear" Experiments (ρ_{lin})

Using a classical 90° geometry Raman setup (Figure 1), it is important to get an estimate of the depolarization ratio, $\rho_{\text{lin}} = I_{\text{VH}}/I_{\text{VV}}$ or I_{\parallel}/I_{\perp} , in an isotropic medium under "ordinary" spontaneous Raman conditions (outside resonance) in order to determine the symmetry of the modes responsible for the Raman activity. Generally, one may discriminate between two situations: $\rho_{\text{lin}} < 3/4$ (or equal to 0.0 in cubic symmetry) for the totally symmetric vibrations; $\rho_{\text{lin}} = 3/4$ for the nontotally symmetric modes.

In contrast, under resonance Raman conditions it is noteworthy that ρ_{lin} may take a different value. So, its variations with respect to the excitation laser energy will provide additional information, since the symmetry properties of the resonant electronic state(s) along with the symmetry of the vibronically coupled different electronic states play a great role in the selection rules.

2.2. Three Invariants of the Raman Tensor

One must first recall the general "symmetry rule": the relevant quantities concerning a rotational average for randomly oriented species (in a solution or a gas phase) must obviously be invariant with respect to the rotation symmetry; they belong to the irreducible representations of the rotation spatial group (without inversion), the R_3 group, similar to the "angular momentum" atomic functions.

According to Fano and Racah,⁵ any polarizability tensor $\alpha_{\rho\sigma}$ (where $\rho, \sigma = x, y, \text{ or } z$) is defined by three irreducible tensors $\alpha(\mathbf{0})$, $\alpha(\mathbf{1})$, and $\alpha(\mathbf{2})$ corresponding in rotational behavior to the spherical harmonics $Y(l)_m$, with $l = 0, 1, \text{ or } 2$, respectively, and m taking $(2l + 1)$ values, since $-l \leq m \leq +l$. Therefore, the various components of these tensors are

that belonging to the totally symmetric representation

$$\alpha(\mathbf{0})_0 = -\frac{1}{\sqrt{3}}(\alpha_{xx} + \alpha_{yy} + \alpha_{zz}) \quad (15)$$

those belonging to the same representations as the components of the dipolar magnetic momentum operator and transform according to the rotations R_x , R_y , and R_z respectively

$$\alpha(\mathbf{1})_{+1} = -\frac{1}{2}(\alpha_{xz} - \alpha_{zx} + i\alpha_{yz} - i\alpha_{zy}) \\ \alpha(\mathbf{1})_0 = \frac{i}{\sqrt{2}}(\alpha_{xy} - \alpha_{yx}) \\ \alpha(\mathbf{1})_{-1} = -\frac{1}{2}(\alpha_{xz} - \alpha_{zx} - i\alpha_{yz} + i\alpha_{zy}) \quad (16)$$

and those that transform as the components of the quadripolar momentum operator, that is, as the five "d" atomic orbitals

$$\alpha(\mathbf{2})_{+2} = \frac{1}{2}(\alpha_{xx} - \alpha_{yy} + i\alpha_{xy} + i\alpha_{yx}) \\ \alpha(\mathbf{2})_{+1} = \frac{1}{2}(\alpha_{xz} - \alpha_{zx} + i\alpha_{yz} + i\alpha_{zy}) \\ \alpha(\mathbf{2})_0 = \frac{1}{\sqrt{6}}(2\alpha_{zz} - \alpha_{xx} - \alpha_{yy}) \\ \alpha(\mathbf{2})_{-1} = \frac{1}{2}(\alpha_{xz} + \alpha_{zx} - i\alpha_{yz} - i\alpha_{zy}) \\ \alpha(\mathbf{2})_{-2} = \frac{1}{2}(\alpha_{xx} - \alpha_{yy} - i\alpha_{xy} - i\alpha_{yx}) \quad (17)$$

From the above quantities, the three tensor invariants are straightforwardly defined:¹⁻⁴

(i) The isotropy

$$\mathbf{G}^0 \text{ (or } \Sigma^0) = |\alpha(\mathbf{0})_0|^2 = 3\bar{\alpha}^2 \quad (18)$$

where $\bar{\alpha}^2 = 1/9(\alpha_{xx} + \alpha_{yy} + \alpha_{zz})^2$ is the mean polarizability.

(ii) The symmetric anisotropy

$$\mathbf{G}^s \text{ (or } \Sigma^2) = \sum |\alpha(\mathbf{2})_m|^2 = 2/3\gamma_s^2 \quad (19)$$

where $\gamma_s^2 = 1/2((\alpha_{xx} - \alpha_{yy})^2 + (\alpha_{yy} - \alpha_{zz})^2 + (\alpha_{zz} - \alpha_{xx})^2) + 3/4((\alpha_{xy} + \alpha_{yx})^2 + (\alpha_{yz} + \alpha_{zy})^2 + (\alpha_{zx} + \alpha_{xz})^2)$

(iii) The antisymmetric anisotropy

$$\mathbf{G}^a \text{ (or } \Sigma^1) = \sum |\alpha(\mathbf{1})_m|^2 = 2/3\gamma_a^2 \quad (20)$$

with $\gamma_a^2 = 3/4((\alpha_{xy} - \alpha_{yx})^2 + (\alpha_{yz} - \alpha_{zy})^2 + (\alpha_{zx} - \alpha_{xz})^2)$.

To facilitate the calculation of the invariants in terms of the tensor elements $\alpha_{\rho\sigma}$, it is also very convenient to define the two new "sum" and "difference" tensors

$$\mathbf{S}_{\rho\sigma} = 1/2(\alpha_{\rho\sigma} + \alpha_{\sigma\rho}) \quad \text{and} \quad \mathbf{A}_{\rho\sigma} = 1/2(\alpha_{\rho\sigma} - \alpha_{\sigma\rho}), \\ \text{respectively} \quad (21)$$

We then arrive at the following simple expressions for the three invariants:

$$\mathbf{G}^0 \text{ (or } \Sigma^0) = 3\bar{\alpha}^2 = 1/3|\text{Tr}(\mathbf{S})|^2 \\ \mathbf{G}^s \text{ (or } \Sigma^2) = 2/3\gamma_s^2 = \text{Tr}(\mathbf{S})(\mathbf{S}^t) - \mathbf{G}^0$$

$$\mathbf{G}^{\mathbf{a}} \text{ (or } \Sigma^1) = {}^2/{}_3\gamma \mathbf{a}^2 = \text{Tr}(\mathbf{A})(\mathbf{A}^{\mathbf{t}}) \quad (22)$$

where the symbol “Tr” indicates the trace of the tensor and the exponent “t” the transpose of the tensor (or its Hermitian conjugate if α is complex).

2.3. “Average” Raman Intensities and Depolarization Ratios

According to eqs 1–7, the Raman intensity is proportional to the squares of the tensor elements, but the elements must be averaged over all the molecular orientations. In this respect, instead of performing cumbersome calculations using the Euler angles, these quantities are more directly calculated with the help of the Clebsch–Gordan coefficients ($C_{L,J}^k$), as indicated hereafter:

$$\langle \alpha_{L,J}^2 \rangle = \sum_{k=0,a,s} C_{L,J}^k \mathbf{G}^k \quad (23)$$

conditions on L, J	$k = 0$	$k = s$	$k = a$
$I = J$	1/3	2/15	0
$I \neq J$	0	1/10	1/6

Under these conditions, the polarized scattering components are

$$I_{\perp(ZX)} \approx K \langle \alpha_{ZX}^2 \rangle = K({}^1/_{10} \mathbf{G}^s + {}^1/_{6} \mathbf{G}^a) = (K/30)(3\mathbf{G}^s + 5\mathbf{G}^a)$$

$$I_{\parallel(ZZ)} \approx K \langle \alpha_{ZZ}^2 \rangle = K({}^1/_{3} \mathbf{G}^0 + {}^2/_{15} \mathbf{G}^s) = (K/30)(10\mathbf{G}^0 + 4\mathbf{G}^s)$$

so that

$$I_{\text{total}} = (I_{\perp} + I_{\parallel}) = (K/30)(10\mathbf{G}^0 + 7\mathbf{G}^s + 5\mathbf{G}^a) \quad (24)$$

The general expression of the depolarization ratio ρ_{lin} for the 90° geometry setup is

$$\rho_{\text{lin}} = \frac{I_{\perp}}{I_{\parallel}} = \frac{3\mathbf{G}^s + 5\mathbf{G}^a}{10\mathbf{G}^0 + 4\mathbf{G}^s} = \frac{2\gamma_s^2 + {}^{10}/_3\gamma_a^2}{30\bar{\alpha}^2 + {}^8/_{3}\gamma_s^2} = \frac{3\gamma_s^2 + 5\gamma_a^2}{45\bar{\alpha}^2 + 4\gamma_s^2} \quad (25)$$

and three distinct important classes of Raman scattering processes can be distinguished:

Pure isotropic

$$\mathbf{G}^0 \neq 0; \mathbf{G}^s = \mathbf{G}^a = 0 \\ \rho_{\text{lin}} = 0 \text{ (whatever is the value of } \mathbf{G}^0)$$

Pure symmetric

$$\mathbf{G}^s \neq 0; \mathbf{G}^0 = \mathbf{G}^a = 0 \\ \rho_{\text{lin}} = {}^3/_{4} \text{ (depolarized modes, whatever is } \mathbf{G}^s)$$

Pure antisymmetric

$$\mathbf{G}^a \neq 0; \mathbf{G}^0 = \mathbf{G}^s = 0 \\ \rho_{\text{lin}} = \infty \text{ (“inverse” polarized modes, whatever is } \mathbf{G}^a)$$

From an experimental point of view, the above formulas deserve several comments:

(i) In the two above former classes of scattering, “ordinary” or spontaneous Raman processes are taking place, whereas the third case applies to particular resonance Raman conditions.

(ii) Under “ordinary” Raman conditions the tensor is always symmetric ($\alpha_{L,J} \equiv \alpha_{J,L}$), so that the third invariant \mathbf{G}^a is equal to zero and neglected. Therefore, any measurement of I_{\perp} provides direct information on the relative value of the “symmetric anisotropy”. So, the two following definitions and equations are often used in Raman polarization studies:

$$I_{\text{aniso}} = I_{\perp} \quad (26)$$

and

$$I_{\text{iso}} = I_{\parallel} - {}^4/_{3}I_{\text{aniso}} \quad (27)$$

Experimentally, it is obvious that the “isotropic” and “anisotropic” Raman responses exhibit, in general, quite different profiles (in intensity, maximum, half-width). In particular, the half-width at half-maximum of the isotropic Raman component, Γ_{iso} (cm^{-1}) = $(2\pi c\tau)^{-1}$, where τ is the lifetime of the intermediate state, is only a fraction of the broader anisotropic component, Γ_{aniso} . Actually, this latter profile is governed by several molecular dynamical processes (rotations, orientations, ...), and new information can be extracted using the Fourier transform formalism of the time dependent correlation functions.

(iii) From simple geometric arguments we may also conclude that the antisymmetric tensor invariant \mathbf{G}^a , which is effective under resonance Raman conditions, cannot be determined by using a linearly polarized laser beam; nor can new information be obtained by varying the scattering angle. So, other experiments must be performed using a circularly polarized incident beam, for instance.^{6,7}

In conclusion, we have shown that an accurate measurement of the depolarization ratio (ρ_{lin}) requires cautious experiments in most situations, and it is often worthwhile to carry out several checks using various standard solutions (using the high symmetry CCl_4 molecular liquid, for instance).

3. Crystalline and Amorphous Thin Films: Polarization Measurements in “Macro-Raman” Experiments

In contrast to the cases of the gas and liquid disordered states, in which the molecules are randomly distributed in space, another particular situation is that of an ordered single crystal where the molecular orientations are fixed and totally defined with respect to the crystallographic axes. In this latter case many polarized Raman experiments can be performed, by using generally accurate adjust-

ments of the incident and scattered electric field directions with respect to the principal axes of the refractive index ellipsoid (of wave normals). In these spectroscopic studies of molecular crystals, such measurements are well-known to afford a wealth of relevant information.⁴

Hereafter, we shall focus our attention on another kind of solid, the partially crystallized and/or amorphous polymer systems, in which some degree of orientation and ordering is effective. Indeed, various polymer samples which can be processed as thin films are able to transform into strongly anisotropic and partly oriented systems under mechanical (stretching) or photonic (irradiation) constraints: these samples are then characterized by a distribution function of the molecular orientations with respect to one (or two) selected direction(s). So, in the following we shall first recall the main expressions and symmetry properties of the orientation distribution functions in uniaxial and biaxial systems. Then, various results of vibrational studies performed on application examples of such polymer systems will be presented, and finally, some theoretical considerations related to the parameter order values and molecular deformation schemes proposed in the polymers will be discussed.

3.1. Series Expansion of the Orientation Distribution Functions in Uniaxial and Biaxial Systems

The development in spherical harmonics of any distribution functions, in particular those depending on the three angular variables (θ , φ , ψ), has first been studied by Roe et Krigbaum^{8,9} and by Bower et al.,¹⁰⁻¹³ who have proposed the following polynomial series:

$$F(\xi = \cos \theta, \varphi, \psi) = \sum_{l=0}^{\infty} \sum_{m=-l}^{+l} \sum_{n=-l}^{+l} \nu_{lmn} Z_{lmn}(\xi) \times \exp(-i(m\varphi + n\psi)) \quad (28)$$

where the term $Z_{lmn}(\xi)$ denotes the real generalized Legendre polynomials, which, according to Rodrigues formula, are

$$Z_{lmn}(\xi) = \frac{1}{2^l l!} \frac{d^l}{d\xi^l} (\xi^2 - 1)^l \quad (29)$$

with $Z_{000}(\xi) = 1.0$ and $Z_{lmn}(\xi) = (-1)^l Z_{lmn}(-\xi)$, and the coefficients ν_{lmn} are the ordinary quantities of the spherical harmonics averaged over the considered distribution:

$$\nu_{lmn} = \frac{1}{4\pi^2} \int_0^{2\pi} \int_0^{2\pi} \int_{-1}^{+1} F(\xi, \varphi, \psi) Z_{lmn}(\xi) \times \exp(+i(m\varphi + n\psi)) d\xi d\varphi d\psi \quad (30)$$

Equation 30 can be applied to normalized as well as to non-normalized Legendre functions, but the non-normalized forms are more often reported in the literature (see Table 1 in ref 14).¹⁴ Nevertheless, in

this case the ν_{lmn} coefficients are slightly different (see numerical factors) and are defined by the following $\langle P_{lmn} \rangle$ expression:

$$\langle P_{lmn} \rangle = \frac{4\pi^2}{N_{lmn}} \nu_{lmn}$$

where

$$N_{lmn}^2 = \frac{(2l+1)(l+m)!(l-n)!}{2(l-m)!(l+n)!} \frac{1}{[(m-n)!]^2} \quad (31)$$

Here, for simplicity, we shall consider only two variables, the polar (θ) and azimuthal (φ) Euler angles. According to Nomura et al.,¹⁵ the orientation distribution function is then developed in a series of normalized and general spherical harmonics, as indicated below:

$$F(\xi = \cos \theta, \varphi) = \sum_{l=0}^{\infty} \sum_{m=-l}^{+l} Q_{lm} \prod_l^m(\xi) \exp(-im\varphi) \quad (32)$$

where

$$Q_{lm} = \frac{1}{2\pi} \int_0^{2\pi} \int_{-1}^{+1} F(\xi, \varphi) \prod_l^m(\xi) \exp(-im\varphi) d(\xi) d(\varphi) \\ = \frac{1}{2\pi} \left[\left(\frac{2l+1}{2} \right) \frac{(l-m)!}{(l+m)!} \right]^{1/2} \langle F_{l,m} \rangle \quad (33)$$

and

$$\prod_l^m(\xi) = \frac{1}{2\pi} \left[\left(\frac{2l+1}{2} \right) \frac{(l-m)!}{(l+m)!} \right]^{1/2} P_l^m(\cos \theta) \quad (34)$$

Under these conditions, the $\langle F_{l,m} \rangle$ parameters are generalized orientational factors and the $P_l^m(\cos \theta)$ functions are the associated nonnormalized Legendre polynomials of great interest:

(i) when $l \neq m$

$$P_l^m(\cos \theta) = (1 - \cos^2 \theta)^{m/2} \frac{d^m}{d(\cos \theta)} P_l(\cos \theta) \quad (35)$$

(ii) when $l \equiv m (= 0, 1, 2, \dots)$

$$P_l^m(\cos \theta) = 1.3 \dots (2m-1) \sin^m \theta \quad (36)$$

We thus arrive at the general expressions of the orientation distribution functions:

In a biaxial model system we obtain

$$F(\cos \theta, \varphi) = \frac{1}{4\pi^2} \sum_{l=0,2,4} \sum_{m=-l}^{+l} \left\{ \left(\frac{2l+1}{2} \right) \frac{(l-|m|)!}{(l+|m|)!} \right. \\ \left. \langle F_{l,|m|} \rangle P_l^{|m|}(\cos \theta) \exp(-im\varphi) \right\} \quad (37)$$

In a uniaxial system, assuming $m = 0$, the expression becomes obviously simpler

$$F(\cos \theta) = \frac{1}{4\pi^2} \sum_{l=0,2,4} \left\{ \left(\frac{2l+1}{2} \right) \langle F_{l,0} \rangle P_l(\cos \theta) \right\} \quad (38)$$

Actually, we shall develop the even-parity distribution function up to only the fourth moment, since in the Raman scattering technique we can reach the factors $\langle F_{l,m} \rangle$ up to only $l = 2$ and 4 ; so, the complete analytical expression of the distribution is

$$\begin{aligned} F(\cos \theta, \varphi) = & \frac{1}{4\pi^2} \left\{ \frac{1}{2} + \frac{5}{4} (3 \cos^2 \theta - 1) \langle F_{2,0} \rangle + \right. \\ & \frac{9}{16} (35 \cos^4 \theta - 30 \cos^2 \theta + 3) \langle F_{4,0} \rangle + \\ & \frac{5}{8} (\sin^2 \theta \cos 2\varphi) \langle F_{2,2} \rangle - \\ & \frac{3}{16} (7 \cos^4 \theta - 8 \cos^2 \theta + 1) (\cos 2\varphi) \langle F_{4,2} \rangle + \\ & \left. \frac{3}{128} (\cos^4 \theta - 2 \cos^2 \theta + 1) (\cos 4\varphi) \langle F_{4,4} \rangle \right\} \quad (39) \end{aligned}$$

where, in agreement with Nomura et al.,¹⁵ the five generalized orientation factors $\langle F_{l,m} \rangle$ display the simple expressions reported in the following equations (eqs 40–44):

$$\langle F_{2,0} \rangle = \frac{1}{2} (3 \langle \cos^2 \theta \rangle - 1) = \langle P_2(\cos \theta) \rangle \equiv f_\theta \quad (\text{see ref 16}) \quad (40)$$

$$\langle F_{4,0} \rangle = \frac{1}{8} (35 \langle \cos^4 \theta \rangle - 30 \langle \cos^2 \theta \rangle + 3) \equiv \langle P_4(\cos \theta) \rangle \quad (41)$$

$$\langle F_{2,2} \rangle = \langle 3 \sin^2 \theta \cos 2\varphi \rangle = 12 \langle P_{2,2}(\cos \theta) \rangle \equiv 2f_\varphi (1 - f_\theta) \quad (\text{see ref 16}) \quad (42)$$

$$\langle F_{4,2} \rangle = \frac{15}{2} (-7 \langle \cos^4 \theta \rangle + 8 \langle \cos^2 \theta \rangle - 1) \langle \cos 2\varphi \rangle = 180 \langle P_{4,2}(\cos \theta) \rangle \quad (43)$$

$$\langle F_{4,4} \rangle = (105 \langle \sin^4 \theta \rangle) \langle \cos 4\varphi \rangle = 1680 \langle P_{4,4}(\cos \theta) \rangle \quad (44)$$

Note that the two former factors are effective in any uniaxial distribution along the OZ long axis (“fiber symmetry”) with a random rotation about the director and with possible averages over both the φ and ψ angles (Figure 2). In contrast, the three latter factors characterize a biaxial symmetry with a possible average over only the ψ angle. In the distinct situation of biaxial symmetry with an average over the angle φ , it will be necessary to change the factors $\langle F_{2,2,0} \rangle$, $\langle F_{4,2,0} \rangle$, and $\langle F_{4,4,0} \rangle$ to $\langle F_{2,0,2} \rangle$, $\langle F_{4,0,2} \rangle$, and $\langle F_{4,0,4} \rangle$, respectively. Of course, it will be necessary to substitute the angle φ for ψ in the related equivalent expressions.

Finally, we must underline that in the more general case of biaxial symmetry without any possible average over both the φ and ψ angles, the complete distribution function $F(\cos \theta, \varphi, \psi)$ will con-

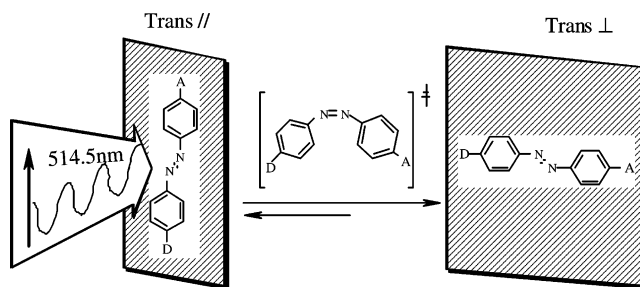


Figure 3. Scheme of a photoisomerization cycle under linearly polarized irradiation.

tain four additional factors, namely $\langle F_{2,2,2} \rangle$, $\langle F_{4,2,2} \rangle$, $\langle F_{4,2,4} \rangle$, and $\langle F_{4,4,2} \rangle$; this leads to a total of 13 factors in the complete distribution function.¹⁴ Under these conditions, it will be quite difficult to get an estimate of all the orientational coefficients from only polarized Raman experiments, even if the individual elements of the molecular polarizability tensor are already well-known from previous studies.

3.2. Application Examples in Systems of Uniaxial Symmetry

3.2.1. Photoinduced Orientation in a DR1 Dye Doped Polymer Film^{17–20}

It is well-known that “push–pull” type chromophores such as the *trans*-azobenzene dyes, which are substituted in the 4–4′ positions with electron donating (–NR₂) and electron accepting (–NO₂) groups, possess intense electronic transitions in the visible region. Under irradiation with a linearly polarized light, the “dispersed red 1” (DR1) type molecule undergoes numerous photoisomerization and reorientation cycles, $\text{trans}_{(//)} \leftrightarrow [\text{cis}]^{\#} \leftrightarrow \text{trans}_{(\perp)}$ (Figure 3). This process leads to a birefringent uniaxial material with preferential orientations of the chromophores perpendicular to the polarization direction of the incident beam.

Macro-Raman scattering experiments using the 90° geometry were performed initially on isotropic films and, later, on the same films after a beam irradiation ($I_0 \approx 10\text{--}15 \text{ mW/cm}^2$, relatively weak to avoid any photobleaching) in order to determine the two orientation factors $\langle F_{2,0,0} \rangle$ and $\langle F_{4,0,0} \rangle$; hereafter, for simplicity, we shall preferentially make use of the short notations $\langle P_2 \rangle$ and $\langle P_4 \rangle$ for the corresponding Legendre parameters. However, an experimental complication arose for obtaining confident reference data; the difficulty was to investigate the initial sample without any perturbation of its isotropy: such a problem has been solved by using a circularly polarized pump beam. Indeed, for the rod-shaped DR1 molecules of cylindrical symmetry, we may assume the diagonal tensor

$$\bar{\alpha} = \begin{pmatrix} \alpha_1 & & \\ & \alpha_1 & \\ & & \alpha_3 \end{pmatrix} \quad (45)$$

and by using first a circularly polarized (denoted by the symbol \odot) and after a linearly polarized (symbol \uparrow) “pump” incident laser, we have checked that the

following intensity relations were satisfied (see Figure 1 for the reference system axes):

(i) First,

$$I_{\text{total}}^{\uparrow} = I_{\parallel}^{\uparrow} + I_{\perp}^{\uparrow} = I_{\text{total}}^{\uparrow} = I_{ZZ}^{\uparrow} + I_{ZX}^{\uparrow}$$

$$I_{\text{total}}^{\uparrow} \approx \frac{\alpha_3^2 N_0 I_0}{15} (9r^2 + 2r + 4) \quad (46)$$

where $r = \alpha_1/\alpha_3$

(ii) Second,

$$\frac{I_{ZZ}^{\uparrow}}{\alpha_3^2 N_0 I_0} \approx \frac{1}{15} \left\{ (8r^2 + 4r + 3) - \frac{20}{7} (4r^2 - r - 3) \langle P_2 \rangle + \frac{24}{7} (r^2 - 2r + 1) \langle P_4 \rangle \right\} \quad (47)$$

$$\frac{I_{ZX}^{\uparrow}}{\alpha_3^2 N_0 I_0} \approx \frac{1}{15} (r^2 - 2r + 1) \left\{ 1 + \frac{5}{7} \langle P_2 \rangle - \frac{12}{7} \langle P_4 \rangle \right\} \quad (48)$$

These expressions can be recasted under the simpler forms

$$\frac{I_{ZZ}^{\uparrow}}{\alpha_3^2 N_0 I_0} \approx A - 2B \langle P_2 \rangle + 8C \langle P_4 \rangle \quad \text{and}$$

$$\frac{I_{ZX}^{\uparrow}}{\alpha_3^2 N_0 I_0} \approx D - E \langle P_2 \rangle - 4C \langle P_4 \rangle \quad (49)$$

with the coefficients

$$A = \frac{1}{15} (8r^2 + 4r + 3) \quad B = \frac{1}{21} (8r^2 - 2r - 6)$$

$$C = \frac{1}{35} (r^2 - 2r + 1) \quad D = \frac{1}{15} (r^2 - 2r + 1)$$

$$E = \frac{-1}{21} (r^2 - 2r + 1) \quad (50)$$

To complete the experiments, we had also to determine the depolarization ratio of each vibrational mode (using a solution) in order to calculate the polarizability ratio $r = \alpha_1/\alpha_3$. As already discussed (subsection 1.3), the expression for the depolarization ratio is

$$\rho_{\text{lin}} = \frac{I_{\text{VH}}}{I_{\text{VV}}} = \frac{(1-r)^2}{(8r^2 + 4r + 3)} \quad (51)$$

So, finally, an estimate of the two order parameters was obtained from the measurement of the two ratios of polarized relative Raman intensities

$$\left\{ \begin{aligned} R_1 &= \frac{I_{ZX}^{\uparrow}}{I_{ZZ}^{\uparrow}} = \frac{D - E \langle P_2 \rangle - 4C \langle P_4 \rangle}{A - 2B \langle P_2 \rangle + 8C \langle P_4 \rangle} \\ R_2 &= \frac{I_{ZX}^{\uparrow} + I_{ZZ}^{\uparrow}}{I_{\text{total}}^{\uparrow}} = \frac{(A + D) - (2B + E) \langle P_2 \rangle + (4C) \langle P_4 \rangle}{(A + D)} \end{aligned} \right. \quad (52)$$

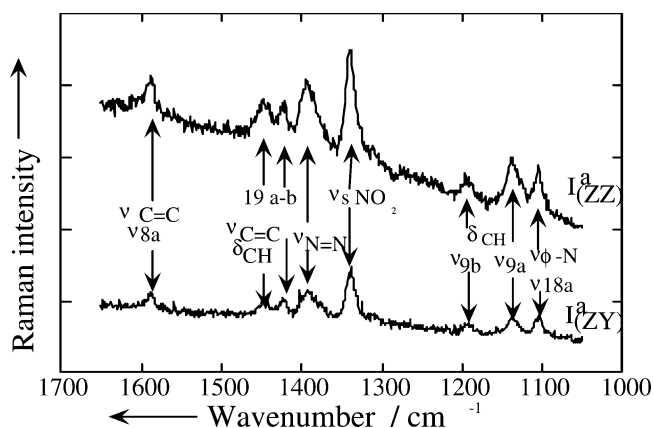


Figure 4. Polarized resonance Raman spectra, I_{ZZ} and I_{ZY} (or I_{ZX}) for a DR1-PMMA dye doped film (3% wt/wt; $N = 6.9 \times 10^{19}$ molecules/cm³) after a 15 mW/cm² irradiation at 496.5 nm. (Reproduced with permission from ref 17. Copyright 1996 John Wiley & Sons Limited.)

Table 1. Raman Results for Several Vibrational Modes in a DR1-PMMA Dye Doped Film (3% wt/wt) after a 15 mW/cm² Irradiation at 496.5 nm^a

mode	$\nu_s(\text{NO}_2)$	$\nu(\text{N}=\text{N})$	$\nu(19a)$	$\nu(19b)$, $\delta(\text{CH}_2)$	$\nu(8a)$
ν/cm^{-1}	1339	1392	1423	1449	1588
ρ_{lin}	0.358	0.353	0.365	0.410	0.410
$\langle P_2 \rangle$	-0.120	-0.086	-0.102	-0.028	-0.066
(IR data)	(-0.110)	(-0.095)			(-0.085)
$\langle P_4 \rangle$	+0.013	+0.014	+0.025	+0.007	+0.032

^a For a better comparison, some infrared data are given in parentheses.

Experimentally, we did observe significant intensity variations on the polarized Raman spectra of an irradiated film (Figure 4), leading to the results reported in Table 1 for several vibrational modes.

It is noteworthy that all values of the $\langle P_2 \rangle$ parameter are negative and confirm a preferential orientation perpendicular to the exciting polarization direction; however, these values are far from the -0.5 limit expected for a complete alignment. Furthermore, we note a very good agreement with some (partial) infrared results of dichroism measurements;²⁰ this provides another evidence for the validity of the proposed Raman approach. Finally, it is important to recall that from the $\langle P_2 \rangle$ order parameter value we may only suggest a mean orientation angle $\langle \cos^2 \theta \rangle$; meanwhile, the additional knowledge of the fourth rank parameter $\langle P_4 \rangle$ is necessary to determine precisely the shape of the orientational distribution function (see later). Indeed, within the optical pumping model of cylindrical molecules distributed inside a system of uniaxial symmetry, the resulting chromophore orientation function is only dependent on the polar θ angle (see Scheme 1). The orientation function may thus be developed under the classic series of even order Legendre polynomials:

$$F(\theta) = \sum_{l=0,2,4} \left(\frac{2l+1}{2} \right) \langle P_l \rangle P_l(\cos \theta) \quad (53)$$

However, the development is restricted and it is not mandatory that the series is converging. So, it is advisable to use the "information entropy" model in

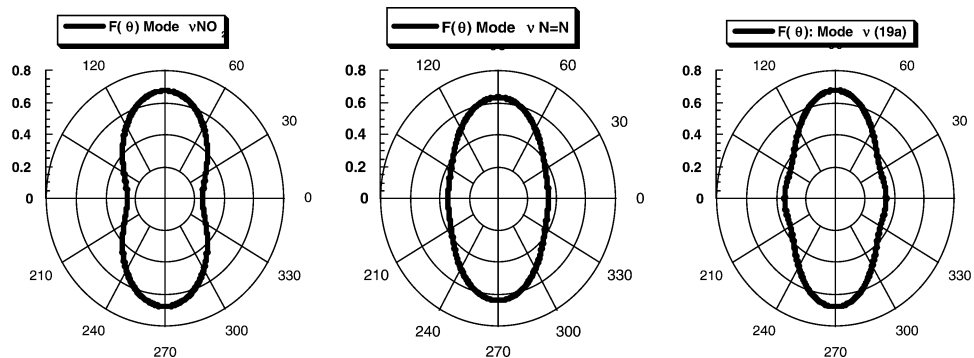
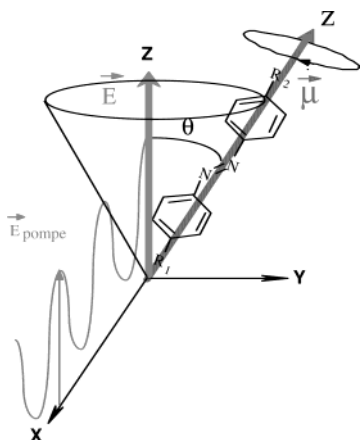


Figure 5. Most probable orientation distribution functions for three DR1 vibrational modes.

Scheme 1



order to maximize the entropy and to get estimates of the Lagrange multipliers (λ_2, λ_4): one thus obtains normalized orientational distribution functions, which are physically meaningful whatever the space region considered. The “most probable” orientation function is then defined as

$$F(\theta) = \frac{\exp(\lambda_2 P_2(\cos \theta) + \lambda_4 P_4(\cos \theta))}{\int_{-1}^{+1} d(\cos \theta) [\exp(\lambda_2 P_2(\cos \theta) + \lambda_4 P_4(\cos \theta))]} \quad (54)$$

The results so far obtained are reported in Figure 5 for three vibrational modes, $\nu(\text{NO}_2)$ ($\lambda_2 = -0.666$; $\lambda_4 = +0.021$), $\nu(\text{N}=\text{N})$ ($\lambda_2 = -0.452$; $\lambda_4 = +0.087$), and $\nu(\text{ring}19\text{a})$ ($\lambda_2 = -0.533$; $\lambda_4 = +0.180$), respectively. As expected, all the distributions exhibit a similar shape and display a maximum at $\pm 90^\circ$. However, some differences are observed at about 0° and 180° , since the $\langle P_4 \rangle$ parameter plays an important role in the width of the distributions.

3.2.2. Uniaxial Orientation in Stretched Polyethylene (PE) Films^{21,22}

During the past decades, several molecular orientation studies on low and high density PE samples were carried out because of not only urgent industrial inquiries for high mechanical modulus films or fibers but also a fundamental interest in establishing the assignments of the Raman active modes. Also, another goal of these studies was to get a better insight into

the orientational properties of the chains in this semicrystalline polymer (in which amorphous and crystalline phases are mixed). Here, we shall refer to a very nice Raman study of high density PE films (thickness ≈ 1.0 mm), which were stretched under the ratios (κ) from 7.0 to 11.7 (with no preferential orientation about the stretching axis).²¹ In such samples with a statistical uniaxial symmetry, we expect, in agreement with Bower's theoretical treatment,^{10,11} five independent expressions for the polarized Raman intensities; these expressions stem from sums and products of various polarizability tensor elements, $\sum \alpha_{ij}^2$ or $\sum \alpha_{ij} \alpha_{ji}$. Actually, for the totally symmetric vibrations displaying a diagonal tensor

$$\begin{pmatrix} \alpha_1 & & \\ & \alpha_2 & \\ & & \alpha_3 \end{pmatrix}$$

(for modes of A_g and B_{1g} symmetry species in orthorhombic PE), whose axes are coincident to those of the structural unit (see Figure 6), one can establish the following five relations:

$$\sum \alpha_{22}^2 = \frac{I[\alpha_{XX}^2]}{I_0 N_0 \alpha_3^2} \approx A + B \langle F_{2,0,0} \rangle + 3C \langle F_{4,0,0} \rangle$$

$$\sum \alpha_{33}^2 = \frac{I[\alpha_{ZZ}^2]}{I_0 N_0 \alpha_3^2} \approx A + 2B \langle F_{2,0,0} \rangle + 8C \langle F_{4,0,0} \rangle$$

$$\sum \alpha_{12}^2 = \frac{I[\alpha_{XY}^2]}{I_0 N_0 \alpha_3^2} \approx D + 2E \langle F_{2,0,0} \rangle + C \langle F_{4,0,0} \rangle$$

$$\sum \alpha_{32}^2 = \frac{I[\alpha_{ZX}^2]}{I_0 N_0 \alpha_3^2} \approx D - E \langle F_{2,0,0} \rangle - 4C \langle F_{4,0,0} \rangle$$

$$\sum \alpha_{22} \alpha_{33} = \frac{I[\alpha_{XX} \alpha_{ZZ}]}{I_0 N_0 \alpha_3^2} \approx (A - 2D) + (2E - B/2) \langle F_{2,0,0} \rangle - 4C \langle F_{4,0,0} \rangle \quad (55)$$

where $I_0 N_0 \alpha_3^2$, $\langle F_{2,0,0} \rangle$, $\langle F_{4,0,0} \rangle$, $r_1 = \alpha_1/\alpha_3$, and $r_2 = \alpha_2/\alpha_3$ are the five unknowns of the problem. Note

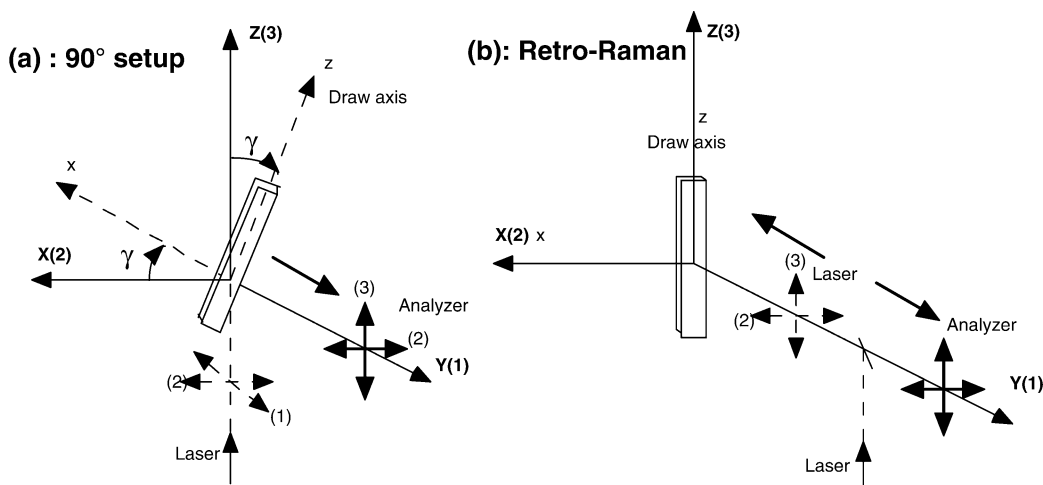


Figure 6. Experimental scattering setup (a) at 90° and (b) at 180° (or backscattering) for the polarized Raman studies of PE films stretched along the oz direction.

that the two polarizability ratios appear in the definitions of the coefficients A , B , C , D , and E :

$$\begin{aligned}
 A &= \frac{1}{15}(3r_1^2 + 3r_2^2 + 2r_1r_2 + 2r_1 + 2r_2 + 3) \\
 B &= \frac{1}{21}(3r_1^2 + 3r_2^2 + 2r_1r_2 - r_1 - r_2 - 6) \\
 C &= \frac{1}{280}(3r_1^2 + 3r_2^2 + 2r_1r_2 - 8r_1 - 8r_2 + 6) \\
 D &= \frac{1}{15}(r_1^2 + r_2^2 - r_1r_2 - r_1 - r_2 + 1) \\
 E &= \frac{1}{42}(r_1^2 + r_2^2 - 4r_1r_2 + 2r_1 + 2r_2 - 2) \quad (56)
 \end{aligned}$$

Experimentally, the authors have made use of both the 90° and 180° scattering geometries (Figure 6). In the former configuration they have intentionally rotated the sample about the OY axis and adjusted the sample to the special values $\gamma = 0^\circ$, 45° , or 90° , to solve more rapidly the system of five scattering intensity equations.

(i) In the first geometry (the 90° geometry), four polarized spectra were recorded for each angular value, γ :

$$\begin{aligned}
 \text{(VH)} \quad I_{12}(\gamma) &\approx \sum(\alpha_{12} \cos \gamma - \alpha_{13} \sin \gamma)^2 \\
 \text{(VV)} \quad I_{13}(\gamma) &\approx \sum(\alpha_{12} \sin \gamma - \alpha_{13} \cos \gamma)^2 \\
 \text{(HH)} \quad I_{22}(\gamma) &\approx \sum(\alpha_{22} \cos^2 \gamma - \alpha_{23} \sin 2\gamma + \alpha_{33} \sin^2 \gamma)^2 \\
 \text{(HV)} \quad I_{23}(\gamma) &\approx \sum\left(\frac{1}{2}\alpha_{22} \sin 2\gamma + \alpha_{23} \cos 2\gamma - \frac{1}{2}\alpha_{33} \sin 2\gamma\right)^2 \quad (57)
 \end{aligned}$$

It is noteworthy that in the above formulas we have reported the (VH), (VV), ... type notations (see Figure 1), which are still of a traditional use (even though

“old fashioned”) in many publications. More importantly, it must be pointed out that the $I_{23}(0^\circ)$ spectrum should be identical to the $I_{23}(90^\circ)$ spectrum, provided there is no depolarization of the diffusion; in contrast, birefringence effects, which are quite difficult to totally eliminate, could be detected for the angle $\gamma = 45^\circ$.

(ii) Conversely, in the “retro-Raman geometry” (at 180°), only three independent measurements were performed, namely

$$\begin{aligned}
 \text{“VV” or ZZ} \quad I_{33} &\approx \sum \alpha_{33}^2 \\
 \text{“VH” or ZX} \quad \text{(HV or XZ)} \quad I_{23} &\equiv I_{32} \approx \sum \alpha_{23}^2 \\
 \text{“HH” or XX} \quad I_{22} &\approx \sum \alpha_{22}^2 \quad (58)
 \end{aligned}$$

Under these conditions, the Raman spectra were analyzed essentially in the 1000–1500 cm^{-1} region, where are located the characteristic bands due to $\nu(\text{C}-\text{C})$ modes at 1080 and 1130 cm^{-1} , and those due to the rocking and deformation modes, ρ and $\delta(\text{CH}_2)$, at 1170 and 1480 cm^{-1} for the crystalline (trans chains) and amorphous (trans and gauche segments) parts, respectively. The crude and renormalized intensity Raman spectra for the 90° experiments are reported in Figure 7A and B, and the results concerning the tensor elements and the orientation coefficients are gathered in Table 2. We must point out that the orientation parameters in the amorphous parts were estimated within the framework of a simple two phase model and under the assumption of a 70% weight fraction for the crystalline part (estimate from density measurements).

From the above results it appears that not only does the Raman tensor of these modes not belong to the cylindrical symmetry ($r_1 \neq r_2$) but also the polarizability variations display opposite signs in the plane and perpendicular to the chain plane; this effect is more pronounced for the $\rho(\text{CH}_2)$ mode, as expected. Furthermore, it must be pointed out that, when using only the experimental results recorded under the 90° configuration (Figure 7A and B), the

Table 2. Ratios for the Principal Components of the Raman Tensors (r_1 , r_2) and Values of the Orientation Coefficients [$\langle P_2(\cos \theta) \rangle$, $\langle P_4(\cos \theta) \rangle$] for Several Vibrational Modes of a PE Film Stretched under the Conditions $\kappa = 7.0$ and 11.7, Respectively (Adapted from Ref 21)

wavenumber	mode	κ	$r_1 = \alpha_1/\alpha_3$	$r_2 = \alpha_2/\alpha_3$	$\langle P_2(\cos \theta) \rangle^a$	$\langle P_4(\cos \theta) \rangle^a$
1080 cm^{-1}	$\nu(\text{C}-\text{C})$ am.	7.0	-1.10	+0.79	+0.42	+0.40
		11.7	-1.05	+0.80	+0.47	+0.47
1130 cm^{-1}	$\nu_s(\text{C}-\text{C})$ crist (am.)	7.0	-0.54	+0.31	+0.75 (+0.95; +0.27)	+0.56 (+0.87; -0.15)
		11.7	-0.57	+0.42	+0.85 (+0.96; +0.60)	+0.69 (+0.90; +0.11)
1170 cm^{-1}	$\rho(\text{CH}_2)$ crist (am.)	7.0	-6.2	+0.42	+0.84	+0.45
		11.7	-7.3	+0.40	+0.87	+0.52

^a The sets of two numbers in parentheses were determined from diffraction studies and correspond to values of the order parameter in the crystalline (X-ray) and amorphous (am.) parts, respectively.

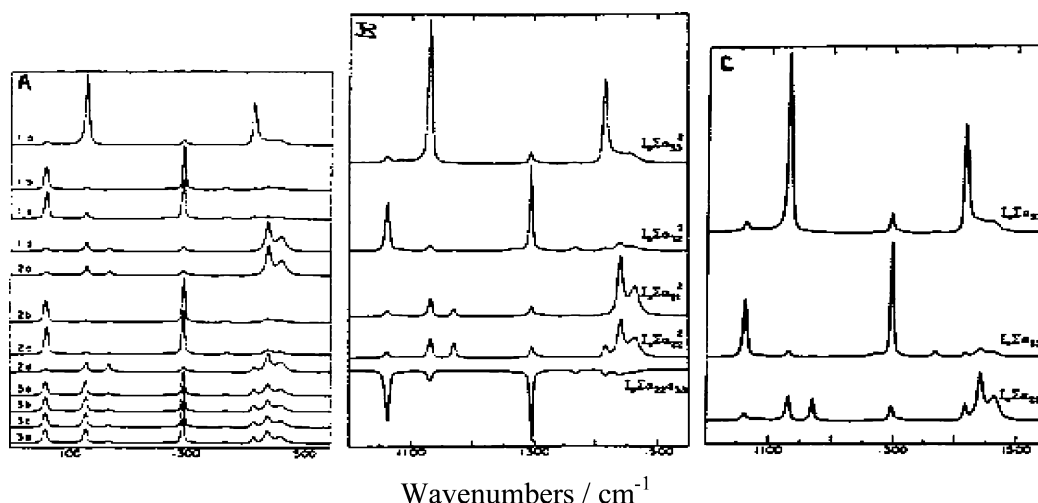


Figure 7. (A) Polarized Raman spectra recorded using the 90° geometry and the angle $\gamma = 90^\circ$ (1), 0° (2), or 45° (3) for a stretched PE film ($\kappa = 11.7$) for the tensor elements $[\alpha_{33}]^2$ (1a), $[\alpha_{32}]^2$ (1b, 1c, 2b, 2c), $[\alpha_{21}]^2$ (1d, 2a), $[\alpha_{22}]^2$ (2d), $[\alpha_{32}]^2$ (1b, 1c, 2b, 2c), and $[\alpha_{21}^2 + \alpha_{32}^2]/2$ (3c, 3d). (B) Result of the calculations to establish the five independent and normalized polarized Raman spectra. (C) Comparison of calculated (from 90° experiments) and recorded (180° geometry) Raman spectra. (Reprinted with permission from ref 21. Copyright 1991 American Chemical Society.)

solutions of the five intensity equations (eqs 55) lead to a very good agreement between theory and experiments for the other backscattering spectra (Figure 7C): this confirms the consistency of the present results. We can thus be quite confident in the parameter values of $\langle P_2(\cos \theta) \rangle$ and $\langle P_4(\cos \theta) \rangle$, even though the values appear always smaller than those determined from X-ray diffraction in the crystalline part. Therefore, under the assumptions of a simple two phase model and a crystalline content equal to $y_{\text{crist}} = 70\%$, one gets a better estimate of the orientation coefficients for the sequences of “trans-chain” segments in both the crystalline (ordered) and amorphous (disordered) phases, via the equation

$$\langle P_n(\cos \theta) \rangle_{\text{total}} = y_{\text{crist}} \langle P_n(\cos \theta) \rangle_{\text{crist}} + (1 - y_{\text{crist}}) \langle P_n(\cos \theta) \rangle_{\text{amorph}} \quad (59)$$

Consequently, it is evidenced that the amorphous part is reorientated more efficiently under stretching in these PE films; this result is reinforced by the significant increase (from +0.27 up to +0.60) observed on the $\langle P_2(\cos \theta) \rangle$ coefficient of the amorphous part for the mode at 1130 cm^{-1} (Table 2). Then, by application of the “information entropy” model to the stretching $\nu_s(\text{C}-\text{C})$ mode, we have calculated the shape of the most probable orientation distribution functions, as shown in Figure 8; in this figure the stretching direction is horizontal. So, the “trans”

sequences appear highly ordered in the crystalline parts, while their distribution function is significantly weaker and broader (with weak maxima at $\pm 23^\circ$) in the disordered amorphous regions.

Furthermore, the authors have observed in the $I_{33} \approx \sum \alpha_{33}^2$ backscattering spectra a very strong intensity enhancement of the mode at 1130 cm^{-1} as a function of the stretching; meanwhile, the intensity of the band at 1060 cm^{-1} was nearly constant (Figure 9a). Relevant correlations between the variations of the intensity ratio $[I(1130)/I(1060)]$ and the value of either the $\langle P_2(\cos \theta) \rangle$ or the $\langle P_4(\cos \theta) \rangle$ coefficient were thus established and found valuable for a wide range of stretching conditions (Figure 9b). It must be pointed out that such a method has also been applied with success to thicker samples and to other high density extruded films, so that it is of potential application as a reliable simple orientational “test”.

Finally, it is worthwhile to note that, in the course of other independent Raman polarized studies on stretched polyethylene films, Gordeyev et al.^{22a-22b} have similarly established very good correlations between the intensity variations of several modes and the amplitude of the stretching factor. Such spectroscopic investigations are thus known to afford new relevant information about the phase transition mechanisms between the layer type and fiber type structures in these uniaxially stretched PE polymer materials.

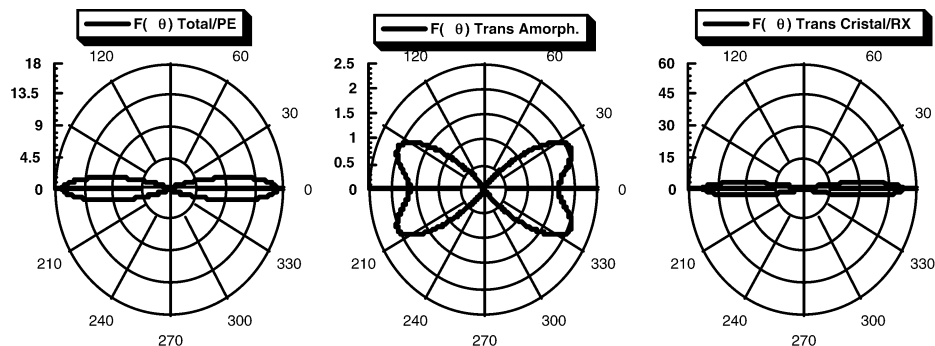


Figure 8. Most probable orientation distribution functions of “trans-sequences” in the whole PE sample and its amorphous and crystalline (X-ray) parts, under the stretching condition $\kappa = 11.7$.

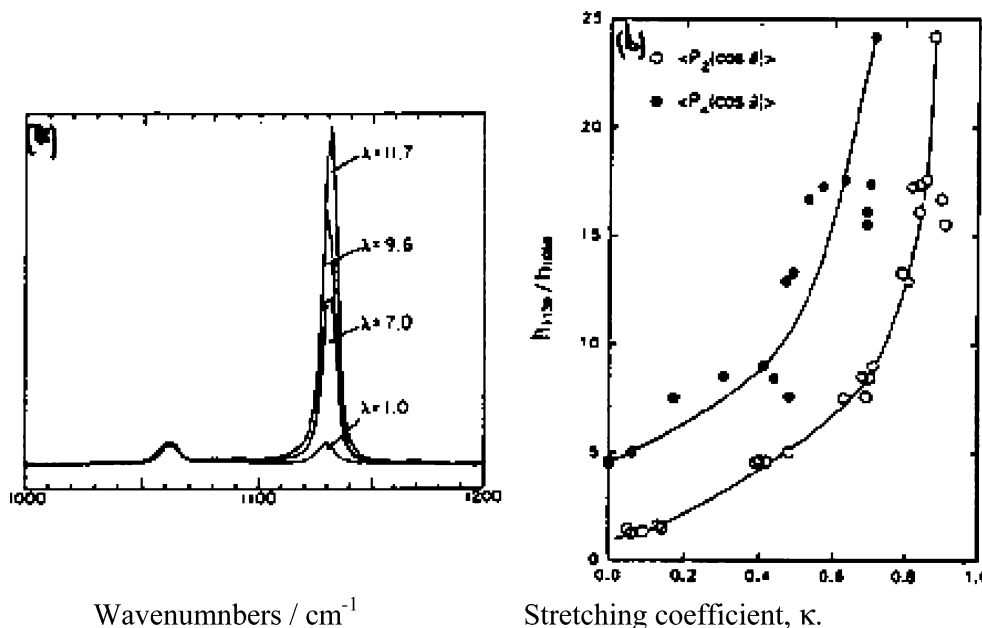


Figure 9. (a) Intensity variations of the Raman modes at 1130 and 1060 cm^{-1} in the $[\alpha_{33}]^2$ spectra as a function of the stretching coefficient (here note $\lambda \equiv \kappa = 1.0-11.7$). (b) Correlations between the intensity ratio $[I(1130)/I(1060)]$ and the orientation parameters, $\langle P_2 \rangle$, $\langle P_4 \rangle$, under various stretching conditions. (Reprinted with permission from ref 21. Copyright 1991 American Chemical Society.)

3.2.3. Correlation Diagrams of $\langle P_4 \rangle$ versus $\langle P_2 \rangle$ in Uniaxial Systems^{12,23-25}

According to the respective values of the $\langle P_2 \rangle$ and $\langle P_4 \rangle$ parameter orders, it may be of great interest in any uniaxial system to have a rapid knowledge of the distribution function we are dealing with: the aim is thus to get a better insight into the domains of existence of the different kinds of functions, but considering that values for both coefficients must be always physically meaningful. If a mean orientation angle cannot be preferentially selected and if only $\langle P_2 \rangle$ is known, a Gaussian orientational distribution centered either at 0° for $\langle P_2 \rangle$ positive (orientation parallel to the constraint) or at 90° for $\langle P_2 \rangle$ negative (orientation perpendicular to the constraint) is generally considered. In contrast, when both the $\langle P_2 \rangle$ and $\langle P_4 \rangle$ values are known, the shape of the distribution function is not necessarily unique, as the two parameter values are not totally independent.

Indeed, according to the Schwartz inequalities,

$$\langle \cos^2 \theta \rangle^2 \leq \langle \cos^4 \theta \rangle \leq \langle \cos^2 \theta \rangle \quad (60)$$

the domain of variations for $\langle P_4 \rangle$ is restricted and limited to the following range,

$$\langle P_4 \rangle_{\min} = \frac{1}{18}(5\langle P_2 \rangle^2 - 10\langle P_2 \rangle - 7) \leq \langle P_4 \rangle \leq \frac{1}{12}(5\langle P_2 \rangle + 7) = \langle P_4 \rangle_{\max} \quad (61)$$

Three main consequences are derived:

- (i) If $\langle P_4 \rangle = \langle P_4 \rangle_{\max}$, the distribution function must be bimodal and exhibit two δ maxima peaking at $\theta = 0^\circ$ and $\theta = 90^\circ$.
- (ii) If $\langle P_4 \rangle = \langle P_4 \rangle_{\min}$, the distribution function is necessarily unimodal with a peak maximum at

$$\theta_0 = \arccos\left(\frac{2}{3}\langle P_2 \rangle + \frac{1}{3}\right)^{1/2} \quad (62)$$

This assumption is often encountered in the literature when $\langle P_2 \rangle$ is the unique known value.

(iii) For all other $\langle P_4 \rangle$ values, the extrema of the distribution function can be obtained from the derivative of eq 54. Among the possible solutions, there

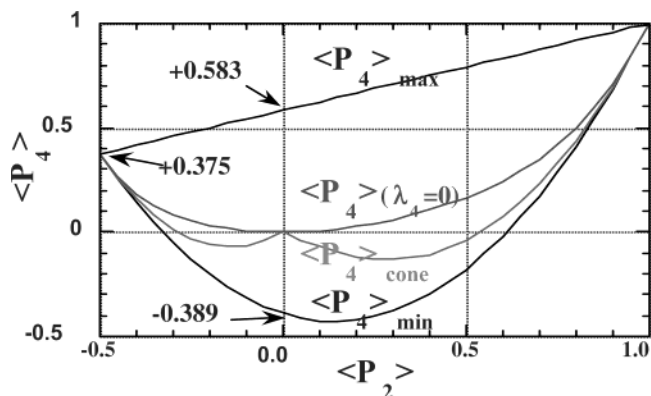


Figure 10. Various domains for the distribution functions as defined from the $\langle P_2 \rangle$ and $\langle P_4 \rangle$ order parameters according to the “information entropy” model ($\langle P_2 \rangle$ varies over the $-0.5, +1.0$ range).

exist the peculiar situations of a Gaussian distribution (often called $\langle P_2 \rangle$ type, i.e., for $\lambda_4 = 0$) and a conic distribution. The various domains of existence for these distributions are then reported in Figure 10.

In the latter cases, and for positive $\langle P_2 \rangle$, monotonously decreasing functions are found; they are different from zero in the interval $\theta = 0.0$ to θ_0 , and they satisfy the relations

$$\begin{cases} \langle P_2 \rangle = \frac{1}{2} \cos \theta_0 (1 + \cos \theta_0) \\ \langle P_4 \rangle = \frac{1}{8} \cos \theta_0 (1 + \cos \theta_0) (7 \cos^2 \theta_0 - 3) \end{cases} \quad (63)$$

Conversely, for negative $\langle P_2 \rangle$, increasing functions are effective; they are different from zero over the $\theta = \theta_0$ to $\pi/2$ range, and they lead to the corresponding relations

$$\begin{cases} \langle P_2 \rangle = \frac{1}{2} (\cos^2 \theta_0 - 1) \\ \langle P_4 \rangle = \frac{1}{8} (\cos^2 \theta_0 - 1) (7 \cos^2 \theta_0 - 3) \end{cases}$$

therefore $\langle P_4 \rangle = \frac{1}{2} \langle P_2 \rangle (7 \langle P_2 \rangle + 2)$ (64)

Therefore, to predict the shape of the most probable distribution functions, it is mandatory to examine the solutions for positive and negative $\langle P_2 \rangle$ values, successively.

(i) Solutions for positive $\langle P_2 \rangle$ (Figure 11): In that case, according to Pottel et al.,²⁴ as $\langle P_4 \rangle$ increases, three distinct domains can be defined: a domain (I) of unimodal distributions (including the conic ones) with a minimum at 0° ; a region (II) where the distributions display a single maximum at 0° (including the Gaussian type); and a domain (III) where the functions show two maxima, one at 0° (more intense) and another one at 90° (less intense). For instance, it is noteworthy that at the point “f” (Figure 11), where $\langle P_2 \rangle = 0.5$ and $\langle P_4 \rangle = 0.608$, a distribution dominated by the $\langle P_4 \rangle$ parameter is found, as λ_2 is equal to zero at this position.

Finally, it is worthwhile to recall that the lower and higher limit curves of region II are obtained

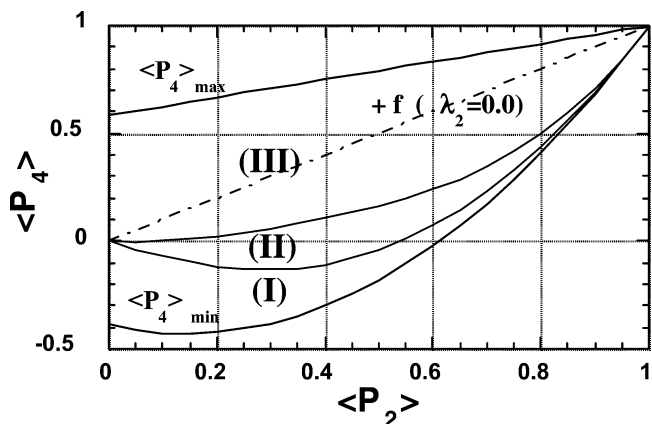


Figure 11. Various domains of the most probable orientation functions for positive $\langle P_2 \rangle$ values.

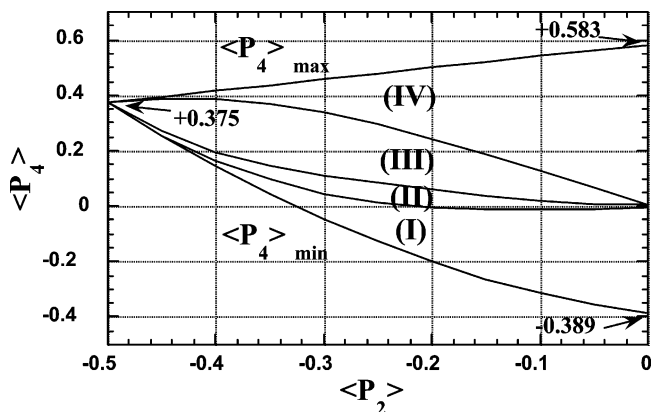


Figure 12. Various domains of the most probable distribution functions for negative $\langle P_2 \rangle$ values.

within the “information entropy” model for the particular solutions $\lambda_2 = -15/2\lambda_4$ and $\lambda_2 = 45/8\lambda_4$, respectively; these curves can be fitted with the following polynomial series:

$$\begin{aligned} \langle P_4 \rangle_{(\lambda_2 = -(15/2)\lambda_4)} &= 0.31 \langle P_2 \rangle^4 + 0.88 \langle P_2 \rangle^3 - \\ &\quad 0.16 \langle P_2 \rangle^2 - 0.03 \langle P_2 \rangle \\ \langle P_4 \rangle_{(\lambda_2 = +(45/8)\lambda_4)} &= 2.56 \langle P_2 \rangle^4 - 3.94 \langle P_2 \rangle^3 + \\ &\quad 2.42 \langle P_2 \rangle^2 - 0.04 \langle P_2 \rangle \end{aligned} \quad (65)$$

(ii) Solutions for negative $\langle P_2 \rangle$ (Figure 12):²⁵ The diagram is now slightly more complex, as four domains can be distinguished: a domain (I) of asymmetric unimodal distributions with a minimum at 90° ; a domain (II) of distributions displaying only a maximum at 90° (including the Gaussian model); and two regions (III and IV) of bimodal distributions exhibiting two maxima at 0° and 90° , with the more intense one being located either at 90° (III) or at 0° (IV).

One can easily check that, as $\langle P_4 \rangle$ increases, the three internal curves (solid lines) are obtained for the particular relations of the Lagrange coefficients, $\lambda_2 = 5/2\lambda_4$, $\lambda_2 = -10/3\lambda_4$, and $\lambda_2 = -5/12\lambda_4$, respectively. So, this leads to the following polynomial series for the various domain limits:

$$\begin{aligned}\langle P_4 \rangle (\lambda_2 = {}^5/2 \lambda_4) &= 1.198 \langle P_2 \rangle^4 - 2.776 \langle P_2 \rangle^3 + \\ &\quad 0.180 \langle P_2 \rangle^2 + 0.184 \langle P_2 \rangle \\ \langle P_4 \rangle (\lambda_2 = -{}^{10}/3 \lambda_4) &= 12.232 \langle P_2 \rangle^4 + 8.082 \langle P_2 \rangle^3 + \\ &\quad 2.388 \langle P_2 \rangle^2 - 0.047 \langle P_2 \rangle \\ \langle P_4 \rangle (\lambda_2 = -{}^5/12 \lambda_4) &= -1.182 \langle P_2 \rangle^4 + 1.634 \langle P_2 \rangle^3 + \\ &\quad 0.025 \langle P_2 \rangle^2 - 1.293 \langle P_2 \rangle \quad (66)\end{aligned}$$

From this overall discussion on the $\langle P_4 \rangle$ versus $\langle P_2 \rangle$ diagrams it is clearly demonstrated that particular attention must be paid to the regions of largest $\langle P_4 \rangle$ values, where the shape of the distribution function may change drastically for a relatively weak variation of the parameters. This is connected to the largest variances (or fluctuations) of $\langle P_2 \rangle$ observed for weak values of this coefficient, particularly in the vicinity of 0.0 and around +0.25.²⁴

Finally, in agreement with Bower,¹² it may be pointed out that from any pair of $\langle P_2 \rangle$ and $\langle P_4 \rangle$ values we can get an estimate of the high and low limits of the higher order parameter, $\langle P_6 \rangle$:

$$\begin{aligned}\langle P_6 \rangle &\geq \frac{1}{700(2\langle P_2 \rangle + 1)} [275\langle P_2 \rangle^2 + 1584\langle P_4 \rangle^2 + \\ &\quad 1620\langle P_2 \rangle \langle P_4 \rangle - 770\langle P_2 \rangle - 378\langle P_4 \rangle - 231] \\ \langle P_6 \rangle &\leq \frac{1}{175(1 - \langle P_2 \rangle)} [-275\langle P_2 \rangle^2 - 1984\langle P_4 \rangle^2 + \\ &\quad 375\langle P_2 \rangle \langle P_4 \rangle + 21\langle P_4 \rangle + 77] \quad (67)\end{aligned}$$

Using these additional relations, the validity of new experimental results (obtained from X-ray or NMR techniques, for instance) can be checked in some particular cases; one may thus obtain a better insight into the form of the most probable orientation distribution function.

3.3. Application Examples in Systems of Biaxial Symmetry

According to the "pioneering" works of Bower and Ward,¹¹⁻¹³ it turned out that any extension of the

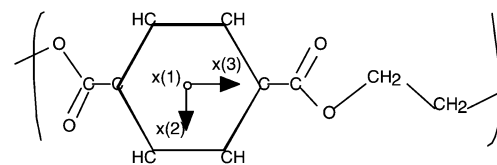
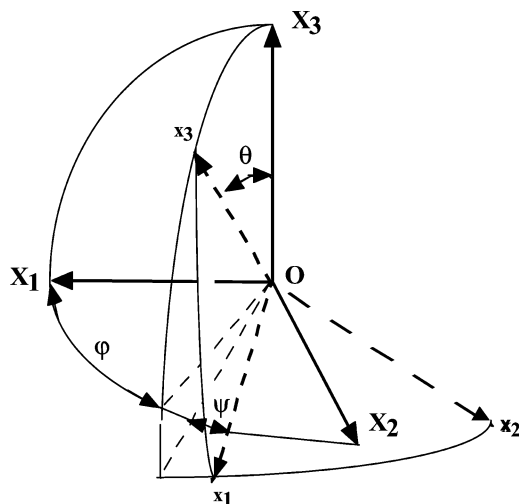
previous method to biaxially oriented films was relatively complex. Nevertheless, the vibrational infrared and Raman techniques could allow good structural characterizations and provide interesting results, more extended than those obtained from NMR or fluorescence techniques, particularly in polymer systems with a low crystallinity.

3.3.1. Biaxial Orientation in a Poly(ethylene terephthalate) (PET) Film¹¹⁻¹³

In this example, both the infrared and Raman techniques were employed in order to investigate changes in the molecular orientations and/or conformations of the benzene rings and/or the ethylenic chains within several largely stretched PET thin films prepared by extrusion from fused mixtures; these films were displaying orientation properties of biaxial symmetry. From parallel measurements by refractometry, three distinct values of the refraction indices were determined: 1.645, 1.573, and 1.541, respectively (at the sodium D line of 589.3 nm). In the following, we shall mainly examine the Raman results obtained for the benzene vibrational mode $\nu(8a)$ ($\omega(\text{C}=\text{C})$) at 1616 cm^{-1} and, comparatively, the infrared results for the modes $\nu(18a)$ (δCH) at 1017 cm^{-1} and $\nu(10a)$ (γCH) at 875 cm^{-1} .

For the mode $\nu(8a)$ ($\omega(\text{C}=\text{C})$) at 1616 cm^{-1} , thanks to the choice of the internal ring axis " $x(3)$ " parallel to the long molecular axis (along the 4-4' "para" positions), we may assume that the principal axes of the Raman tensor are coincident with the benzene axes and that the Raman tensor is again of cylindrical symmetry (Figure 13).

Under these conditions, six independent linear equations corresponding to the Raman intensities $I_{ij} = I_0 N_0 \langle \alpha_{ij}^2 \rangle = \sum_{lmn} \langle F_{lmn} \rangle A_{lmn}^{ij}$ are expected: they are functions of the five effective order parameters $\langle F_{lmn} \rangle$ and of the coefficients A_{lmn}^{ij} (see below the expressions for A , B , C , D , and E) which are second degree polynomials in α_1 and α_3 . After some cumbersome calculations, we get the following equations:



$$\text{with, } \bar{\mathbf{a}} = \begin{pmatrix} \alpha_1 & & \\ & \alpha_1 & \\ & & \alpha_3 \end{pmatrix}, \text{ and } r = \alpha_1 / \alpha_3$$

Figure 13. Definitions of the Euler angles and internal axes in the benzene rings in a PET sample.

First, from the expressions of the tensor diagonal components,

$$[\alpha_{11}] = [(\alpha_3 - \alpha_1) \cos^2 \varphi \sin^2 \theta + \alpha_1]$$

$$[\alpha_{22}] = [(\alpha_3 - \alpha_1) \sin^2 \varphi \sin^2 \theta + \alpha_1]$$

$$[\alpha_{33}] = [(\alpha_3 - \alpha_1) \cos^2 \theta + \alpha_1]$$

we obtain the following equations

$$I_{11} = \frac{I[\alpha_{11}^2]}{I_0 N_0 \alpha_3^2} \approx A + B \langle F_{2,0,0}^r \rangle + 3C \langle F_{4,0,0}^r \rangle - \frac{B}{2} \langle F_{2,2,0}^r \rangle - \frac{C}{3} \langle F_{4,2,0}^r \rangle + \frac{C}{24} \langle F_{4,4,0}^r \rangle$$

$$I_{22} = \frac{I[\alpha_{22}^2]}{I_0 N_0 \alpha_3^2} \approx A + B \langle F_{2,0,0}^r \rangle + 3C \langle F_{4,0,0}^r \rangle + \frac{B}{2} \langle F_{2,2,0}^r \rangle + \frac{C}{3} \langle F_{4,2,0}^r \rangle + \frac{C}{24} \langle F_{4,4,0}^r \rangle$$

$$I_{33} = \sum \alpha_{33}^2 = \frac{I[\alpha_{33}^2]}{I_0 N_0 \alpha_3^2} \approx A + 2B \langle F_{2,0,0}^r \rangle + 8C \langle F_{4,0,0}^r \rangle \quad (68a)$$

Similarly, from the nondiagonal tensor components,

$$[\alpha_{12}] = [(\alpha_3 - \alpha_1) \sin \varphi \cos \varphi \sin^2 \theta]$$

$$[\alpha_{31}] = [(\alpha_3 - \alpha_1) \cos \varphi \sin \theta \cos \theta]$$

$$[\alpha_{23}] = [(\alpha_3 - \alpha_1) \sin \varphi \sin \theta \cos \theta]$$

we get three additional relations

$$I_{12} = \sum \alpha_{12}^2 = \frac{I[\alpha_{12}^2]}{I_0 N_0 \alpha_3^2} \approx D + 2E \langle F_{2,0,0}^r \rangle + C \langle F_{4,0,0}^r \rangle - \frac{C}{24} \langle F_{4,4,0}^r \rangle$$

$$I_{31} = \sum \alpha_{31}^2 = \frac{I[\alpha_{31}^2]}{I_0 N_0 \alpha_3^2} \approx D - E \langle F_{2,0,0}^r \rangle - 4C \langle F_{4,0,0}^r \rangle - \frac{E}{2} \langle F_{2,2,0}^r \rangle + \frac{C}{3} \langle F_{4,2,0}^r \rangle$$

$$I_{23} = \sum \alpha_{23}^2 = \frac{I[\alpha_{23}^2]}{I_0 N_0 \alpha_3^2} \approx D - E \langle F_{2,0,0}^r \rangle - 4C \langle F_{4,0,0}^r \rangle + \frac{E}{2} \langle F_{2,2,0}^r \rangle - \frac{C}{3} \langle F_{4,2,0}^r \rangle \quad (68b)$$

Moreover, for completeness, we must add two interdependent relations arising from products of the diagonal tensor elements and defined as follows in eqs 69:

$$I_{11,33} = \frac{I[\alpha_{11}\alpha_{33}]}{I_0 N_0 \alpha_3^2} \approx (A - 2D) + (2E - B/2) \langle F_{2,0,0}^r \rangle - 4C \langle F_{4,0,0}^r \rangle + (E - B/4) \langle F_{2,2,0}^r \rangle + \frac{C}{3} \langle F_{4,2,0}^r \rangle$$

$$I_{22,33} = \frac{I[\alpha_{22}\alpha_{33}]}{I_0 N_0 \alpha_3^2} \approx (A - 2D) + (2E - B/2) \langle F_{2,0,0}^r \rangle - 4C \langle F_{4,0,0}^r \rangle - (E - B/4) \langle F_{2,2,0}^r \rangle - \frac{C}{3} \langle F_{4,2,0}^r \rangle \quad (69)$$

Provided that the ratio $r = \alpha_1/\alpha_3 = \alpha_2/\alpha_3$, which is contained in definitions of the A , B , C , D , and E coefficients, is otherwise known (equal to -0.18 in this example), we arrive again at the six unknowns of the problem, namely

$$I_0 N_0 \alpha_3^2, \langle F_{2,0,0}^r \rangle, \langle F_{4,0,0}^r \rangle, \langle F_{2,2,0}^r \rangle, \langle F_{4,2,0}^r \rangle, \langle F_{4,4,0}^r \rangle$$

Finally, all the coefficients (A to E already encountered in eqs 50) correspond in that case to simpler expressions, and they can be further simplified if the ratio r tends to zero (when $\alpha_3 \gg \alpha_1$):

$$\begin{aligned} A &= \frac{1}{15}(8r^2 + 4r + 3) \approx \frac{3}{15} \\ B &= \frac{1}{21}(8r^2 - 2r - 6) \approx \frac{-6}{21} \\ C &= \frac{1}{35}(r^2 - 2r + 1) \approx \frac{1}{35} \\ D &= \frac{1}{15}(r^2 - 2r + 1) \approx \frac{1}{15} \\ E &= \frac{-1}{21}(r^2 - 2r + 1) \approx \frac{-1}{21} \end{aligned} \quad (70)$$

The above equations deserve some general and very important comments:

(i) First, it must be underlined that these relations are similar to those already reported in various publications, including the articles due to Bower et al.,^{10,11} but non-normalized forms of the Legendre polynomials (noted P_{lmn} or Z_{lmn}) are more often used. In this respect, we recall hereafter some useful relations involving the different notations

$$\begin{aligned} \langle F_{l,m,n} \rangle &= \frac{(l+m)! (l-n)!}{(l-m)! (l+n)! (m-n)!} \langle P_{l,m,n} \rangle \\ \langle F_{l,m,0} \rangle &= \frac{(l+m)!}{(l-m)! (m)!} \langle P_{l,m,0} \rangle \end{aligned} \quad (71)$$

leading to

$$\begin{aligned} \langle F_{2,0,0} \rangle &\equiv \langle P_{2,0,0} \rangle; \quad \langle F_{4,0,0} \rangle \equiv \langle P_{4,0,0} \rangle; \\ \langle F_{2,2,0} \rangle &\equiv 12.0 \langle P_{2,2,0} \rangle; \quad \langle F_{4,2,0} \rangle \equiv 180.0 \langle P_{4,2,0} \rangle; \quad \text{and} \\ &\quad \langle F_{4,4,0} \rangle \equiv 1680.0 \langle P_{4,4,0} \rangle \end{aligned}$$

where

$$\begin{cases} \langle P_{2,2,0} \rangle = \frac{1}{4} \langle \sin^2 \theta \cos 2\varphi \rangle \\ \langle P_{4,2,0} \rangle = \frac{1}{24} \langle (-7 \cos^4 \theta + 8 \cos^2 \theta - 1) \cos 2\varphi \rangle \\ \langle P_{4,4,0} \rangle = \frac{1}{16} \langle (\cos^4 \theta - 2 \cos^2 \theta + 1) \cos 4\varphi \rangle \end{cases} \quad (72)$$

Note that similar expressions apply to $\langle P_{2,0,2} \rangle$, $\langle P_{4,0,2} \rangle$, and $\langle P_{4,0,4} \rangle$ provided the angle φ is changed to ψ . Finally, it is noteworthy that the parameter $\langle P_{2,2,2} \rangle$, which is effective in the general case of a statistical biaxial symmetry (where any Euler angle may take a random value), can be determined from additional infrared measurements (in transmission with oblique incidence, for instance); it is defined as

$$\langle P_{2,2,2} \rangle = \frac{1}{4} \langle (1 + \cos^2 \theta) \cos 2\varphi \cos 2\psi - 2 \cos \theta \sin 2\varphi \sin 2\psi \rangle \quad (73)$$

(ii) It is also noteworthy that eqs 70 become simple fractions when the condition $\alpha_3 \gg \alpha_1$ is fulfilled, and the Raman intensity expressions (eqs 68a and 68b) are also simpler:

$$I_{11} \approx 105 \frac{I[\alpha_{11}^2]}{I_0 N_0 \alpha_3^2} = 21 - 30 \langle F^r_{2,0,0} \rangle + 9 \langle F^r_{4,0,0} \rangle + 15 \langle F^r_{2,2,0} \rangle - \langle F^r_{4,2,0} \rangle + \frac{1}{8} \langle F^r_{4,4,0} \rangle$$

$$I_{22} \approx 105 \frac{I[\alpha_{22}^2]}{I_0 N_0 \alpha_3^2} = 21 - 30 \langle F^r_{2,0,0} \rangle + 9 \langle F^r_{4,0,0} \rangle - 15 \langle F^r_{2,2,0} \rangle + \langle F^r_{4,2,0} \rangle + \frac{1}{8} \langle F^r_{4,4,0} \rangle$$

$$I_{33} \approx 105 \frac{I[\alpha_{33}^2]}{I_0 N_0 \alpha_3^2} = 21 + 60 \langle F^r_{2,0,0} \rangle + 24 \langle F^r_{4,0,0} \rangle + \frac{1}{8} \langle F^r_{4,4,0} \rangle \quad (74)$$

and also

$$I_{12} \approx 105 \frac{I[\alpha_{12}^2]}{I_0 N_0 \alpha_3^2} = 7 - 10 \langle F^r_{2,0,0} \rangle + 3 \langle F^r_{4,0,0} \rangle - \frac{1}{8} \langle F^r_{4,4,0} \rangle$$

$$I_{31} \approx 105 \frac{I[\alpha_{31}^2]}{I_0 N_0 \alpha_3^2} = 7 + 5 \langle F^r_{2,0,0} \rangle - 12 \langle F^r_{4,0,0} \rangle + 2.5 \langle F^r_{2,2,0} \rangle + \langle F^r_{4,2,0} \rangle$$

$$I_{23} \approx 105 \frac{I[\alpha_{23}^2]}{I_0 N_0 \alpha_3^2} = 7 + 5 \langle F^r_{2,0,0} \rangle - 12 \langle F^r_{4,0,0} \rangle - 2.5 \langle F^r_{2,2,0} \rangle - \langle F^r_{4,2,0} \rangle \quad (75)$$

Actually, all the above eqs 74–75 will be very useful for the treatment of polarized data in any Raman microscopic measurements on thin films (see below).

3.3.2. Values of the Order Parameters in a PET Film^{11–13}

Experimentally, the authors used a 28.7 μm thick film of PET which was previously unidirectionally stretched in the ratio $\kappa = 3.5$. All the Raman recordings were performed in the 90° geometry (i.e. $2 \times 3 = 6$ experiments) and with backscattering at 180° (3 measurements) with different directions with respect to the three principal axes; nine configurations of diffusion were used with the four possible polarization combinations. This led to a total of 36 intensity measurements (with redundancies, of course) for inspection of the ring vibration at 1616 cm^{-1} , even though only six independent measurements exist in a biaxial symmetry system. Under this approach, the error possibilities and corresponding standard deviations were significantly reduced. Then, from the simultaneous resolution of the six intensity equations, the best fit final values reported in Table 3 were obtained.

Here, we must underline the excellent coincidence between values extracted from infrared (IR) and Raman experiments, the weak error bar on $\langle P_{200} \rangle$ (only 12%), but the larger uncertainties ($\approx 50\%$) on the other coefficients.

3.3.3. Estimates of the Direction Cosines

From the knowledge of the different $\langle P_{2mn} \rangle$ parameters, new relevant information about the orientations of the benzene planes and the chain axes is obtained via calculation of the direction cosines. As a matter of fact, mean values of the direction cosines between the benzene ring axes, Ox_i , and the reference

Table 3. Polarized Raman Intensity Measurements and Estimated Values of the Order Parameters in a PET Thin Film (Results Adapted from Ref 11)

Raman mode 1616 cm^{-1}	$I_{1,1}$	$I_{2,2}$	$I_{3,3}$	$I_{1,2 \text{ or } 2,1}$	$I_{1,3 \text{ or } 3,1}$	$I_{2,3 \text{ or } 3,2}$	
mean value	25.9	32.8	100.0 ^a	25.5	24.0	32.1	
rms deviation	1.0	3.1	2.7	2.8	1.9	4.0	
$\langle P_{lmn} \rangle$	$\langle P_{200} \rangle$	$\langle P_{220} \rangle$	$\langle P_{202} \rangle$	$\langle P_{222} \rangle$	$\langle P_{400} \rangle$	$\langle P_{420} \rangle$	$\langle P_{440} \rangle$
Raman	+0.25	-0.013			+0.10	-0.003	-0.007
(IR 1017 cm^{-1})	± 0.03	± 0.006			± 0.05	± 0.004	± 0.003
	(+0.23)	(-0.01)					
(IR 875 cm^{-1})			+0.03	+0.07			
Raman			± 0.01	± 0.02			

^a Value put equal to 100.0 for overall normalization.

Table 4. Comparison of the Cosinus Direction Values (Error of ± 0.02) for the Orientation of the Benzene Rings and the Skeletal Chains^a

$\langle \cos^2(x_i X_j) \rangle$	X_1	X_2	X_3
x_1	0.43 (0.46)	0.27 (0.27)	0.30 (0.27)
x_2	0.35 (0.35)	0.45 (0.46)	0.20 (0.19)
x_3	0.22 (0.19)	0.28 (0.27)	0.50 (0.54)

^a Values in parentheses were estimated from the "B" conformational model described in ref 11.

laboratory axes, OX_i , (Figure 13) are easily calculated from the following expressions:

$$\begin{aligned} \langle \cos^2(x_3 X_1) \rangle &= \frac{1}{3} - \frac{1}{3} \langle P_{200} \rangle + 2 \langle P_{220} \rangle \\ \langle \cos^2(x_3 X_2) \rangle &= \frac{1}{3} - \frac{1}{3} \langle P_{200} \rangle - 2 \langle P_{220} \rangle \\ \langle \cos^2(x_3 X_3) \rangle &= \frac{1}{3} + \frac{2}{3} \langle P_{200} \rangle \end{aligned} \quad (76)$$

$$\begin{aligned} \langle \cos^2(x_2 X_1) \rangle &= \frac{1}{3} + \frac{1}{6} \langle P_{200} \rangle - \langle P_{220} \rangle + \langle P_{202} \rangle - \langle P_{222} \rangle \\ \langle \cos^2(x_2 X_2) \rangle &= \frac{1}{3} + \frac{1}{6} \langle P_{200} \rangle + \langle P_{220} \rangle + \langle P_{202} \rangle + \langle P_{222} \rangle \\ \langle \cos^2(x_2 X_3) \rangle &= \frac{1}{3} - \frac{1}{3} \langle P_{200} \rangle - 2 \langle P_{202} \rangle \end{aligned} \quad (77)$$

$$\begin{aligned} \langle \cos^2(x_1 X_1) \rangle &= \frac{1}{3} + \frac{1}{6} \langle P_{200} \rangle - \langle P_{220} \rangle - \langle P_{202} \rangle + \langle P_{222} \rangle \\ \langle \cos^2(x_1 X_2) \rangle &= \frac{1}{3} + \frac{1}{6} \langle P_{200} \rangle + \langle P_{220} \rangle - \langle P_{202} \rangle - \langle P_{222} \rangle \\ \langle \cos^2(x_1 X_3) \rangle &= \frac{1}{3} - \frac{1}{3} \langle P_{200} \rangle + 2 \langle P_{202} \rangle \end{aligned} \quad (78)$$

Values of these direction cosinus squares are reported in Table 4, where they can be compared to those expected for the chains under the assumption of a so-called "B" conformational model. In this model it was assumed that there was no preferential orientation for the ester groups with respect to the adjacent benzene rings, with the chain axis orientation being similar to that of the C_1 – C_4 ring axis. Moreover, the terephthaloyl residue should accommodate the same conformation in the amorphous and crystalline phases, but the chains could exhibit some "gauche" defects in the glycol residues in the amorphous phase. Finally, the mean direction of the chains should be along the c axis in the crystalline parts.

It is noteworthy that all these values differ significantly from 0.33, the value expected in a totally disordered sample. Moreover, the maximum observed in $\langle \cos^2(x_3 X_3) \rangle$ confirms that the C_1 – C_4 ring axis is preferentially oriented along the stretching direction. Also, we note that $\langle \cos^2(x_3 X_2) \rangle$ is significantly larger than $\langle \cos^2(x_3 X_1) \rangle$, which indicates a more pronounced orientation perpendicular to the film plane. Similarly, the high value of $\langle \cos^2(x_2 X_2) \rangle$ confirms the previous observation. To summarize, in the PET layers we can conclude that the benzene rings, whose C_1 – C_4 axes are located closer to the $OX_1 X_3$ plane than to the

$OX_2 X_3$ one, are strongly oriented along the stretching direction. According to eqs 76, this conclusion is corroborated in the case under study by the negative sign of the $\langle P_{220} \rangle$ parameter. It should be equal to zero in a perfectly oriented sample of uniaxial symmetry. Therefore, a "biaxiality indicator" is provided by the domain of variations of $\langle P_{220} \rangle$, whose limiting values are governed by the $\langle P_{200} \rangle$ main parameter. Indeed, the following very simple inequality must always be fulfilled:

$$|\langle P_{220} \rangle| \leq \frac{1}{6}(1 - \langle P_{200} \rangle) \quad (79)$$

The limit is here equal to ± 0.125 , as $\langle P_{200} \rangle$ is equal to $+0.25$, and the inequality is well satisfied. Nevertheless, the very weak value of $\langle P_{220} \rangle$ (-0.013) provides another proof that there exists only a small tendency of the C_1 – C_4 ring axis for a preferential orientation perpendicular to the film plane. Similarly, the determined values of $\langle \cos^2(x_3 X_1) \rangle$ and $\langle \cos^2(x_3 X_2) \rangle$ confirm the above conclusions. It is worthwhile to note that the "planar orientation" of the benzene rings was otherwise confirmed in the crystalline parts from X-ray diffraction measurements. Concerning the chain parameters, the values in parentheses in Table 4 are very similar to those determined for the rings. This result shows again that, under weak stretching conditions, the chains located near the surface planes of the PET films are more likely oriented along the stretching direction. Conversely, an orientation perpendicular to the layer planes is expected to decrease under a stronger constraint, the chains being able to reorient preferentially inside the film planes. Finally, it is more tedious to discuss the exact physical meaning of the values of the $\langle P_{400} \rangle$, $\langle P_{420} \rangle$, and $\langle P_{440} \rangle$ order parameters, since all of them have been estimated from the Raman results (Table 3). From eqs 74 and the knowledge of the positive $\langle P_{200} \rangle$ coefficient, we may define the limits of their domain of existence:

$$\langle P_{400} \rangle_{\min} = -0.429 \leq \langle P_{400} \rangle \leq +1.0 = \langle P_{400} \rangle_{\max}$$

$$|\langle P_{420} \rangle| \leq \frac{3}{56} = 0.0536$$

$$|\langle P_{440} \rangle| \leq \frac{1}{16} = 0.0625 \quad (80)$$

The experimental values in the case under study are found to be equal to $+0.10$, -0.003 , and -0.007 , respectively. So, they are contained within the physically correct limits. The above values are in total agreement with the fact that the final orientational distribution function $F(\theta, \varphi, \psi)$ must be positive whatever the investigated region, as illustrated for the 1616 cm^{-1} ring vibration in Figure 14. Furthermore, these values might show a great influence on the width of the distributions (when calculated for identical φ angles). Such effects could be evidenced in a comparative study of several similar samples, but submitted to various and distinct mechanical constraints.

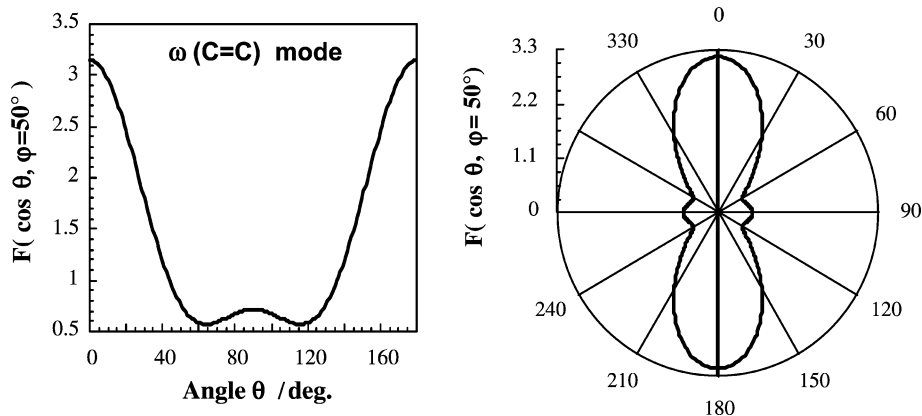


Figure 14. Shape of the final distribution function $F(\theta, \varphi, \psi)$ in PET layers obtained for the ring mode at 1616 cm^{-1} using $\varphi = 50^\circ$ (left side, normal curve variations; right side, polar plot).

3.4. Deformation Schemes, Theoretical Considerations, and Applications of Direct Methods via Internal Calibrations^{13,26–33}

3.4.1. Theoretical Considerations of the Deformation Schemes

In former models for the deformation of a polymer under stretching, it was generally assumed that the polymer was built of an assembly of isotropic transverse units, whose symmetry axes were rotating during the mechanical drawing, as lines of points in a bulk material. The polymer was actually subject to deformation at a constant volume. This scheme was called “pseudoaffine” in order to distinguish it from a more conventional “affine” model, in which it was assumed that all vectors connecting the different meeting points of a polymeric framework would necessarily be rotating and changing their length. In both models, rather complicated polynomial relations have been proposed between both order parameters, $\langle P_{200} \rangle$ and $\langle P_{400} \rangle$, and the unique stretching factor (or draw ratio κ) in an uniaxial system. Equivalently, several relations between the coefficients $\langle P_{200} \rangle$, $\langle P_{220} \rangle$, $\langle P_{400} \rangle$, $\langle P_{420} \rangle$, and $\langle P_{440} \rangle$ and the three factors κ_1 , κ_2 , and κ_3 (of course with the condition $\kappa_1\kappa_2\kappa_3 = 1.0$) were suggested in a biaxial symmetry system.

The “pseudoaffine” model was found to be quite predictive with respect to the mechanical and birefringence properties. However, a fundamental objection was raised because it was tacitly assumed that the unique axis of the structural units was coupled to the rotation axis toward the stretching direction. Actually, this coupling is not mandatory for chains which may exist in a viscoelastic regime of plastic deformation. So, under this model, the variations of both $\langle P_{200} \rangle$ and $\langle P_{400} \rangle$ parameters were first simulated by increasing functions, which gradually tend toward asymptotic values for a complete alignment,

$$\langle P_{200} \rangle = \frac{1}{2} \left\{ \frac{2\kappa^3 + 1}{(\kappa^3 - 1)} - \frac{3\kappa^{1/2} \cos^{-1}(\kappa^{-3/2})}{(\kappa^3 - 1)^{2/3}} \right\} \quad (81)$$

$$\langle P_{400} \rangle = \frac{1}{8} \left\{ 3 - \frac{30\kappa^3}{(\kappa^3 - 1)} \left[1 - \frac{\cos^{-1}(\kappa^{-3/2})}{(\kappa^3 - 1)} \right] + \frac{35\kappa^6}{(\kappa^3 - 1)^2} \left[1 + \frac{1}{2\kappa^3} - \frac{3 \cos^{-1}(\kappa^{-3/2})}{2(\kappa^3 - 1)} \right] \right\} \quad (82)$$

In contrast, in the “affine” deformation model of molecular networks, whose origins are in viscoelasticity theories, it is acknowledged that an ideal network of chains can be built of several segments and of rotating links, with each chain containing a number of bondings N . Under these conditions, different relatively simple expressions have been proposed for the variations of both order parameters:

$$\langle P_{200} \rangle = \frac{1}{5N^2} \left(\kappa^2 - \frac{1}{\kappa} \right) + \frac{1}{25N^2} \left(\kappa^4 + \frac{\kappa}{3} - \frac{4}{3\kappa^2} \right) + \dots \quad (83)$$

and

$$\langle P_{400} \rangle = \frac{3}{175N^2} \left(\kappa^4 - 2\kappa + \frac{1}{\kappa^2} \right) + \frac{216}{13475N^3} \left(\kappa^6 - \frac{4\kappa^3}{5} - \frac{7}{5} + \frac{6}{5\kappa^3} \right) + \dots \quad (84)$$

From the above equations, and in good agreement with experiments, in the “pseudoaffine” model we expect monotonic increases for $\langle P_{200} \rangle$ and $\langle P_{400} \rangle$ over a restricted range of draw ratios (with, however, very low values for $\langle P_{400} \rangle$ under weak stretching), but we expect more drastic variations in the “affine model” (Figure 15). However, an important criticism of the latter model comes from the fact that the extension limits of a molecular skeletal system could reach very large values, a situation which is not at all physically meaningful.

Therefore, Nobbs and Bower²⁶ have proposed another version, denoted “modified affine”, in which it is assumed that a chain may remain rotating, exactly as a rigid unit, and may still accommodate an extended “all-trans” form. Thanks to this last model, which fits the data quite well, correct interpretations of the Raman spectra, refractometry data, and polarized fluorescence results on hot-stretched PET films and on PMMA amorphous films were possible. Nevertheless, it is necessary to take into consideration a

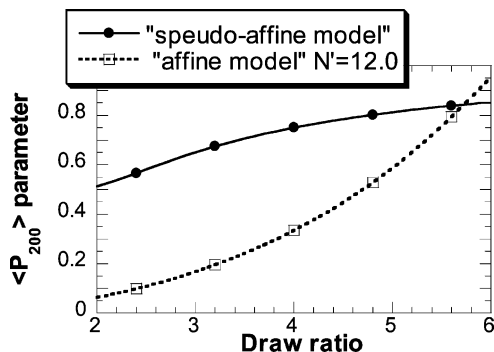


Figure 15. Variations of the $\langle P_{200} \rangle$ coefficient versus the draw ratio ($\kappa = 2-6$) in the "pseudoaffine" and "affine" ($N = 12.0$) models, respectively (eqs 81 and 83).

distribution of N values as a function of κ . Indeed, there is no sound argument which justifies that molecular entanglements of end crossed chains, not totally extended, would be able to remain in a deformation "affine" regime.

Finally, Raha and Bowden²⁷ have proposed an alternative deformation scheme and suggested that the number of cross-links decreases systematically as the draw ratio increases. It is then assumed that the reduction in the number of cross-links per unit volume N , that is, the number of molecular entanglements, is proportional to the degree of deformation. This hypothesis leads to the relations

$$\delta N \approx N(\kappa - 1)$$

and

$$N = N_0(t) \exp[-(\kappa - 1)] \quad (85)$$

where the number N_0 , or cross-link density, is a function of the temperature (t) and corresponds to an undistorted state (large number at low temperature). Therefore, the simplest approach, which Raha and Bowden adopted, has been to link the previous eq 85 to the random link network deformation model. Considering essentially the first term of eq 83, they have proposed the useful approximate expression

$$\langle P_{200} \rangle = \frac{1}{5N_0} \left(\kappa^2 - \frac{1}{\kappa} \right) \exp[-(\kappa - 1)] \quad (86)$$

It must be recalled that, even though this model is quite successful in a curve-fitting exercise of various experimental results from birefringence and/or optical data obtained on different systems under stress, it is based on a purely empirical procedure. New theoretical developments have still to be established to better explain the deformation of any molecular network in the absence of crystallization effects. The numerous experimental results of high quality obtained during these last years should promote shortly such works. This will be very useful to all scientists involved in studies of the physical and rheological properties of polymer systems.

3.4.2. Applications of Direct Methods via Internal Calibrations

Several very nice pieces of work and examples of polarized Raman studies can be found in the recent

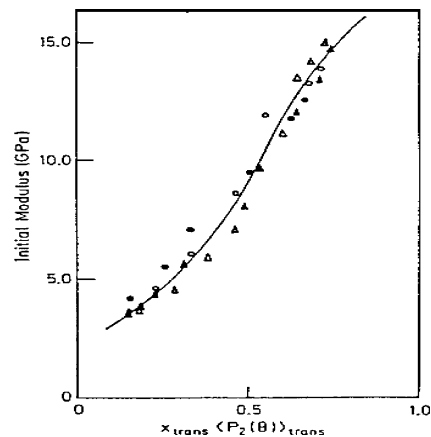


Figure 16. Relation between the Young modulus and the overall parameter " $x_{\text{trans}} \langle P_2 \rangle_{\text{trans}}$ " in uniaxially stretched PET films. (Reproduced with permission from ref 13. Copyright 1985 Springer-Verlag GmbH & Co.)

literature, but they are essentially for systems of uniaxial symmetry. In these studies, the authors have provided clear evidences for the existence of correlations between the values of the first-order parameters of even-parity and the stretching ratio and/or the mechanical or birefringence properties. As illustrative examples, we shall emphasize below some excellent literature results concerning samples built of poly(ethylene terephthalate) (PET) polymer layers, of polyethylene (PE) tubes, of polyester fibers, and of industrial compounds such as polyvinyl halide derivatives (PVC and PVF2) and the isotactic polypropylene (isoPP) polymer.

3.4.2.1. Anisotropic Mechanical Properties of PET Thin Films.¹³ In such uniaxially oriented samples it has been demonstrated that the Young modulus along the stretching direction was not directly correlated to the orientation function of the amorphous part. Nevertheless, a good correlation has been established with the overall parameter " $x_{\text{trans}} \langle P_2 \rangle_{\text{trans}}$ " (Figure 16), where x_{trans} indicates the proportion of segments in the "trans" conformation. It was thus concluded that the modulus was mainly dependent on the proportion of extended chains in their "trans" conformation, whatever their surrounding in the amorphous and crystalline parts. In the amorphous state, the "trans" sequences could stabilize the overall structure and play a role similar to that of fibers inside a composite material.

Other layered films oriented with a biaxial symmetry ordering were also investigated by mechanical means, and in particular, the nine independent elastic constants were determined for a sample stretched with $\kappa = 5.0$. As discussed in a preceding section, the elastic constant values were in agreement with a chain alignment and a preferential, although incomplete, orientation of the principal axis (x_3) of the benzene rings and of the associated residus. Moreover, these values provided evidences for the existence of shearing forces in the (1,2) and (2,3) planes. However, these particular results still remain "case studies", and similar relevant approaches should be carried out on other systems. In this respect, it is worth noting that Archer and Fuller²⁸ have recently developed a new polarization modulation laser Ra-

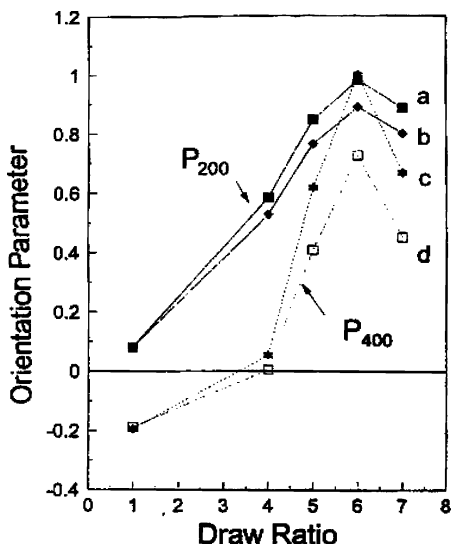
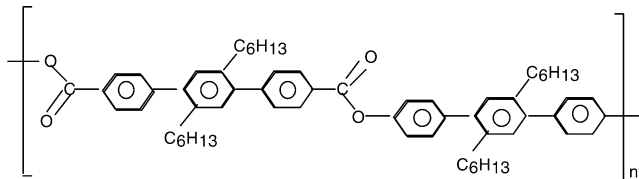


Figure 17. Variations of the parameters $\langle P_{200} \rangle$ and $\langle P_{400} \rangle$ as a function of the draw ratio, κ , in a PE sample, extracted from (a and c) the tensor elements α_{ZZ} , α_{ZY} , and α_{YY} and (b and d) the element α_{ZZ} . (Reproduced with permission from ref 29. Copyright 1996 Society for Applied Spectroscopy.)

man scattering technique, to investigate the stress and refractive index tensors in thin amorphous films and in the melt state of a polyisobutylene sample. They succeeded in measuring simultaneously the time dynamics of the optical “stress” responses to a mechanical constraint, that is, responses in both birefringence and dichroism. However, the experimental optical setup and theoretical analyses for a such dynamical study are rather intricate, and they still remain a matter for academic research laboratories.

3.4.2.2. Use of a Colored Dye Doping as a Probe of the Orientation in Amorphous PE²⁹. To probe the degree of orientation in uniaxially stretched polyethylene tubes, Everall and co-workers²⁹ have taken advantage of the clever idea to incorporate a very low quantity (0.05% wt/wt) of a linear absorbing dye, the “diphenyl 1,8-octatetraene” of chemical formula $\Phi-(C=C)_4-\Phi$, into the polymer before

Chart 1. Molecular Structure of the Polyester PES 3:3/C6



extrusion and stretching (i.e. located mainly in the amorphous parts). This dye gives rise to very intense resonance Raman signals (in particular, for the modes $\omega(C=C)$ at 1574 and 1582 cm^{-1}). The polarized Raman spectra, I_{ZZ} , I_{ZY} , and I_{YY} , recorded under stretching and after a thermal annealing allow us to get estimates of the parameter orders $\langle P_{200} \rangle$ and $\langle P_{400} \rangle$ and to correlate their variations to the draw ratio; this has been accomplished over the whole range of drawing, $\kappa = 1.0-7.0$ (Figure 17). It is thus demonstrated that the amorphous parts as well as the crystalline phases are strongly oriented under the constraint, since $\langle P_{200} \rangle$ is found to be nearly equal to +1.0; nevertheless, the crystalline parts appear to relax significantly under annealing (−30%).

This “dye doping method” is very efficient and can be generalized to other systems, in particular to systems in which it is very difficult to characterize isolated vibrational modes due to only the specific amorphous phase.

3.4.2.3. Molecular Orientations in Polyester Films As Studied by Raman, FTIR, and X-ray Techniques.³⁰ Here, the authors have investigated a bulky polyester containing para-terphenyl chains with *n*-hexyl substituents in the side-chain position, so that they used the reference name PES 3:3/C6 (Chart 1). Different 90° geometry scattering setups were employed with the sample in a vertical, horizontal, or oblique position, to probe several polarizability tensor elements. From inspection of the 1616 cm^{-1} mode due to the benzene rings, they have obtained a very good correlation between the variations of the Raman intensity ratio I_{HV}/I_{VV} and the stretching coefficient (Figure 18).

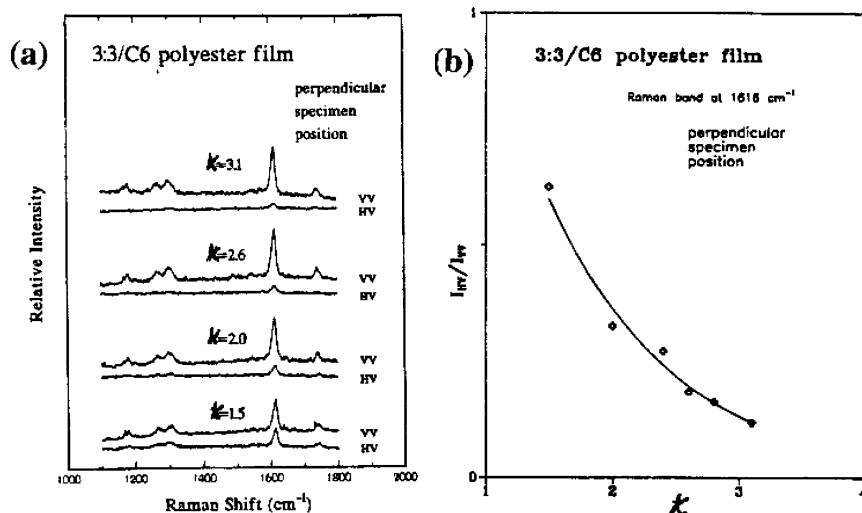


Figure 18. (a) Polarized Raman spectra, VV and HV, of a PES 3:3/C6 film in the perpendicular specimen position under various stretching conditions. (b) Relation between the depolarization ratio I_{HV}/I_{VV} for the 1616 cm^{-1} band and the stretching coefficient, κ . (Reprinted with permission from ref 30. Copyright 1996 American Chemical Society.)

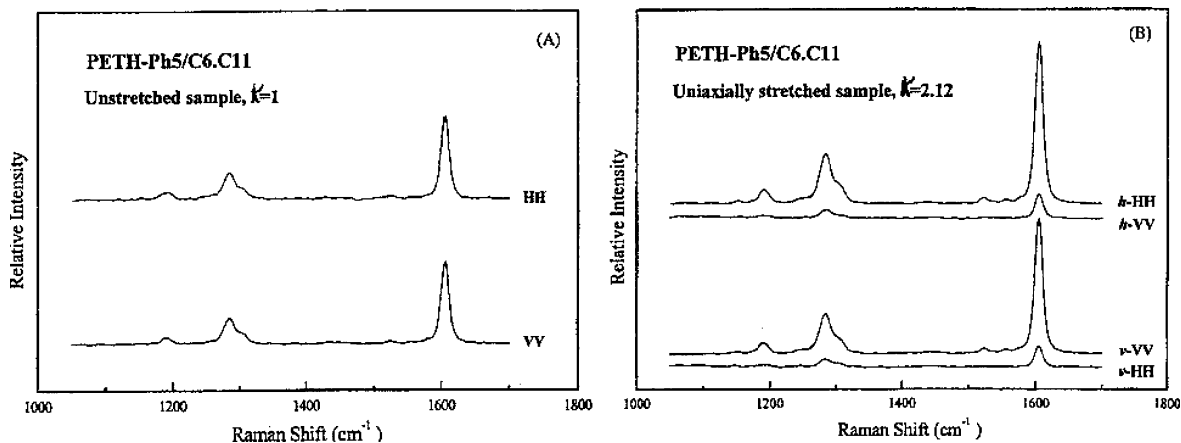
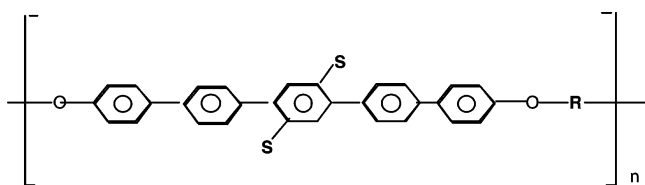


Figure 19. Polarized Raman spectra of a PETH–Ph5/C6.C11 film, before (A) and after (B) uniaxial stretching ($\kappa = 2.12$); the v - and h -symbols refer to the stretching axis oriented either in the parallel (v) or the perpendicular (h) direction in the laboratory system; they indicate the orientation of the sample. (Reprinted with permission from ref 31. Copyright 1999 American Chemical Society.)

Chart 2. Molecular Structure of Polyethers (PETH) with $S = C_6H_{13}$, OC_6H_{13} , or $C_{12}H_2$ and $R = C_7H_{14}$, C_9H_{18} , $C_{10}H_{20}$, or $C_{11}H_{22}$



Furthermore, from a review comparison of various results obtained using three techniques, Raman, FTIR, and X-ray, the high sensitivity of the vibrational methods with respect to the different molecular segments was confirmed. In contrast, the wide angle X-ray diffraction technique provides information only on the more extended organized domains; this leads generally to larger $\langle P_{200} \rangle$ values. Finally, it was demonstrated in this study that the cylindrical symmetry could be applied with success to the Raman tensor of the investigated modes, so that this kind of bulky polymer could be equivalently treated as a rodlike system.

3.4.2.4. Molecular Orientations in Blue Luminescent Rigid–Flexible Polymers.³¹ Here, we are concerned with aromatic and aliphatic polyethers (PETH; Chart 2) containing in the main chain not only S-disubstituted para-quinquephenyl groups (with $S = C_6H_{13}$, OC_6H_{13} , or $OC_{12}H_{25}$) but also alkylene groups (with $R = C_7H_{14}$, C_9H_{18} , $C_{10}H_{20}$, or $C_{11}H_{22}$). On one hand, the substituting groups are responsible for the filmogenic property and the solubility behavior at a temperature where the polymers are thermally stable. On the other hand, the polymers exhibit blue light emission and photoluminescence, a photophysical property which is strongly dependent on the molecular orientations and offers new perspectives to prepare interesting optical materials.

The polarized Raman spectra of uniaxially stretched PETH films of pure polyethers and of blends diluted ($\approx 1\%$) in isopropylene were investigated; the films were prepared from hot solutions (130°C), dried under vacuum, and, finally, put under pressure at 220°C . The parameter orders $\langle P_{200} \rangle$ and $\langle P_{400} \rangle$ were

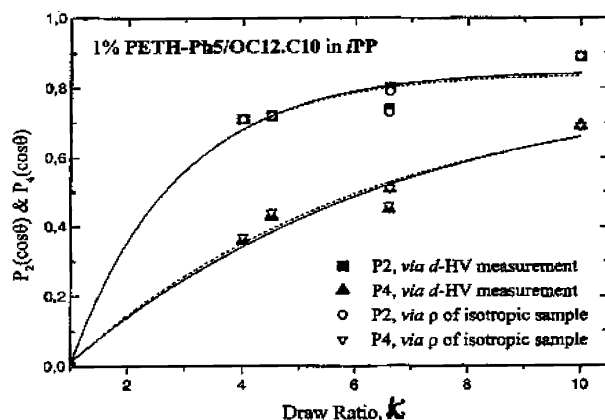


Figure 20. Variations of the parameters $\langle P_{200} \rangle$ and $\langle P_{400} \rangle$ of the mode at 1605 cm^{-1} , for a polyether diluted (1%) in polypropylene, as a function of the stretching ratio. (Reprinted with permission from ref 31. Copyright 1999 American Chemical Society.)

then determined for the ring mode at 1605 cm^{-1} , and their values presented good correlations with the stretching ratio, over the wide domain $\kappa = 1.0\text{--}10.0$ (Figures 19 and 20).

Furthermore, quite different orientational behaviors were evidenced in comparative photoluminescence studies, but only rather weak dichroic ratios were noted. Nevertheless, the diluted blends in isopropylene appeared always in Raman and photoluminescence as the best oriented systems, so that it was argued that the lateral interchain interactions were probably minimized in the blends. Such results open new interesting routes for potential applications, particularly in polarized blue light emission properties.

3.4.2.5. Molecular Orientations in Industrial PVC Samples.^{32,33} Industrial PVC samples containing $\approx 5\%$ additives, such as stabilizers and lubricants but not plasticizers, were uniaxially stretched and investigated by specular reflection in FTIR and by resonance Raman in the backscattering geometry, using various sample orientations and light-beam polarization configurations. The resonantly enhanced Raman bands at 1127 and 1515 cm^{-1} (Figure 21) are assigned to polyene segments arising from a dehy-

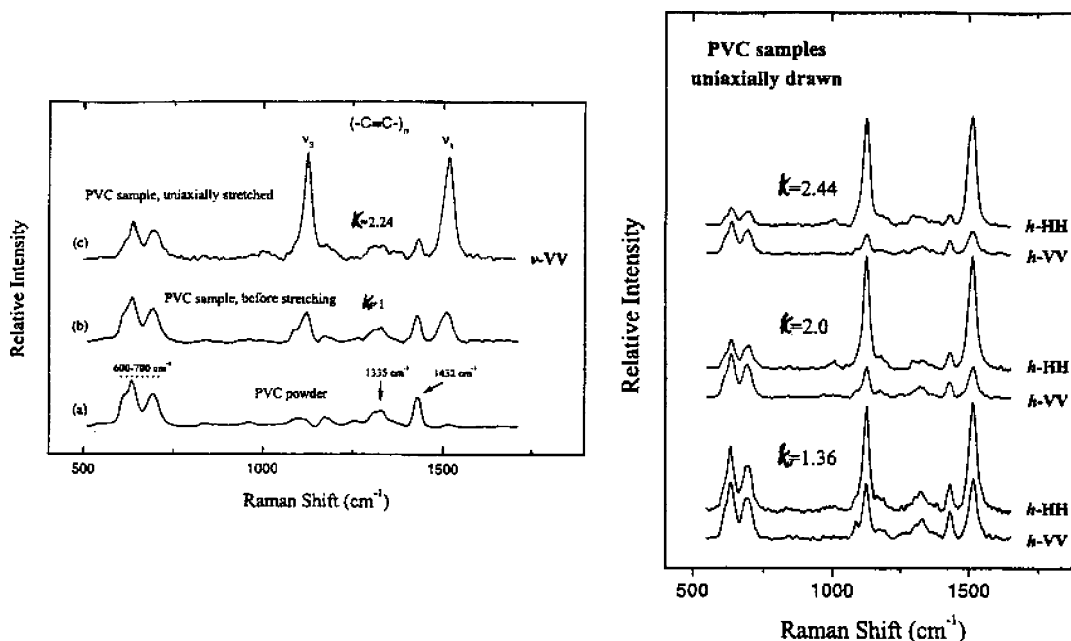


Figure 21. (left) Raman spectra in the ν -VV configuration of a PVC powder (a) and of an industrial sample, before (b) and after (c) uniaxial stretching. (right) Polarized Raman spectra in the h -HH and h -VV configurations of a PVC sample of uniaxial symmetry under various draw ratios, κ . (Reprinted with permission from ref 32. Copyright 2000 American Chemical Society.)

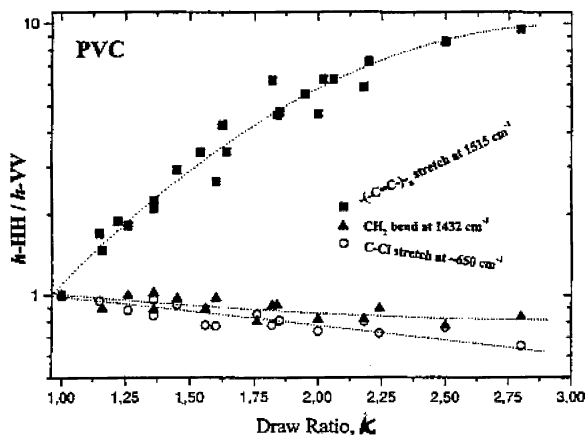


Figure 22. Polarization ratios " h -HH/ h -VV" in PVC as a function of the ratio (λ or κ) for the modes ν (C=C) at 1515 cm^{-1} , δ (CH₂) at 1432 cm^{-1} , and ν (C-Cl) at 650 cm^{-1} . (Reprinted with permission from ref 32. Copyright 2000 American Chemical Society.)

drochlorination reaction in the PVC sample and/or from a partial thermal degradation. They represent good probes to determine the first even-parity order parameters. Once again, these conjugated "all-trans" polymer segments of cylindrical symmetry were used as the "orientation indicator" of the amorphous region, and excellent correlations between the intensity ratio of the indicator and the stretching factor were established. In contrast, it is remarkable that other internal vibrations of PVC, such as the δ (CH₂) or ν (C-Cl) modes, were to a large extent less sensitive (Figure 22).

Under these conditions, the authors claimed that it was possible to take advantage of the properties of these samples to establish calibrations using the intensity variations of the ratio "intensity(sensitive mode)/intensity(unsensitive mode) as a function of

(P_{200}), and to determine in-situ and in real-time the stretching coefficient values. These concepts were actually applied by the authors³³ to PVC and PVF2 industrial polymers and to isotactic PP samples containing ≈ 0.1 wt % 1,8-diphenyloctatetraene (DPOT) absorbing dye. Some polarized Raman spectra and correlation curves concerning a PVC sample are reported in Figure 23.

3.4.2.6. In-Line Estimate of the Molecular Orientations in Polypropylene Fibers.³⁴ Under the same context of in-situ application studies, Paradkar and co-workers³⁴ have recently followed the intensity variations of two bands in the polarized Raman spectra of the isotactic polypropylene fibers, iso-PP. They thus proposed a method for in-line measurements in a compact pilot melt-spinning line, containing a feed roll, a draw roll, and a relax roll (Figure 24). The measurements of the intensity ratio for two Raman modes at 841 and 809 cm^{-1} (ρ (CH₂) and ν (C-C) coupled vibrations) in the fibers under various stretching ratios (in the 1.5–4.0 range) gave rise to very nice correlations with other birefringence data (Figure 25); moreover, the effects of sample throughput and take-up velocity on the polarized Raman spectra (i.e. on the crystallinity of the polymer) were monitored in real-time.

Definitely, the very sensitive Raman technique is well adapted (in the above example the error is only a few 1/1000 on the birefringence) and allows a rapid fabrication control. A single polarized Raman spectrum recorded on a restricted spectral domain appears sufficient!

One may thus expect that similar and new spectroscopic methods for characterization purposes will be developed during the next few years.

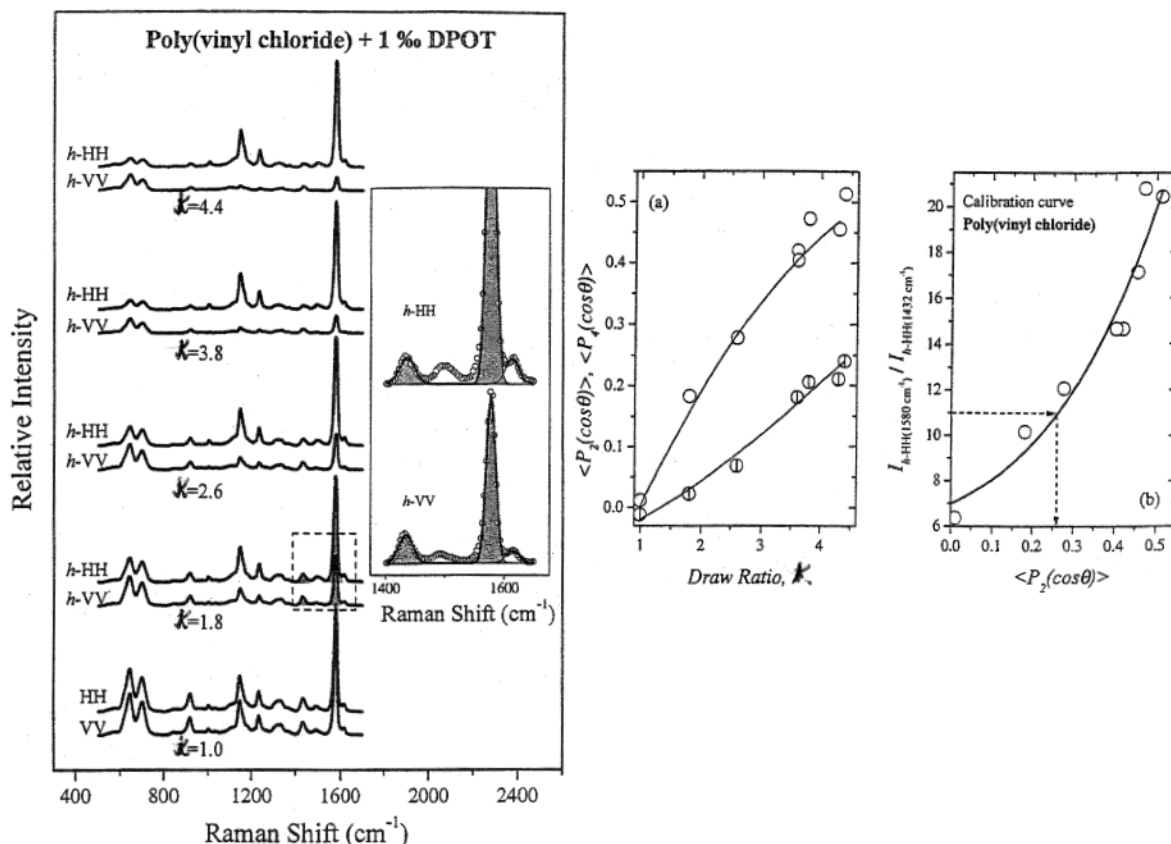


Figure 23. (left) Different polarized Raman spectra of PVC with a zoom on the 1400–1600 cm^{-1} region for $\kappa = 1.8$; (right) variations of the parameters $\langle P_{200} \rangle$, $\langle P_{400} \rangle$ calculated from the dye signal at 1580 cm^{-1} and calibration curve of the experimental ratio “h-HH(1580)/h-HH(1432)” as a function of $\langle P_{200} \rangle$. (Reproduced with permission from ref 33. Copyright 2002 Society for Applied Spectroscopy.)

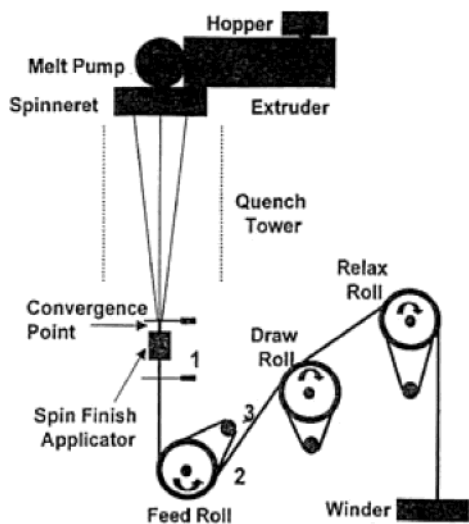


Figure 24. Schematic design of a compact pilot melt-spinning line. (Reproduced with permission from ref 34. Copyright 2001 Society for Applied Spectroscopy.)

4. Polarization Measurements in Confocal “Micro-Raman” Spectrometry

4.1. Coupling of an Optical Microscope—Experimental Considerations

The coupling of a high grade optical microscope with a large numerical aperture lens, $NA \approx 0.9$ – 0.5 , and with a bright-light efficient spectrometer needs great care to perform accurately Raman intensity

measurements, even in the presence of a nonabsorbing sample.^{4,35–38} As a matter of fact, the optical light path of the laser beam exciting a sample, illustrated in Figure 26, includes a semitransparent dichroic plate or a notch filter (in the more modern instruments), a microscope objective lens to focus the laser, and a microscope sample stage to control the sample displacements. Therefore, different experimental constraints must be overcome at these levels, and they mainly concern the properties of the notch filter, the choice of the objective lens, and, finally, the transmission property and the optical quality of the sample surface.

4.1.1. Semitransparent Plate or Notch Filter

In previous old instruments the beam-splitter was a dielectric plate inclined at 45° with respect to the laser beam. It had a low reflection coefficient (≈ 10 – 20%) of the incident light and, consequently, a high transmission (90 – 80%) in order to favor the scattered intensity.^{39,40} Such a beam-splitter induced generally undesirable intensity variations and depolarization effects, so that in modern micro-Raman instruments a notch filter has definitely replaced this plate. The notch filter is used both to reflect the incident laser light toward the microscope objective, with $\approx 90\%$ efficiency, and to transmit the backscattered Raman radiation with the same efficiency to the instrument spectrograph. It is a very neutral optical element working in a nearly normal incidence (Figure 27), and its reflection and transmission factors are indepen-

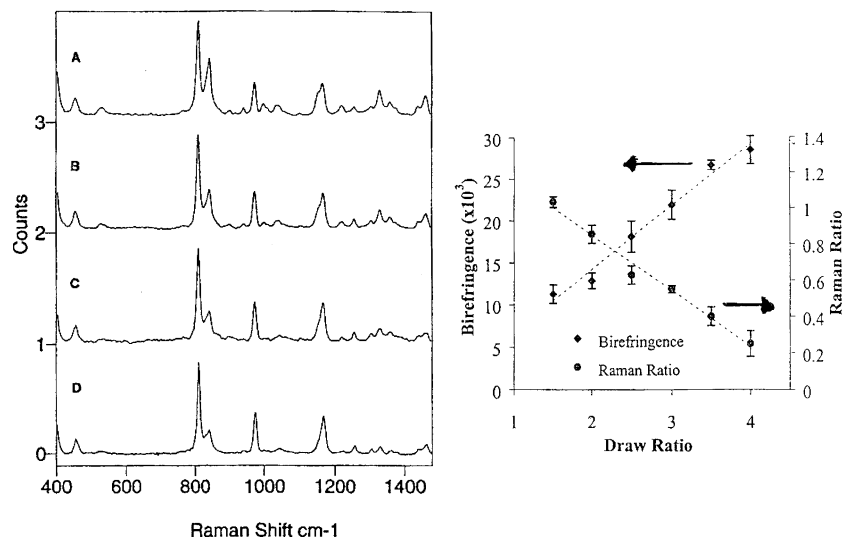


Figure 25. (left) Some typical on-line VV polarized Raman spectra of polypropylene fibers with different draw ratios measured at the midpoint between the feed and draw rolls (position 3 in Figure 24): the fibers were extruded at a rate of ~ 4.0 g/min; the take-up speed was 200 m/min, and the fibers were drawn by appropriately varying the speed of the draw roll; stretching ratio values were 1.5 (A), 2.5 (B), 3.0 (C), and 3.5 (D), respectively. (right) Plot of the draw ratio as a function of the Raman intensity ratio and the birefringence in polypropylene fibers. (Reproduced with permission from ref 34. Copyright 2001 Society for Applied Spectroscopy.)

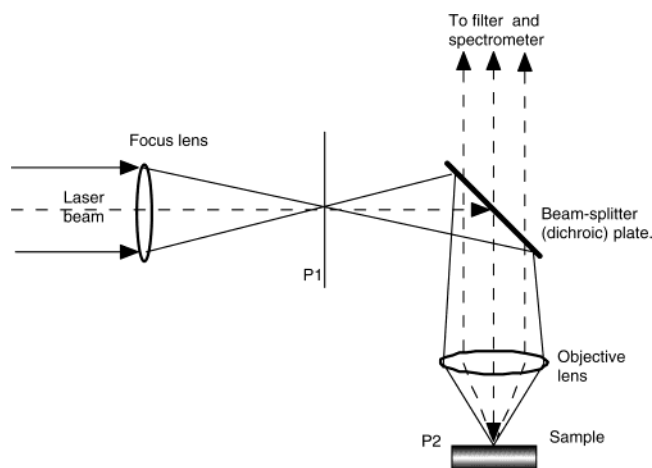


Figure 26. Beam-light path to focus a laser on the sample surface using an optical microscope.

dent of the polarization direction of both the incident and backscattered light.

Then, according to the optical scheme described in Figure 27, no intensity corrections are needed in the polarization Raman recordings, but an analyzer plate and a scrambler located in front of the entrance slit of the spectrometer are still necessary to analyze the scattered light and to correct for the response of the spectrograph grating, respectively.

It is very important to note that any notch filter must be specially designed for a single exciting laser radiation and that, for special application and efficient elastic light rejection, particular filters built of holographic thin index gratings contained in ≈ 60 μm thick layers of bichromate gelatine were recently built.⁴¹ In contrast to the dichroic plates, this type of holographic filter (designed for the 632.8 nm line of an He–Ne laser) displays a very high transmission coefficient of 80–90% at $\approx \pm 500$ cm^{-1} (as shown in Figure 28) and a reflectivity larger than 90% and 50% for the incident light polarization in

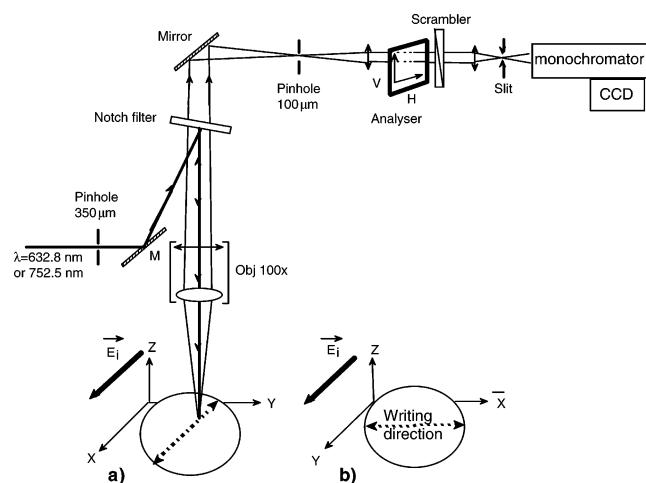


Figure 27. Experimental setups for recording polarized micro-Raman spectra from a uniaxially oriented sample: measurements of (a) the $Z(XX)Z$ and $Z(XY)Z$ spectra in the first configuration, and (b) the $Z(YY)Z$ and $Z(YX)Z$ spectra in the second configuration.

the perpendicular (\perp) and parallel (\parallel) directions, respectively; this justifies the choice of the perpendicular reflectivity setup in the above confocal setup of Figure 27.

Finally, when used in conjunction with another thin-band notch filter, generally located in front of the entrance slit of the spectrometer, such high quality filters allow us to record excellent Raman spectra even in the low wavenumber range, a region generally quite difficult to investigate.

4.1.2. Objective Lens: How To Make the Best Choice?

First, it is worth recalling that the “numerical aperture” NA of a lens objective is defined by the sine of the maximum angle of half-aperture,

$$NA = n \sin(\theta_m) \quad (87)$$

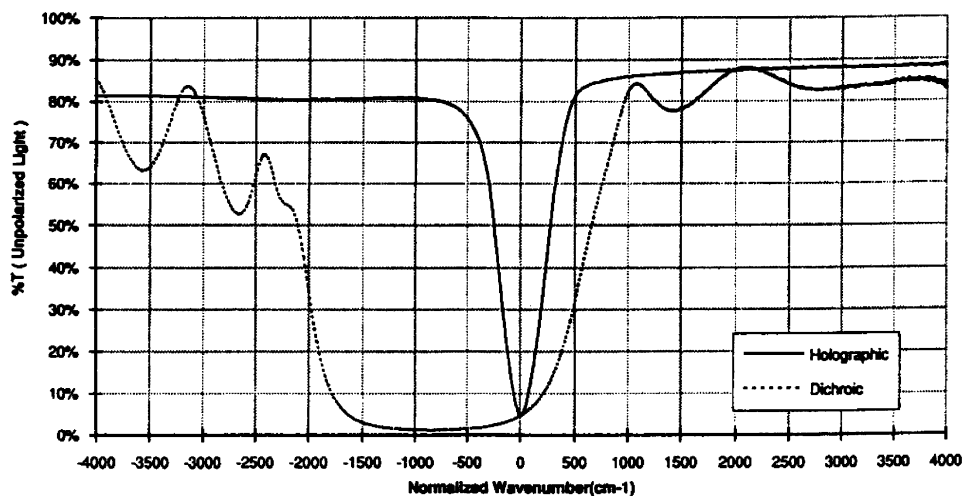


Figure 28. Transmission at near 632.8 nm of a holographic (full lines) and a dichroic (dashed lines) beam-splitter plate under the incidence angle of 45°. (Reproduced with permission from ref 41. Copyright 1992 Society Applied Spectroscopy.)

Table 5. Optical Properties of Some Commonly Used Objective Lenses (at $\lambda_0 = 632.8$ nm)

half-angle aperture (θ_m)/deg	33.4	39	48.6	53.1	64.2	71.8
NA = $n \sin(\theta_m)$	0.55	0.63	0.75	0.80	0.90	0.95
working distance (f)/mm	8.1	6.5	0.38 (5.0)	3.2	0.21 (2.5)	0.37 (1.6)
objective lens type (notation)	50X LWD	50X UTK	50X MPlan	100X LWD	100X MPlan	100X MSPlan
aperture photo: $fD = (2 \tan(\theta_m))^{-1}$	0.76	0.62	0.44	0.375	0.242	0.164
D_{\max} spot (@632.8 nm)/ μm	1.40	1.22	1.03	0.96	0.86	0.81
"waist" $d = (4\lambda_0/\pi) (fD)/\mu\text{m}$	0.61	0.50	0.35	0.30	0.19	0.13
"depth of focus" ($T = 0.86\%$) $\approx 4\lambda_0/(NA)^2/\mu\text{m}$ ($T = 0.86$ @ 1/e)	8.4	6.4	4.5	3.95	3.12	2.80

and the increase of NA is related to the increase either in the lateral resolving power of the lens (y) or, equivalently, in the minimum diameter ($D = 2y$) of the light spot limited by the diffraction phenomena:

$$y = \frac{0.61\lambda_0}{NA}$$

or, equivalently,

$$D = 2y = \frac{1.22\lambda_0}{NA} \quad (88)$$

In this respect, some characteristic geometric and optical properties of several typical "dry" objective lenses are summarized in Table 5.

For instance, using a high numerical aperture lens of NA = 0.95 and the wavelength $\lambda_0 = 632.8$ nm, the visual distinction between two points will take place for a minimum distance of 0.81 μm , a distance imposed by the diffraction limits. Furthermore, if the shape of the sample implies no constraint on the frontal distance or "working distance" (WD), it will be advantageous to use a plane achromatic field objective of small focal length and of high NA. The choice of the objective is thus very important and crucial for the incident intensity distribution, as the scattered intensity collected over the solid angle Ω will be proportional to

$$\frac{\Omega}{4\pi} = \frac{2\pi(1 - \cos \theta_m)}{4\pi} = \frac{(1 - \cos \theta_m)}{2} \quad (89)$$

Table 6. Intensity Variations of the Band at 520 cm^{-1} of a Silicium Plate Using Different Objectives (Adapted from Ref 42)

objective lens	100X	50X	ULWD 50X	ULWD 20X
NA	0.95	0.75	0.55	0.40
WD = working dist/mm	0.37	0.38	8.1	11.0
measured intensities/a.u.	14700	9900	5000	1900
rel intensities/%	100	67	34	9
theor rel intensities/%	100	62	34	7

Depending on whether the samples are absorbing or transparent, it is thus obvious that the performances of a particular objective will be markedly different.

4.1.3. Strongly Absorbing Samples⁴²

With strongly absorbing materials the laser beam is not penetrating inside the samples, and only the Raman spectrum of the surface is recorded. The collected Raman signal is therefore maximum using the highest NA objective lens. Experimentally, this is nicely verified by the intensity variations of the band at 520 cm^{-1} of a silicium plate, as reported in Table 6, where intensity data with four distinct objectives are compared.

Note that if the microscope is used in conjunction with a diaphragm of spatial resolution (particularly in a confocal optical setup), quite similar intensity variations will be found. Differences between the observed and theoretical percentage values (%) in Table 6 are thus essentially due to variations in the transmission factor of the objectives.

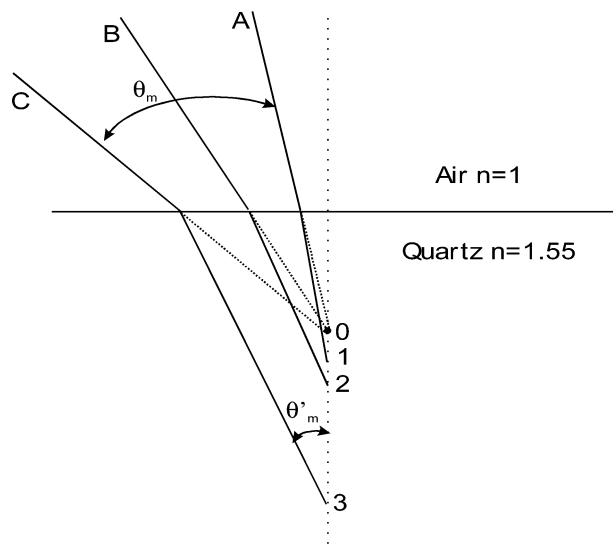


Figure 29. Optical paths at a plane interface of a quartz sample ($n = 1.55$).

Table 7. Raman Intensity Measurements for the ν_1 Band of Quartz (Adapted from Ref 42)

objective lens	100X	50X	ULWD 50X	ULWD 20X
intensity without spatial filter	4900	9700	7000	11500
intensity with spatial filter (400 μm)	900	3100	2500	4300

4.1.4. Weakly Absorbing Samples⁴²

In contrast, with weakly absorbing samples the laser beam penetrates inside the sample and one must take account of its refraction index, as the optical path is modified according to the Fresnel relation

$$\sin(\theta_m')_{\text{effective}} = \frac{1}{n} \sin(\theta_m) \quad (90)$$

The marginal and paraxial rays do not converge to the same position, giving rise to longitudinal spherical aberration. These fundamental and drastic effects are schematically illustrated in Figure 29, using for instance a quartz sample ($n = 1.55$).

Under these conditions, if the ray "B" is the marginal ray for an ULWD 20X objective ($\text{NA} = 0.4$), the light will be concentrated into a small volume and will give rise to an intense Raman spectrum. Conversely, if we use a 50X lens ($\text{NA} = 0.75$), the ray "C" will now be the marginal one, and the laser irradiance will be spread over a larger volume. Only a weak fraction of the beam will be efficient for Raman scattering, because of the limited field depth of the instrument. In these cases, additional drastic effects can be expected when using a spatial resolution diaphragm. As indicated in Table 7, this is actually observed on the intensity results for the quartz signal at 464 cm^{-1} due to the ν_1 totally symmetric mode of A_1 symmetry.

4.2. Intensity Measurements with Transparent Samples

Generally, the transparency and surface properties of a sample are the main factors controlling not only

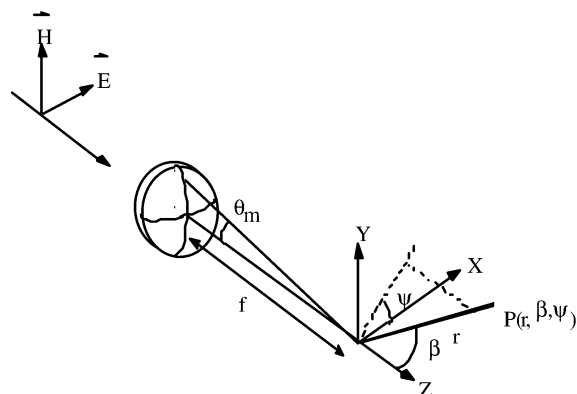


Figure 30. Notations for the illumination angles in the focal plane of a microscope lens: the dimensionless optical coordinates of the point P are $u = (2\pi/\lambda_0)z \sin^2 \theta_m$ and $v = (2\pi/\lambda_0)(x^2 + y^2)^{1/2} \sin \theta_m$.

the incident energy densities, which are radially and axially distributed within the focus region, but also the scattered energy densities. In theory, the intensity of a Raman signal scattered by a sample volume V and collected over a solid angle Ω is given by the following general relation,

$$\text{int} \approx C \int_V \int_{\Omega} |E_{\text{inc}} \alpha_{IJ} E_{\text{scatter}}|^2 d\Omega dV \quad (91)$$

where C is a constant, E_{inc} and E_{scatter} are the moduli of the electric field vectors, and α_{IJ} are the components of the polarizability derivative tensor. Such calculations, which take into account the objective effects, are very complex, and they have originally been developed by G. Turrell and co-workers.^{35,38,39,43,44} In this approach, all the following conditions are assumed to be satisfied: (i) the wave front surface coming from the laser must be uniphase and of Gaussian type; (ii) the focusing system must be aplanatic; (iii) the sample surface must be perpendicular to the revolution axis of the laser and to the focus optics; (iv) the sample must be homogeneous and optically isotropic (or perfectly oriented); (v) the focal point must be localized at a short distance from the surface.

4.2.1. General Intensity Expressions

In the usual orientation conventions (see the notations recalled in Figure 30), any point P located in the focal plane is initially defined by its polar coordinates, r , β , and ψ . Then, according to the theoretical approaches first developed by Richards and Wolf,⁴⁵ and then by Torök et al.,⁴⁶ it may be demonstrated that the incident electric field of a laser initially polarized along the X direction fits the following expression:

$$E_{\text{inc}} = \begin{pmatrix} i(I_0 + I_2 \cos 2\psi) \\ -(I_2 \sin 2\psi) \\ -2(I_1 \cos \psi) \end{pmatrix} \quad (92)$$

Here, I_0 , I_1 , and I_2 are integrals over the effective angle of illumination (θ_m) and are functions of the longitudinal (u) and transverse (v) dimensionless optical coordinates at the point P , namely

$$u = (2\pi/\lambda_0)z \sin^2 \theta_m$$

and

$$v = (2\pi/\lambda_0)(x^2 + y^2)^{1/2} \sin \theta_m \quad (93)$$

Then, using the definition of

$$m = +\sqrt{(n^2 - \sin^2 \theta_i)} \quad (94)$$

we obtain the expressions

$$I_0(u, v, n) = \int_0^{\theta_m} D(\theta) \sin \theta \left\{ \frac{2m \cos \theta}{n^2 \cos \theta + m} + \frac{2 \cos \theta}{\cos \theta + m} \right\} \times J_0\left(\frac{v \sin \theta}{\sin \theta_m}\right) \exp(iu \cos \theta / \sin^2 \theta_m) \cos^{1/2} \theta \, d\theta \quad (95)$$

$$I_1(u, v, n) = \int_0^{\theta_m} D(\theta) \sin \theta \left[\frac{2 \sin \theta \cos \theta}{n^2 \cos \theta + m} \right] \times J_1\left(\frac{v \sin \theta}{\sin \theta_m}\right) \exp\left(\frac{iu \cos \theta}{\sin^2 \theta_m}\right) \cos^{1/2} \theta \, d\theta \quad (96)$$

$$I_2(u, v, n) = \int_0^{\theta_m} D(\theta) \sin \theta \left\{ \frac{-2m \cos \theta}{n^2 \cos \theta + m} + \frac{2 \cos \theta}{\cos \theta + m} \right\} \times J_2\left(\frac{v \sin \theta}{\sin \theta_m}\right) \exp\left(\frac{iu \cos \theta}{\sin^2 \theta_m}\right) \cos^{1/2} \theta \, d\theta \quad (97)$$

where J_0 , J_1 , and J_2 are Bessel functions of first kind and of zero, first, second order, respectively, and the radial Gaussian distribution of the incident laser energy $D(\theta)$ is defined by

$$D(\theta) = \left(\frac{N}{\sin \theta_m} \right) \exp\left(-\frac{\sin^2 \theta}{\sin^2 \theta_m} \right) \quad (98)$$

Unfortunately, the above integrals cannot be obtained under simple analytic expressions and they are not rapidly converging, so that elaborate numerical calculations (in high precision) must be performed. Nevertheless, according to the general intensity expression in eq 91, the calculations of the Raman intensities are carried out by a double integration (of triple integrands!) over the collection cone of diffusion ($d\Omega$) and, later, over the illuminated volume (dV):

(i) Integration over the scattering cone ($d\Omega$) (see Figure 31). First,

$$\int_{\Omega} (E)_{\text{scat}}^2 \, d\Omega = \int_{\Omega} \begin{pmatrix} (\cos \theta \cos \varphi \sin \chi + \sin \varphi \cos \chi)^2 \\ (-\cos \theta \sin \varphi \sin \chi + \cos \varphi \cos \chi)^2 \\ (\sin \varphi \sin \chi)^2 \end{pmatrix} d\Omega = \begin{pmatrix} A \\ A \\ B \end{pmatrix} \quad (99)$$

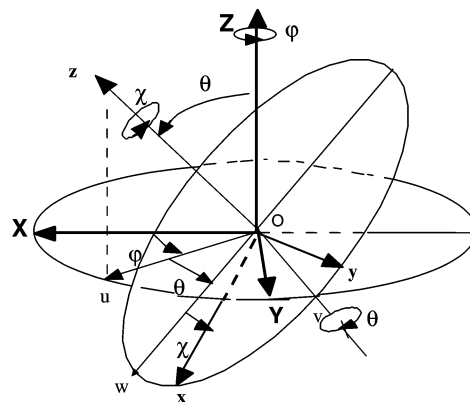


Figure 31. Definitions of the Euler angles in backscattering Raman experiments showing the three rotations φ , θ , χ necessary on passing from the XYZ to the xyz reference axes.

with

$$A = \pi^2 \int_0^{\theta_m} (\cos^2 \theta + 1) \sin \theta \, d\theta = \pi^2 \left(\frac{4}{3} - \cos \theta_m - \frac{1}{3} \cos^3 \theta_m \right) \quad (100)$$

and

$$B = 2\pi^2 \int_0^{\theta_m} \sin^3 \theta \, d\theta = \pi^2 \left(\frac{2}{3} - \cos \theta_m + \frac{1}{3} \cos^3 \theta_m \right) \quad (101)$$

Equation 99 thus transforms into

$$\int_{\Omega} [\alpha_{XYZ}^2] E_{\text{scat}}^2 \, d\Omega = \begin{pmatrix} \alpha_{XX}^2 A + \alpha_{XY}^2 A + \alpha_{XZ}^2 B \\ \alpha_{YX}^2 A + \alpha_{YY}^2 A + \alpha_{YZ}^2 B \\ \alpha_{ZX}^2 A + \alpha_{ZY}^2 A + \alpha_{ZZ}^2 B \end{pmatrix} \quad (102)$$

(ii) Second integration over the volume (dV). In a second step, we define the height ($h = z$) and the radius ($R = (x^2 + y^2)^{1/2}$) of the illumination cone and, then, the total volume V :

$$V = \frac{1}{3} \pi R^2 h = \frac{1}{3} \pi \left(\frac{v^2}{k^2 \sin^2 \theta_m} \right) \left(\frac{u}{k \sin^2 \theta_m} \right) = \frac{1}{3} \pi \frac{uv^2}{k^3 \sin^4 \theta_m} \quad (103)$$

so that

$$dV = \frac{2\pi}{3} \left(\frac{1}{k^3 \sin^4 \theta_m} \right) v \, dv \, du \quad (104)$$

and

$$\int_V dV E_{\text{inc}}^2 \approx \int_0^{2\pi} d\psi \int_{-\infty}^{+\infty} v \, dv \int_0^{\infty} du E_{\text{inc}}^2 = \begin{pmatrix} 2C_0 + C_2 \\ C_2 \\ 4C_1 \end{pmatrix} \quad (105)$$

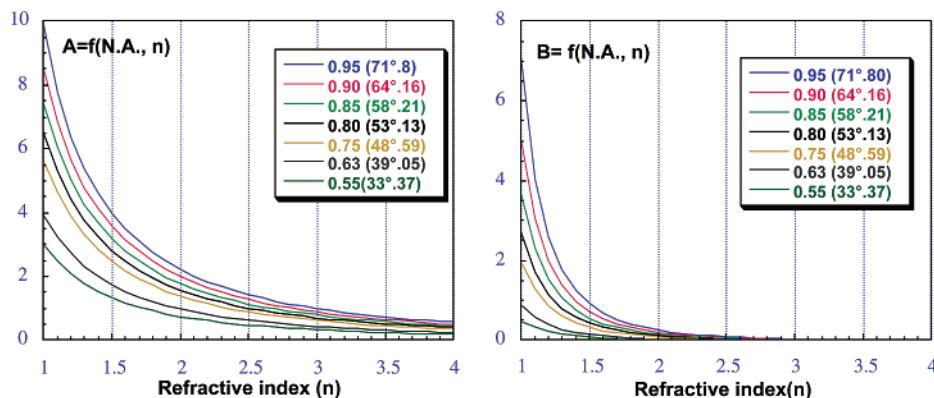


Figure 32. Variations of the A and B coefficients for various objectives versus the refractive index, n .

where the C_j coefficients associated with energy distributions of the incident intensity are

$$C_j = 2\pi \int_0^\infty \int_0^\infty |I_j(u, v, n)|^2 v \, dv \, du \quad (106)$$

(iii) Finally, the complete Raman intensity expression becomes

$$\begin{aligned} \text{int} = & C\{(\alpha_{XX}^2 A + \alpha_{XY}^2 A + \alpha_{XZ}^2 B)(2C_0 + C_2) + \\ & (\alpha_{YX}^2 A + \alpha_{YY}^2 A + \alpha_{YZ}^2 B)(C_2) + \\ & (\alpha_{ZX}^2 A + \alpha_{ZY}^2 A + \alpha_{ZZ}^2 B)(4C_1)\} \quad (107) \end{aligned}$$

where the coefficients A and B are related to the collection of the Raman scattering and are dependent on the “effective” half-aperture angle inside the sample; their variations are plotted in Figure 32 as a function of the refractive index of the sample.

Similarly, the variations of the coefficients C_0 , C_1 , and C_2 related to the energy distributions of the incident intensity at the point $P(r, \beta, \psi)$ in the focal plane inside the sample are reported in Figure 33. It is noteworthy that values of the coefficients C_0 , C_1 , and C_2 vary roughly in the ratios 100/10/1; the intensities are thus mainly dependent on the coefficient C_0 , and their variations are governed by the first terms in eq 107. We may recall that similar variation curves were already published in the literature,^{38,39} but significant differences and more rapid decreases (when the refractive index n increases) are evidenced for the highest NA values, since we have carried out the integral calculations with a higher accuracy and a double precision method.

Finally, it is remarkable that the average energy density at any point of the coordinates (u, v, ψ) takes always the form

$$\langle W_e(u, v, \psi) \rangle \approx (1/8\pi)(C_0 + 2C_1 + C_2) \quad (108)$$

and this expression normalizes (at a constant energy density) the responses of all different objective lenses.

To conclude this theoretical section, we must recall that the intensity and depolarization ratio measurements in Raman microspectrometry are sometimes very tedious and quite complex, even when dealing with a weakly absorbing sample. However, in the following examples, we shall try to demonstrate that very good relevant results can nevertheless be reached,

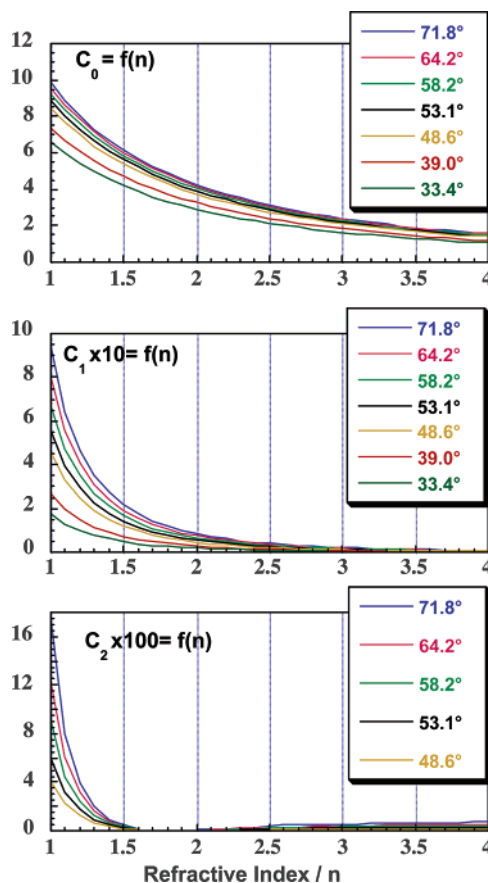


Figure 33. Variations of the intensity coefficients C_0 , C_1 , and C_2 as a function of the refractive index, n .

provided that rigorous attention is paid to the precise experiments and the data treatment.

4.2.2. Application of the Intensity Expression to a Liquid Sample

In agreement with the previously defined geometric scattering definitions (Figure 27), application of the general intensity relation in eq 107 leads to the following development for the measurement of the depolarization ratio of a Raman signal in a nonabsorbing liquid:

$$\begin{aligned} \text{int}_{\parallel} \approx & I_{(XX)} \approx \{(\alpha_{XX}^2 A + \alpha_{XZ}^2 B)(2C_0 + C_2) + \\ & (\alpha_{YX}^2 A + \alpha_{YZ}^2 B)(C_2) + (\alpha_{ZX}^2 A + \alpha_{ZZ}^2 B)(4C_1)\} \quad (109) \end{aligned}$$

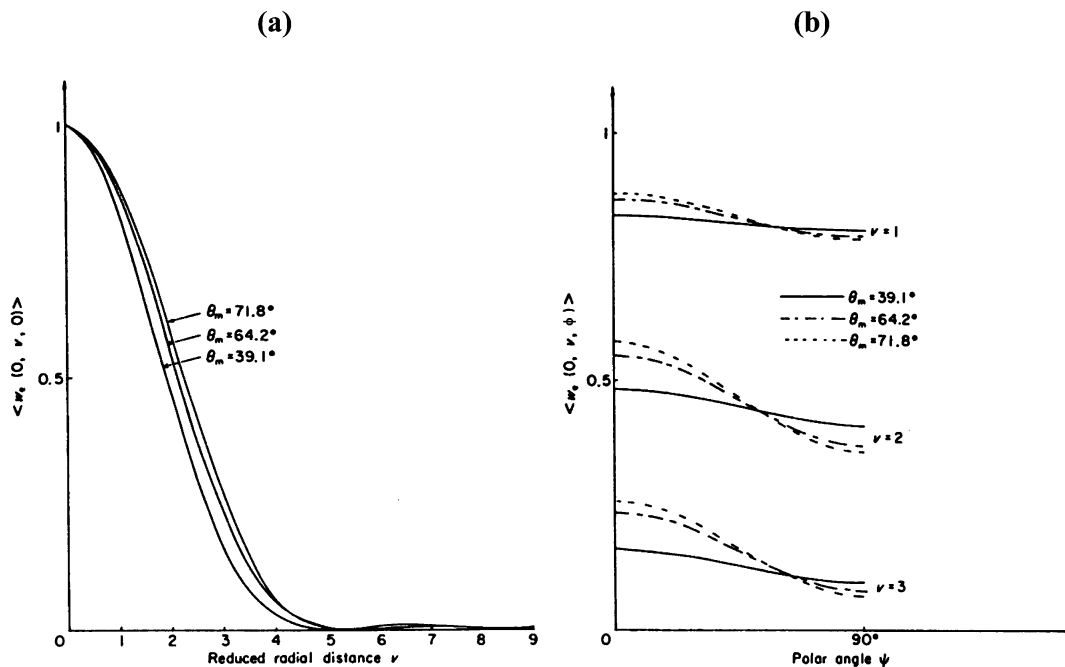


Figure 34. (a) Variations of the normalized energies $\langle W_e(0, \nu, 0) \rangle$ as a function of the “reduced” radial distance with three objectives. (b) Variations of $\langle W_e(0, \nu, \psi) \rangle$ in the focal plane for the “reduced” radial distances $\nu = 1.0, 2.0,$ and $3.0,$ respectively. (Reproduced with permission from ref 44. Copyright 1984 John Wiley & Sons Limited.)

Table 8. Depolarization of the $\nu_1(A_1)$ and $\nu_4(F_2)$ Modes in CCl_4 (Results adapted from Ref 43)

θ_m/deg	$\nu_1(A_1)$ 459 cm^{-1}			$\nu_4(F_2)$ 314 cm^{-1}		
	$\rho_{\text{calc}}(n=1.0)$	$\rho_{\text{calc}}(n=1.46)$	ρ_{exp}	$\rho_{\text{calc}}(n=1.0)$	$\rho_{\text{calc}}(n=1.46)$	ρ_{exp}
71.8	0.03	0.003	0.012 ± 0.005	0.801	0.770	0.770 ± 0.030
64.8	0.02	0.0025	0.010 ± 0.005	0.795	0.767	0.770 ± 0.030
58.2	0.015	0.002	0.008 ± 0.005	0.788	0.765	0.760 ± 0.030
39.1	0.004	0.001	0.008 ± 0.005	0.770	0.758	0.760 ± 0.030
20.5	0.000	0.000	0.007 ± 0.005	0.756	0.753	0.750 ± 0.030

$$\text{int}_\perp \approx I_{(YX)} \approx \{(\alpha_{YX}^2 A + \alpha_{YZ}^2 B)(2C_0 + C_2) + (\alpha_{XX}^2 A + \alpha_{XZ}^2 B)(C_2) + (\alpha_{ZX}^2 A + \alpha_{ZZ}^2 B)(4C_1)\} \quad (110)$$

If we consider the $\nu_1(A_1)$ band at 459 cm^{-1} and the $\nu_4(F_2)$ mode at 314 cm^{-1} of the CCl_4 molecule of spherical symmetry ($n = 1.46$; point group T_d), we obtain for the corresponding theoretical depolarization ratios, $\rho_{\text{calc}} = \text{int}_\perp / \text{int}_\parallel$,

$$\rho_{\text{calc}}(A_1, \alpha_{xx} = \alpha_{yy} = \alpha_{zz}) = \frac{4BC_1 + AC_2}{2AC_0 + 4BC_1 + AC_2} \quad (111)$$

$$\rho_{\text{calc}}(F_2, \alpha_{xx} = \alpha_{yy} = \alpha_{zz} = 0) = \frac{6(A + B)C_0 + 4(3A + 4B)C_1 + (7A + 6B)C_2}{2(4A + 3B)C_0 + 4(3A + 4B)C_1 + (7A + 6B)C_2} \quad (112)$$

Actually, as indicated in Table 8, we observe very good agreement between the experimental and calculated ratios.

4.2.3. Radial and Axial Energy Distributions within the Objective Focal Plane⁴⁴

As mentioned previously, the point $P(r, \beta, \psi)$ located in the focal plane may equivalently be defined by its

dimensionless optical axial (u) and radial (v) coordinates, that is, by $P(u, v, \psi)$, and according to eq 98, the Gaussian distribution of the incident energy has the analytic form

$$D(\theta) = \langle W_e(\sin \theta) \rangle = \left(\frac{N}{\sin \theta_m} \right) \exp\left(- \frac{\sin^2 \theta}{\sin^2 \theta_m} \right)$$

So, it is important to determine the variations in the distribution and the mean value of the electric energy along the radial and axial directions when the aperture of the objective lens is modified.⁴⁴

4.2.3.1. Radial Distribution. The curves of the average energies $\langle W_e(0, \nu, 0) \rangle$ and $\langle W_e(0, \nu = \text{constant}, \psi) \rangle$ are compared for three objectives in Figure 34. They display a very similar Gaussian shape, with a half-width at half-height, $\nu_{1/2} \cong 2.0 \pm 0.2$. We thus retrieve already known values of the radial resolving power,

$$y = 2(x^2 + y^2)^{1/2} = \frac{2\nu_{1/2}}{|k| \sin \theta_m} = \frac{\lambda_0 \nu_{1/2}}{\pi \sin \theta_m} \cong 0.64 \frac{\lambda_0}{\text{NA}} \quad (113)$$

and the resolution does not vary significantly, as we are always working at the limits imposed by the diffraction. Note that the effective radius of the spot (y) is equal to $0.492 \mu\text{m}$ (X100 lens) or to $0.575 \mu\text{m}$ (50X lens), when using the red He–Ne laser line

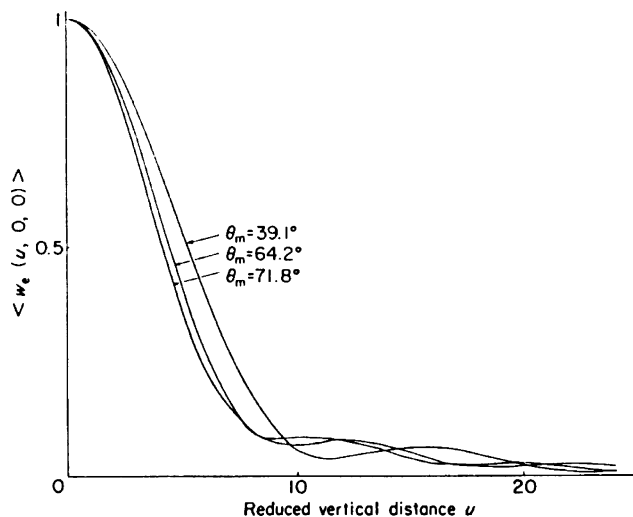


Figure 35. Variations of the normalized average incident electric energies $\langle W_e(u, 0, 0) \rangle$ as a function of the “reduced” vertical distance for three distinct objectives. (Reproduced with permission from ref 44. Copyright 1984 John Wiley & Sons Limited.)

Table 9. Values of the “Effective” Axial Depth Using the 100X and UTK 50X Lenses ($\lambda_0 = 632.8$ nm)

objective	θ_m/deg	NA	$u_{1/2}$	$\delta/\mu\text{m}$	$2\delta/\mu\text{m}$ (dof)
100X	64.2	0.90	4.5	1.12	2.24
UTK 50X	39	0.63	5.5	2.78	5.57

(632.8 nm). These values are in very good agreement with those already reported in Table 5.

4.2.3.2. Axial Distribution. In this case, as shown in Figure 35, the curves of the normalized average energy axial distributions $\langle W_e(u, 0, 0) \rangle$ display significant variations and are dependent on the NA of the objective lens. Their half-width at half-maximum $u_{1/2}$ varies over the 4.5–5.5 range. This result prompts us to define an effective axial depth (δ) or “depth of focus” (dof, 2δ), whose values for the two 100X and UTK 50X lenses are given in Table 9:

$$\delta = 2Z = \frac{2u_{1/2}}{|k| \sin^2 \theta_m} = \frac{\lambda_0 u_{1/2}}{\pi \sin^2 \theta_m} \quad (114)$$

The depth of focus varies drastically from one lens to another (here, by the factor 2.5), as the illuminated volume is inversely proportional to NA^2 (or, equivalently, to $\sin^2 \theta_m$). As indicated in Table 9, we thus obtain an estimate of the depth of focus (2δ) value at 50% of irradiance.

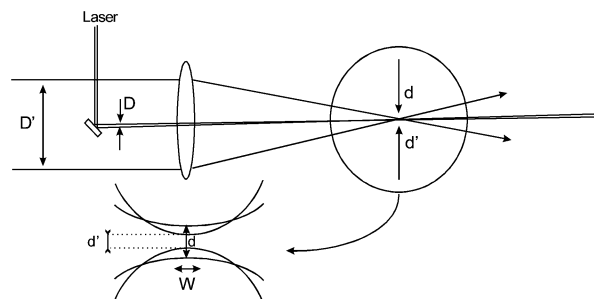
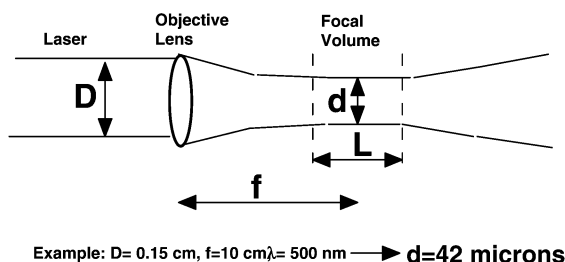


Figure 36. Diameters (d and d') and useful lengths (L and W) of the “waist” laser in a confocal microscopic setup. Note that $d = 4\lambda_0/f\pi D$ and $L = 16\lambda_0 f^2/\pi D^2 = \pi d^2/\lambda_0$.

In conclusion, it is clear that all these very important optical properties must be taken into consideration for a proper recording of polarized Raman spectra. In particular, in the above diagrams we have shown that severe conditions must be fulfilled to probe radially and/or axially (in the depth) any new nonabsorbing sample by using the micro-Raman spectroscopic technique.

4.3. Optical Principles and in-Depth Sectioning with a Confocal Instrument

In the preceding section we have shown that Raman microspectrometry is a very efficient technique to investigate small samples and restricted volumes (a few cubic micrometers or picograms), such as a small gas inclusion inside a transparent material, for instance. Now, considering the advantages of the confocal microscopic technique, we shall demonstrate that both the radial (lateral) and axial (in depth) resolutions can even be improved when working at the spatial micronic limits imposed by the diffraction.

Actually, because of the peculiar shape of the “waist” of any laser beam tightly focused in the object focal plane of the microscope, the main goal for any sample under study is to collect the Raman light passing through an adjustable aperture. This pinhole is located in the corresponding image confocal plane. As sketched in Figures 36 and 37, the challenge is thus to adjust a Raman microscope with the smallest dimension, $d = d'$ minimum. Under these conditions, it is necessary to insert a first fixed diaphragm on the entrance beam path (to diminish d') and to put another adjustable confocal hole on the outgoing beam. Then, only the photons coming from the focal plane, where the incident intensity is maximum, are efficient: both diaphragms or pinholes are said to be confocal; in other words, they must be optically conjugated to the point source in the object plane, and only the light coming from the focal plane is entirely collected by the detector.

Normally, such an optical setup must allow us to select different zones or in-depth sections in a weakly absorbing sample by adjusting the size of the confocal pinhole placed before the spectrometer. One must be able to spectroscopically perform a true axial sectioning at a variable depth of penetration.

Actually, the optimum axial resolution is theoretically reached if the size of the confocal diaphragm is equal to that of the image (given by the objective) of

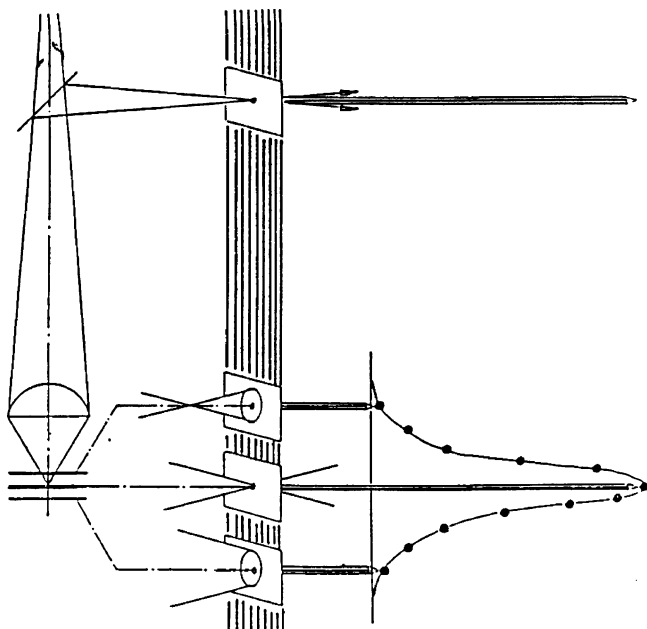


Figure 37. Confocal configuration and principle of the optical sectioning along the axial direction. (Reproduced with permission from ref 48. Copyright 1990 Jobin-Yvon SAS.)

the laser point source in the sample, provided there are no aberration or diffuse reflection effects.⁴⁷ This confocal configuration is thus quite convenient in Raman microspectrometry, as it normally allows the rejection of any stray light (background, fluorescence, luminescence, ...) coming from outside the probed focal volume. As an illustrative example, we compare in Figure 38 two spectra recorded with the classic and the confocal Raman technique, respectively; identical conditions were used (laser 2 mW at $\lambda_0 = 514.5$ nm, CCD detector) to irradiate graded polystyrene balls (average diameter of $0.5 \mu\text{m}$) lying on a glass plate.⁴⁸ The first spectrum (left) has been obtained using wide slits (confocal hole opened up to

$1200 \mu\text{m}$ diameter), meanwhile for the recording of the second spectrum (right) the confocal pinhole has been intentionally closed down to $140 \mu\text{m}$. This condition corresponds to an analyzed sample of diameter equal to $\approx 1.0 \mu\text{m}$, considering the magnification of the 100X objective and the 1.4 amplification factor of the instrument transfer optics.⁴⁷ It is noteworthy that both spectra are displayed on the same scale; they have not been the subject of any particular treatment, and the drastic decrease of the background in the second case is surely due to the restricted depth of focus. Definitely, there is no intensity loss in the Raman bands due to polystyrene and the contrast is markedly improved.

It is otherwise possible to demonstrate that the performances in axial sectioning of a confocal Raman microspectrometer can be derived, in a first approximation, from simple rules of optical geometry.^{48,49} In addition, thanks to the use of different objectives and pinholes, this technique facilitates the investigation of multilayered composite thick polymer films. Nevertheless, it will often be difficult to eliminate any aberration phenomena and refraction effects without a loss of the in-depth resolution. So, all these factors must be considered in a more rigorous approach before drawing definitive conclusions (qualitative or quantitative) on the nature of the probed interfaces. In recent studies, some conclusions were sometimes too hurriedly claimed. So, one must remember that this problem is very difficult to treat rigorously and remains an open question. It is still the matter of numerous debates and discussions in the recent literature.^{47,50-55}

4.4. Applications, Raman Images, and Calculation of the Order Parameters

4.4.1. Uniaxial Orientation in Azopolymer Diffraction Gratings

It has been recently demonstrated in several groups and research laboratories that permanent

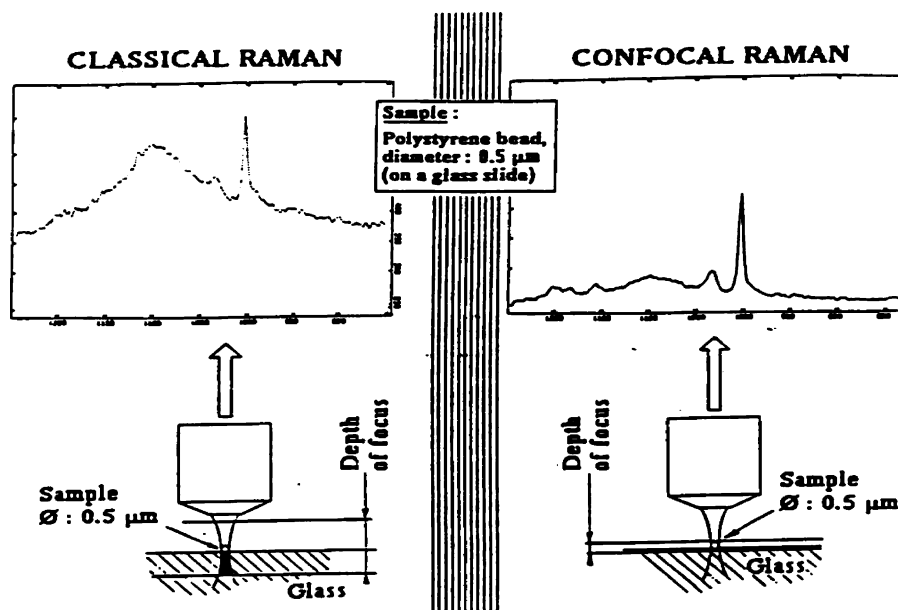


Figure 38. Spectra of polystyrene balls ($\phi = 0.5 \mu\text{m}$) lying on a glass plate: (left) under classic conditions; (right) under confocal Raman conditions. (Reproduced with permission from ref 48. Copyright 1990 Jobin-Yvon SAS.)

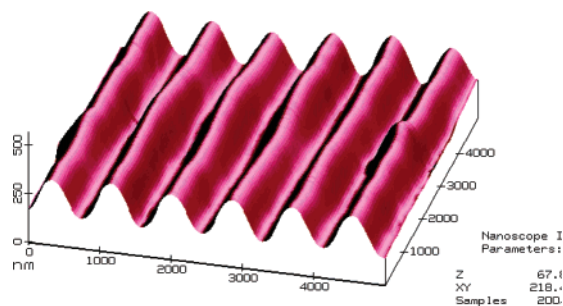


Figure 39. Atomic force microscopy (AFM) image of a 830 nm period grating with a surface relief modulation of 190 nm.

holographic gratings, with a spatial period (Λ) typically in the 0.8–3.0 μm range (Figure 39), can be easily inscribed on initially isotropic thin films (1–2 μm) of amorphous polyacrylate (co-)polymers (pDR1M-co-MMA) containing covalently bonded “azobenzene units” in side-chain positions.

Such holographic gratings are optically inscribed by interfering two coherent laser beams with appropriate polarizations, for instance using the circular polarizations (circR + circL), the parallel linear ones (p + p, s + s), and/or the orthogonal linear ones (p + s). The relief amplitudes and dynamics of formation are strongly dependent on the used polarizations.^{18,56–63} Actually, from the analyses of the intensities and polarizations of all the transmitted and diffracted beams at several orders (0, ± 1 , ± 2), two main contributions in the formation mechanisms have been clearly distinguished and characterized: on one hand, the anisotropy or birefringence (Δn) and, on the other hand, the sinusoidal modulation of the surface relief (Δd).

To get new information on these mechanisms and on the chromophore orientations, we have recorded for the first time, with the help of confocal Raman microspectrometry, different series of polarized Raman spectra in all regions of such surface gratings. The spectra were largely enhanced because of resonance Raman effects. Therefore, from inspection of the intensity variations of some characteristic vibrational modes, we have obtained polarized Raman images of large surfaces (16 \times 16 μm^2 , for instance). These images reproduced quite confidently the grating grooves, as we shall see hereafter. Then, from theoretical treatments of the scattered Raman intensities including the objective lens corrections, we were able to estimate both order parameters ($\langle P_2 \rangle$ and $\langle P_4 \rangle$), to obtain new information about the chromophore orientation distribution functions, $F(\cos \theta)$, and the dye concentration gradients (at a submicron level). Results of some selected examples are summarized in the following sections, compared to the topographic images recorded by AFM (atomic force microscopy) and to the theoretical predictions of the “angular hole-burning” photo-orientation model in order to validate this new Raman approach.

4.4.1.1. Diffraction Gratings Inscribed Using (circ.Right + circ.Left) Polarizations. The first example concerns the study of diffraction gratings inscribed by interfering two coherent laser beams of circular polarizations, Right (R) and Left (L). This

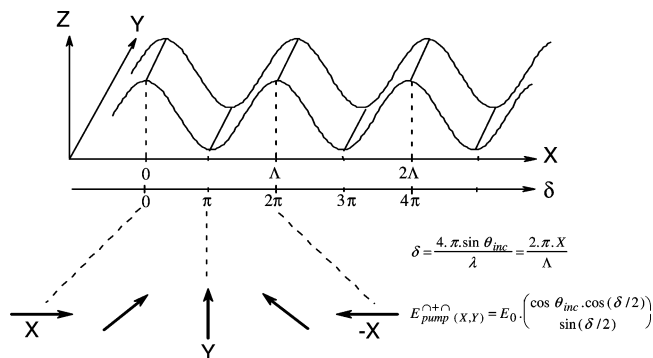


Figure 40. Variations of the polarization direction and of the electric components along the X and Y axes for the incident configuration (circ.Right + circ.Left) as a function of the position δ along the grating vector direction. (Reprinted with permission from ref 18. Copyright 1998 American Chemical Society.)

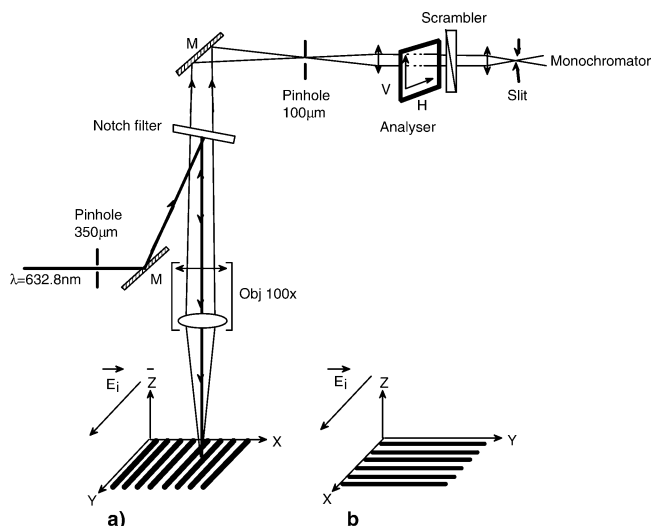


Figure 41. Experimental setup in Raman confocal microscopy for the recording of polarized spectra: (a) recording of $Z(YX)Z$, $Z(Y)Z$ spectra in the first configuration; (b) recording of $Z(XY)Z$, $Z(X)Z$ spectra in the second configuration. (Reprinted with permission from ref 18. Copyright 1998 American Chemical Society.)

process involves a modulated orientation of the polarization, which remains linear but accomplishes a 2π rotation along a grating period, Λ (see chart in Figure 40).

From an experimental point of view and according to the Porto notation, two series of two polarized Raman spectra, $Z(YX)Z$, $Z(Y)Z$ in the first experiments and $Z(XY)Z$, $Z(X)Z$ in the second ones, were recorded with a data point at every ~ 0.5 or $0.2 \mu\text{m}$. Several lines covering a large area (roughly $20 \times 20 \mu\text{m}^2$) were inspected in order to get a reasonable average over several grating periods. Details about the experimental confocal microscopic setup are described in Figure 41. It is noteworthy that we intentionally fixed the direction of the incident electric field \mathbf{E}_i , while the analyzer was adjusted in either the V or H position, successively (a/setup); then, the sample stage was rotated by 90° to record the second series of polarized spectra (b/setup).

Under these conditions, according to the reference axes defined in Figure 41 and to the general Raman intensity from eq 91,

$$I_{IJ}^{\text{Raman}} \approx \int_V \int_{\Omega} |\mathbf{E}_i \langle \alpha_{IJ} \rangle \mathbf{E}_s|^2 d\Omega dV$$

we expect the following polarized Raman responses:

For the incident laser beam polarized along the
Y direction,

$$\begin{aligned} I_{(YX)} &= [\langle \alpha_{YX}^2 \rangle A + \langle \alpha_{YZ}^2 \rangle B] (2C_0 + C_2) + \\ &[\langle \alpha_{ZX}^2 \rangle A + \langle \alpha_{ZZ}^2 \rangle B] (4C_1) + [\langle \alpha_{XX}^2 \rangle A + \langle \alpha_{XZ}^2 \rangle B] (C_2) \\ I_{(YY)} &= [\langle \alpha_{YY}^2 \rangle A + \langle \alpha_{YZ}^2 \rangle B] (2C_0 + C_2) + \\ &[\langle \alpha_{ZY}^2 \rangle A + \langle \alpha_{ZZ}^2 \rangle B] (4C_1) + [\langle \alpha_{XY}^2 \rangle A + \langle \alpha_{XZ}^2 \rangle B] (C_2) \end{aligned} \quad (115)$$

leading to the first ratio of relative Raman intensities,

$$R_1(X \text{ or } \delta) = \frac{I_{YX}}{I_{YY}} \quad (116)$$

For the incident laser beam polarized along the
X direction,

$$\begin{aligned} I_{(XY)} &= [\langle \alpha_{XY}^2 \rangle A + \langle \alpha_{XZ}^2 \rangle B] (2C_0 + C_2) + \\ &[\langle \alpha_{ZY}^2 \rangle A + \langle \alpha_{ZZ}^2 \rangle B] (4C_1) + [\langle \alpha_{YY}^2 \rangle A + \langle \alpha_{YZ}^2 \rangle B] (C_2) \\ I_{(XX)} &= [\langle \alpha_{XX}^2 \rangle A + \langle \alpha_{XZ}^2 \rangle B] (2C_0 + C_2) + \\ &[\langle \alpha_{ZX}^2 \rangle A + \langle \alpha_{ZZ}^2 \rangle B] (4C_1) + [\langle \alpha_{YX}^2 \rangle A + \langle \alpha_{YZ}^2 \rangle B] (C_2) \end{aligned} \quad (117)$$

leading to the second ratio of relative intensities,

$$R_2(X \text{ or } \delta) = \frac{I_{XY}}{I_{XX}} \quad (118)$$

We must recall that not only the terms $\langle \alpha_{IJ}^2 \rangle$ in the above expressions are estimated from orientationally averaged quantities but one must also consider an additional matrix rotation, $\mathbf{R}(\beta')$, of the polarization vector,

$$\langle \alpha_{IJ}^2 \rangle \approx \langle [\mathbf{R}(\beta') [\mathbf{T}(\theta, \varphi, \psi) \xrightarrow{\alpha} \mathbf{T}^t(\theta, \varphi, \psi)] \mathbf{R}^t(\beta')]^2 \rangle \quad (119)$$

where the values $\beta' = 0^\circ, 45^\circ,$ and 90° correspond to points localized at the top, at the half-slope, and in the bottom positions of the surface relief, respectively. Similarly, the two ratios R_1 and R_2 are dependent on the positions X (or δ) over a grating period (see definition in Figure 40) and on the orientationally averaged quantities $\langle \cos^2 \theta \rangle$ and $\langle \cos^4 \theta \rangle$, that is, on the two first even-order Legendre polynomials, $\langle P_2 \rangle$ and $\langle P_4 \rangle$.^{18,19}

As an illustration, four polarized Raman spectra, $Z(YY)\bar{Z}$, $Z(YX)\bar{Z}$ on one hand and $Z(XX)\bar{Z}$, $Z(XY)\bar{Z}$ on the other hand, recorded over the 1000–1700 cm^{-1} wavenumber range for a 3.0 μm period grating are reproduced in Figure 42. The intensity variations of the mode $\nu_s(\text{NO}_2)$ at 1339 cm^{-1} (with data points at every 0.2 μm covering roughly two periods) give rise to the profiles shown in Figure 43. Here, it is very important to point out that the two former responses

are in phase, while the two latter ones are nearly out of phase. These results are in good agreement with the theoretical predictions of a simple hole-burning model,^{18,19,56–59} confirming that the preliminary photophysical orientation mechanisms during the isomerization cycles are quite dominant. The above results concerning both $Z(XX)\bar{Z}$ and $Z(XY)\bar{Z}$ spectra are also elegantly illustrated in the integrated intensity Raman images for a $16 \times 20 \mu\text{m}^2$ area of the surface relief (Figure 44); these images reproduce nicely the grating spacing period and confirm the overall dephasing observed between the two types of polarized Raman response.

From all these experimental results, it is thus possible to establish the variations of the two ratios R_1 , R_2 and, consequently, to estimate the values of the order parameters $\langle P_2 \rangle$ and $\langle P_4 \rangle$ in each region of the surface relief, in particular at the hole and peak locations. Results obtained at these positions are reproduced in Figure 45, where we have also reported the shapes of the most probable orientation distribution functions; these functions were calculated from an estimate of the Lagrange multipliers (λ_2, λ_4) and using the formalism of the “information entropy” theory.²⁵

It is evidenced that the orientation functions display intense maxima at $\pm 90^\circ$ for the hole positions, while they are markedly broader, asymmetric, and split into two maxima at nearly $\pm 30^\circ$ (with respect to the perpendicular direction) for the peak positions. This result is in agreement with the existence of constraints and pressure gradients responsible for the formation of the sinusoidal relief. These constraints probably occur during the mass transport from the holes toward the bumps. Indeed, this interpretation is reinforced by a careful inspection in the four polarized spectra of the variations of the Raman intensities, which were found to be in agreement with an increase of $\sim 5\%$ in the chromophore concentration at the bumps. It is worth noting that these results are consistent with other models independently proposed, in particular the model of a translational dynamics of the polymer chains and that of a viscoelastic flux regime during the grating formation.^{64–66}

4.4.1.2. Diffraction Gratings Inscribed Using Linearly Polarized Beams, ($45^\circ + 135^\circ$) and ($\mathbf{p} + \mathbf{p}$). In a second example, we shall discuss Raman results for holographic gratings inscribed on thin films of the copolymer K1-10 from Bayer AG (Leverkusen, Germany); its chemical formula is reported in the chart in Figure 46. This copolymer contains 10% photoactive “azo” units and 90% “mesogen-azo” units, both in side-chain positions; this facilitates the formation of an intermediate mesophase and the appearance of a strong birefringence ($\Delta n \approx -0.10, -0.25$) because of cooperative orientational effects.^{58,59,67–69} We have inscribed gratings on isotropic thin films of this sample by using two linearly polarized interfering laser beams, more precisely under the ($45^\circ + 135^\circ$) and the ($0^\circ(\mathbf{p}) + 0^\circ(\mathbf{p})$) configurations. In the former case, there exists only a modulation of the final polarization, which is successively linear (vertical or s), elliptic, circular (R

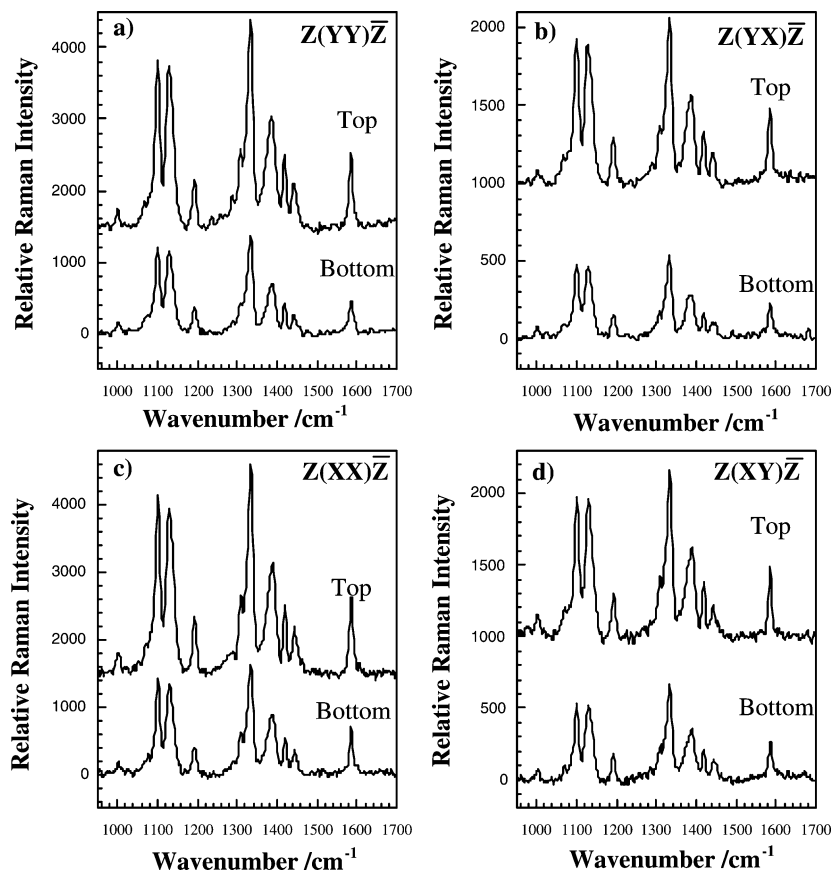


Figure 42. Four polarized Raman spectra recorded under (a) $Z(Y\bar{Y})\bar{Z}$, (b) $Z(YX)\bar{Z}$, (c) $Z(XX)\bar{Z}$, and (d) $Z(XY)\bar{Z}$ polarization conditions for a $3.0\ \mu\text{m}$ period grating. (Reprinted with permission from ref 18. Copyright 1998 American Chemical Society.)

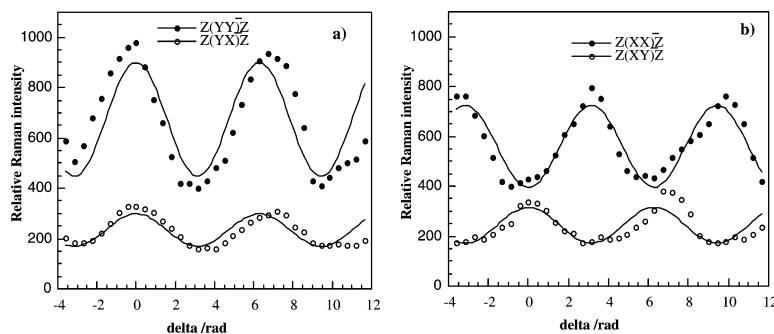


Figure 43. Polarized Raman intensity variations over several grating periods for the mode $\nu_s(\text{NO}_2)$ at $1339\ \text{cm}^{-1}$ under (a) the $Z(Y\bar{Y})\bar{Z}$ and $Z(YX)\bar{Z}$ polarizations and (b) the $Z(XX)\bar{Z}$ and $Z(XY)\bar{Z}$ conditions. (Reprinted with permission from ref 18. Copyright 1998 American Chemical Society.)

or L), elliptic, linear (horizontal or p), ...; in the latter case, the polarization does not vary and remains, of course, horizontal (p), but there is a strong intensity modulation maximizing at X equal to 0.0 , Λ (or equivalently at $\delta = 0, 2\pi$), exactly at the bottom positions of the surface relief (see Figure 46).

In the related micro-Raman studies, our main purpose was to check the chromophore orientations in a direction perpendicular to the incident field. In the first case, the orientational effects were expected to occur alternately at every half-period (with however no preferential orientation at $1/4$ and $3/4$ of a period where the pump polarization is circular), and in the second case, the orientations were expected to give rise to a homogeneous pattern. Nevertheless, as evidenced in Figure 47, peculiar perturbations in the surface relief profiles were revealed from AFM topo-

graphic measurements. In addition to the main modulation with the normal period equal to $3.5\ \mu\text{m}$, submaxima or subminima were always detected at the half-period positions. In the second case, the overstructures were particularly enhanced, giving rise to another $\approx 20\ \mu\text{m}$ height modulation, a perturbation quite significant as compared to the total amplitude of about $55\ \mu\text{m}$.

Several important results of our micro-Raman scattering investigations are summarized in Figures 48 and 49, which contain the curves of the polarized Raman intensity variations over several grating periods and the corresponding variations of the intensity ratios R_1 , R_2 . Also included are the shapes of the orientation distribution functions calculated from the values of the $\langle P_2 \rangle$ and $\langle P_4 \rangle$ parameters determined in different regions.

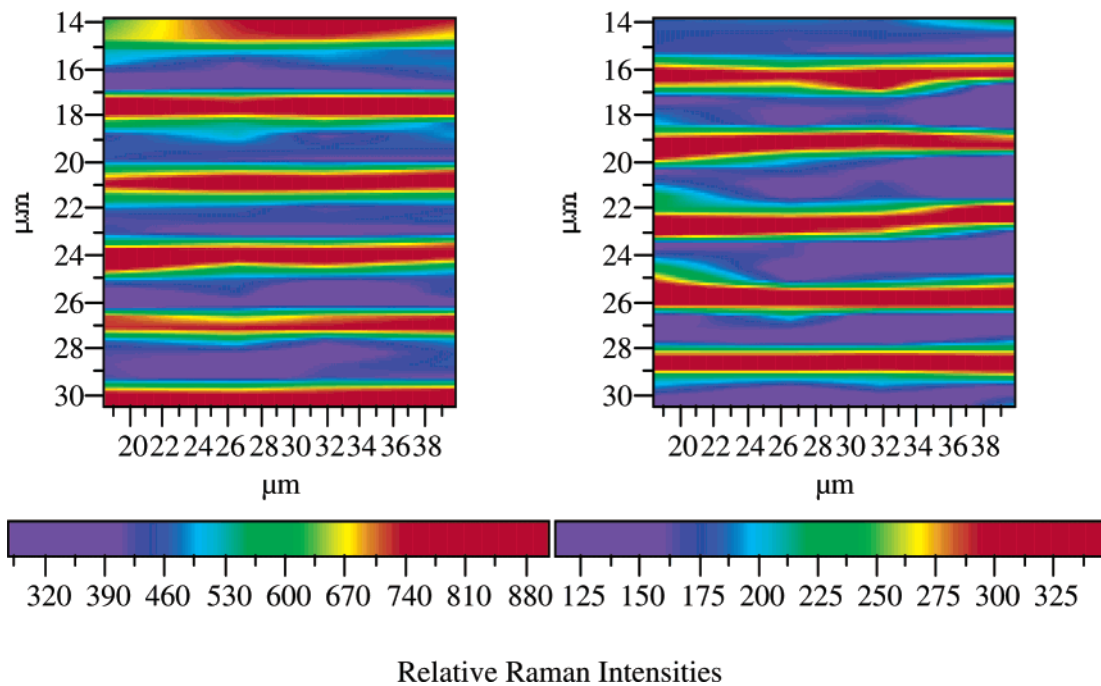


Figure 44. Raman images from the integrated intensities on the $Z(XX)\bar{Z}$ (left) and $Z(XY)\bar{Z}$ (right) spectra. (Reprinted with permission from ref 18. Copyright 1998 American Chemical Society.)

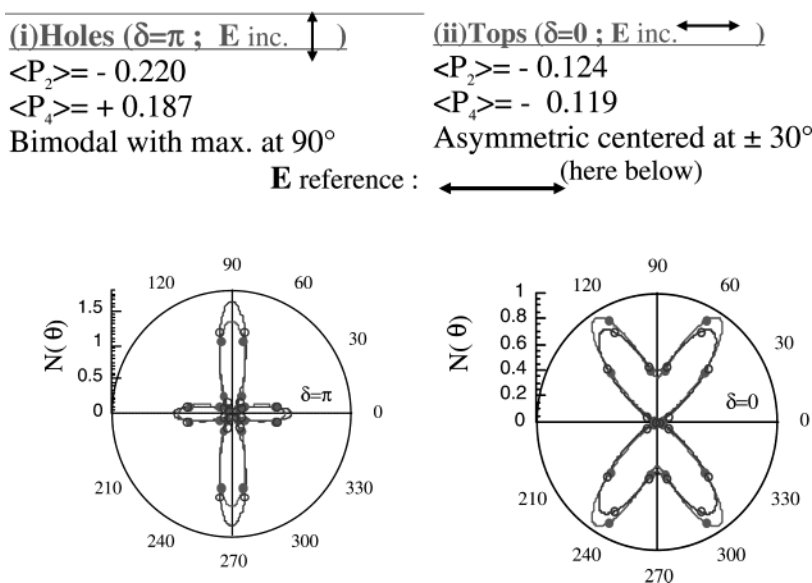


Figure 45. Values of the main order parameters and most probable orientation functions at the hole and top positions of a surface relief grating. (Adapted from refs 18 and 19.)

(i) For the grating inscribed under the $(45^\circ + 135^\circ)$ configuration, we note in the bottom regions $\langle P_2 \rangle = -0.190$ ($\lambda_2 = -1.092$) and $\langle P_4 \rangle = +0.049$ ($\lambda_4 = 0.252$), leading to a Gaussian distribution with a maximum at 90° . Similarly, in the peak regions, the values $\langle P_2 \rangle = -0.200$ ($\lambda_2 = -0.990$) and $\langle P_4 \rangle = +0.149$ ($\lambda_4 = 1.428$) lead to a bimodal distribution maximizing at 0° , as expected. Finally, at the positions $1/4$ or $3/4$ of a period, we do retrieve $\langle P_2 \rangle \equiv \langle P_4 \rangle \approx 0.0$, confirming that the chromophore orientation remains isotropic. All these results thus corroborate the good fit between the developed theoretical and experimental approaches.

(ii) For the grating inscribed under the $(p + p)$ configuration, as expected, we find in each region a chromophore orientation distribution function of

Gaussian type with a maximum at 90° ; all the parameter order values are quite similar, equal to $\langle P_2 \rangle = -0.143$ ($\lambda_2 = -0.984$), $\langle P_4 \rangle = -0.025$ ($\lambda_4 = -0.531$) in the more pronounced holes and equal to $\langle P_2 \rangle = -0.123$ ($\lambda_2 = -0.703$), $\langle P_4 \rangle = +0.005$ ($\lambda_4 = -0.074$) in the weaker bottoms arising from the overmodulations. Therefore, in this study we got a better insight into the grating formation mechanisms, and we have concluded that the surface relief anomalies originate in constructive interferences between transmitted and diffracted beams of a proper polarization.⁵⁸⁻⁶² Furthermore, it is worth noting that the $Z(YY)\bar{Z}$ and $Z(YX)\bar{Z}$ experimental Raman intensity variations have always provided clear evidences for the existence of these overmodulations (Figure 49). Such results demonstrate again the high sensitivity

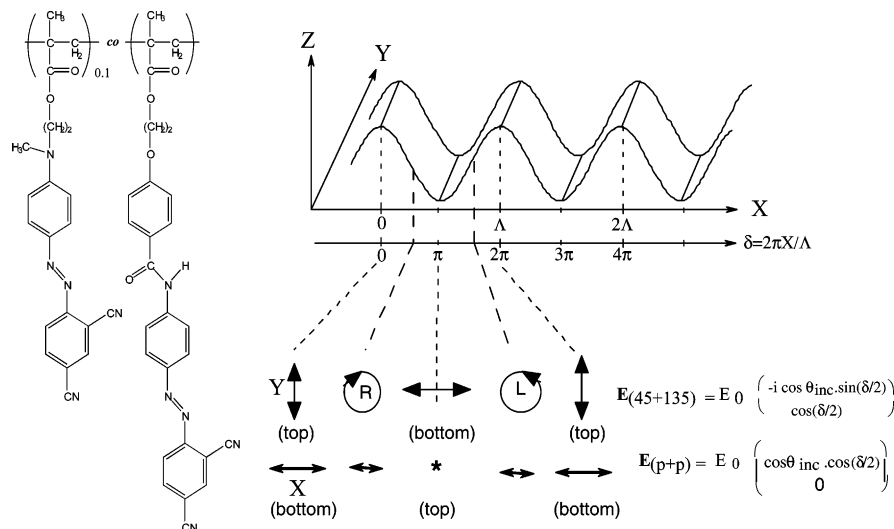
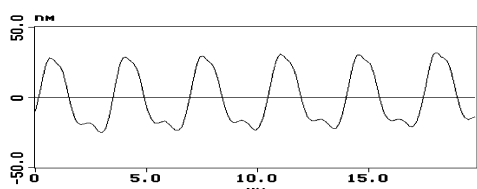


Figure 46. Chemical formula of the K1-10 copolymer and nature of the electric field components in the two linear polarization setups, ($45^\circ + 135^\circ$) and ($p + p$), for holographic grating inscriptions.

a/ ($45^\circ + 135^\circ$) polarizations.



b/ ($p + p$) polarizations.

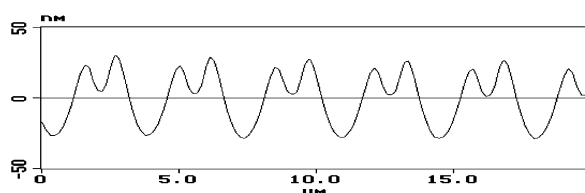
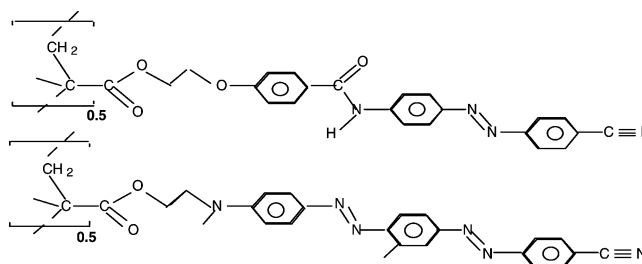


Figure 47. AFM profiles of the perturbed surface reliefs observed in the gratings inscribed under (a) ($45^\circ + 135^\circ$) and (b) ($p + p$) polarizations on K1-10 polymer thin films. (Reproduced with permission of the PCCP Owner Societies from ref 58. Copyright 2000 The Royal Society of Chemistry.)

of the Raman microspectrometric technique used in conjunction with polarization analyses; the corresponding Raman images recorded on large grating areas also revealed themselves to be quite informative.⁵⁸

Furthermore, it is noteworthy that we have similarly applied with success the micro-Raman spectroscopic technique for the determination of the molecular orientations in different azopolymer films. Some parallel studies were developed with the aims to duplicate gratings through a phase mask and to find out the best conditions to stabilize the diffraction efficiency in a new grating inscribed using a single laser beam. We have also investigated the optical properties of gratings poled under high DC electric field conditions, to better understand the polarity effects in the breaking symmetry mechanisms and in the frequency doubling generations.⁷⁰ Finally, from Raman investigations on shorter spacing period gratings ($\Lambda \approx 1.0\text{--}1.4 \mu\text{m}$), we have still obtained nicely resolved Raman images which clearly demonstrate that it is possible to work at the diffraction

Chart 3. Chemical Formula of the Copolymer "P269" (Ref 73)



limits ($\approx \lambda/2$). It is thus obvious that, in the near future, the micro-Raman polarization technique will also be applied with success to other original investigations of various nanomaterials; this technique will surely be useful to develop new applications in the domain of nanophotonics.

4.4.2. Photoinduced Biaxial Orientations in Strongly Absorbing Polymer Films

Hereafter, our purpose is to pay attention to the more complex biaxial symmetry properties of various polymer systems. Such biaxial orientational phenomena occur often in polymer films, because of the occurrence of strong cooperative effects upon photoinduced reactions and/or the existence of either a stable intermediate liquid-crystalline mesophase (as demonstrated in the previously mentioned K1-X type samples^{67–69}) or a semicrystalline phase (as encountered in the p(DR19T) homopolymer⁷¹). For instance, the K1-X polymers are known to be strongly absorbing in the visible region and to possess a very large birefringence, typically in the $\Delta n = -0.2, -0.4$ range.

In this context, we have recently investigated the chromophore orientation properties in thin films of a new "P269" copolymer (see Chart 3) using the UV-visible, Fourier transform infrared (FTIR), and confocal Raman microspectrometric techniques. This copolymer, synthesized in Bayer AG laboratories (Leverkusen, Germany), contained in side-chain positions equal amounts (50%) of two kinds of covalently

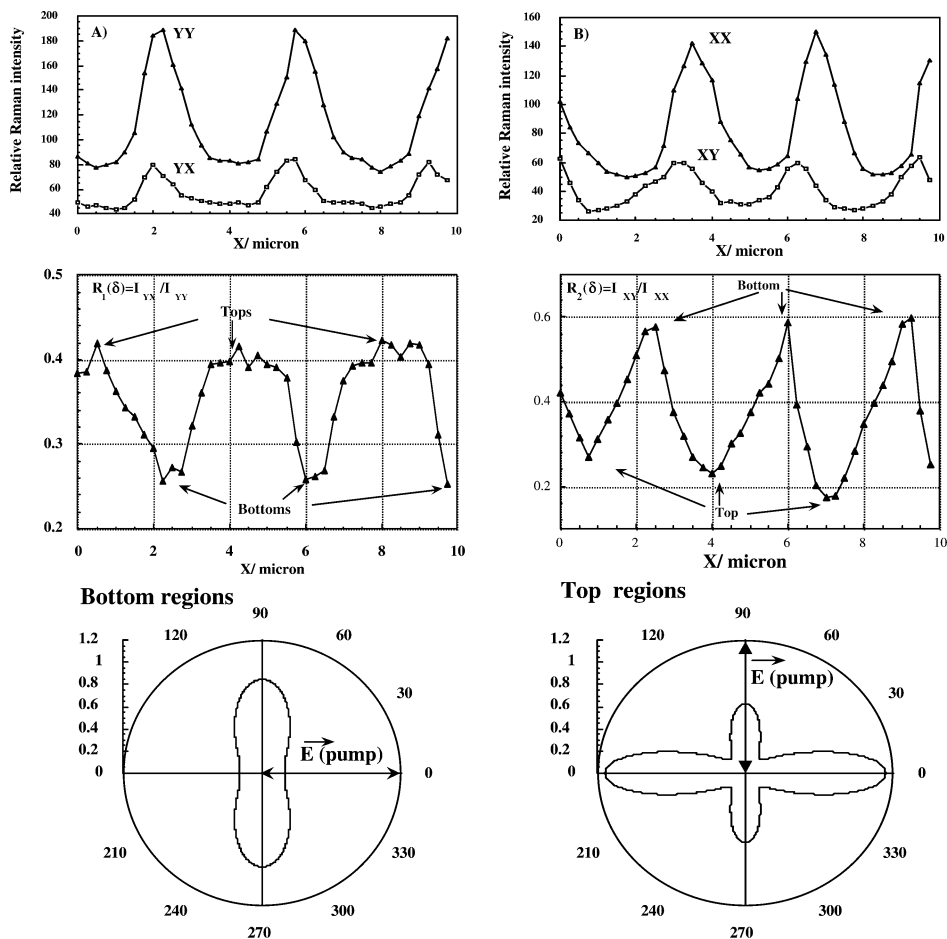


Figure 48. Main Raman results and shapes of the orientation distribution functions in a grating inscribed using the linear polarization ($45^\circ + 135^\circ$) configuration. (Adapted from ref 58.)

bonded azo units, “classic-diazo” and “azo-mesogen” ones.⁷² Most spectroscopic results of this study were recently published,⁷³ so we shall describe only the theoretical basis of the proposed new vibrational approach. For such a biaxial symmetry system, the method consists essentially in combining FTIR and Raman data to get the physically meaningful best fit values of the effective main orientation order parameters.

First, we recall some theoretical background about the definition of the orientational coefficients and the related experimental measurements. Then, the treatments of the vibrational data are discussed and the more physically reasonable orientation distribution functions are developed.

According to Kaito notation¹⁶ and the laboratory axes defined in Figure 50, from FTIR experiments it is possible to obtain the two orientation coefficients f_θ and f_φ . They are estimated from a comparison of the spectrum of the starting isotropic sample (A_0) and those of the sample after irradiation with a linearly polarized laser beam, $A_{||}$ (A_X) and A_{\perp} (A_Y).

Indeed, from the definitions,

$$f_\theta = \frac{1}{2}(3\langle \cos^2 \theta \rangle - 1) \equiv \langle F_{200} \rangle$$

$$f_\varphi = \frac{\langle \cos 2\varphi \sin^2 \theta \rangle}{\langle \sin^2 \theta \rangle} \quad (120)$$

we get straightforwardly the relations

$$A_X \approx \langle \cos^2 \theta \rangle = A_0(2f_\theta + 1)$$

$$A_Y \approx \langle \cos^2 \varphi \sin^2 \theta \rangle = A_0(1 - f_\theta)(1 + f_\varphi)$$

$$A_Z \approx \langle \sin^2 \varphi \sin^2 \theta \rangle = A_0(1 - f_\theta)(1 - f_\varphi) \quad (121)$$

where $A_0 = (A_X + A_Y + A_Z)/3.0$ is the mean absorbance. We thus obtain two important expressions:

$$f_\theta(\text{biax}) = \frac{(A_X/A_0) - 1}{2} = \frac{A_X - \left(\frac{A_Y + A_Z}{2}\right)}{3A_0}$$

$$\text{and } f_\varphi(\text{biax}) = \frac{(A_Y - A_Z)}{(A_Y + A_Z)} \quad (122)$$

It is obvious that in an isotropic sample both coefficients are zero, $f_\theta = f_\varphi = 0.0$, whereas in a homogeneous uniaxial sample we expect $f_\theta = 1.0$ and $f_\varphi = 0.0$ if all the chromophore long axes are oriented along the X direction. Similarly, for a sample of biaxial symmetry with a perfect orientation along the Y direction and the Z direction, we expect $f_\theta = -0.5$, $f_\varphi = 1.0$ and $f_\theta = +0.5$, $f_\varphi = -1.0$, respectively. Experimentally, it is easily checked on some selected infrared active modes that the orientation factor f_φ

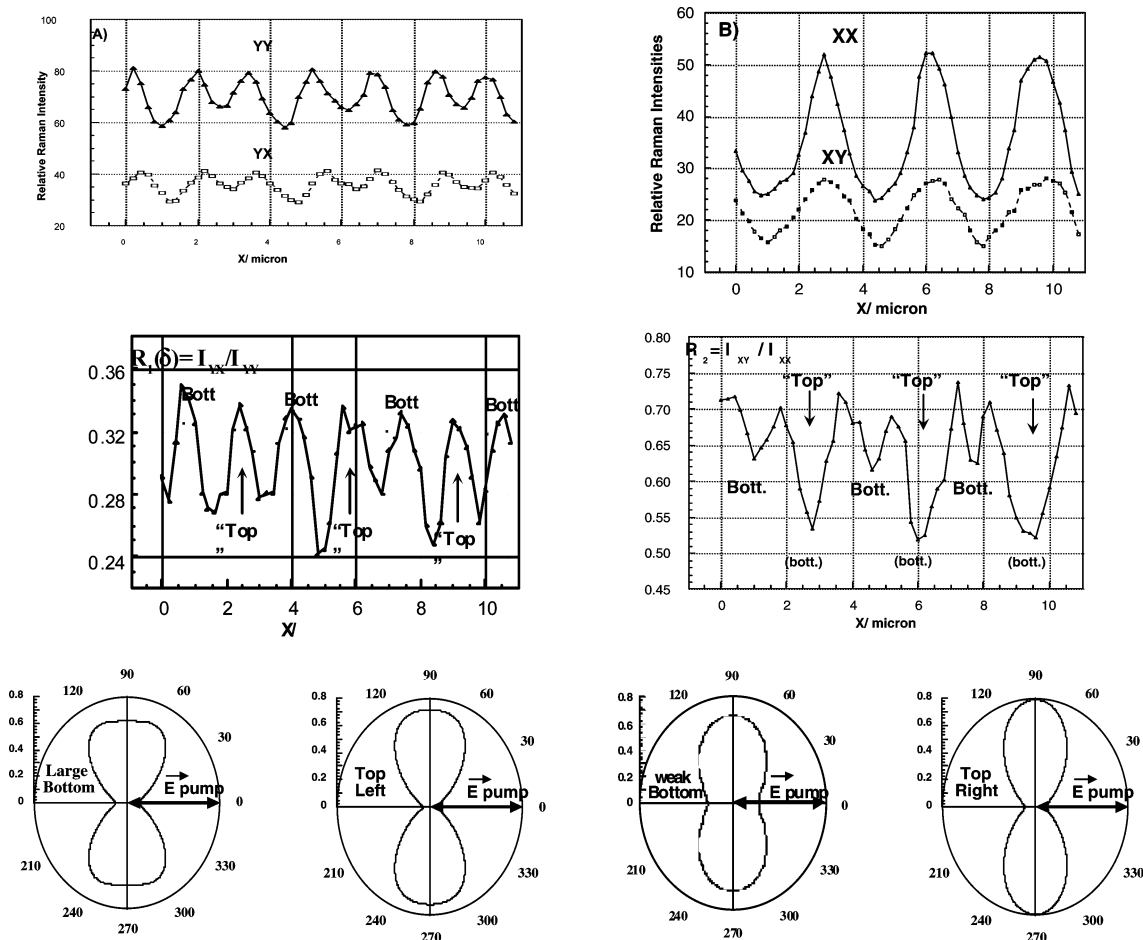


Figure 49. Main Raman results and shapes of the orientation distribution functions in a grating inscribed using the linear (p + p) polarization configuration. (Adapted from ref 58.)

differs from zero and that there exists a biaxial symmetry with a preferential in-plane (when f_φ is positive) or out of film-plane (when f_φ is negative) orientation.

Furthermore, according to the scattering geometries already defined in Figure 42 and to the general intensity equation (eq 107), in a first approximation the following expressions can be used in confocal micro-Raman experiments in order to get the two intensity ratios, R_1 and R_2 :

- (i) when the incident laser beam is polarized along the direction Y , one gets $R_1 = I_{YX}/I_{YY}$ using

$$\begin{aligned} I_{YX} &= (A\langle\alpha_{YX}^2\rangle + B\langle\alpha_{YZ}^2\rangle)(2C_0 + C_2) + \dots \\ I_{YY} &= (A\langle\alpha_{YY}^2\rangle + B\langle\alpha_{YZ}^2\rangle)(2C_0 + C_2) + \dots \end{aligned} \quad (123)$$

- (ii) when the laser beam is polarized along the direction X , one obtains $R_2 = I_{XY}/I_{XX}$ via

$$\begin{aligned} I_{XY} &= (A\langle\alpha_{XY}^2\rangle + B\langle\alpha_{XZ}^2\rangle)(2C_0 + C_2) + \dots \\ I_{XX} &= (A\langle\alpha_{XX}^2\rangle + B\langle\alpha_{XZ}^2\rangle)(2C_0 + C_2) + \dots \end{aligned} \quad (124)$$

It must be recalled that only the first terms (the more significant ones) are here above considered and that the averages of the squares of the tensor elements

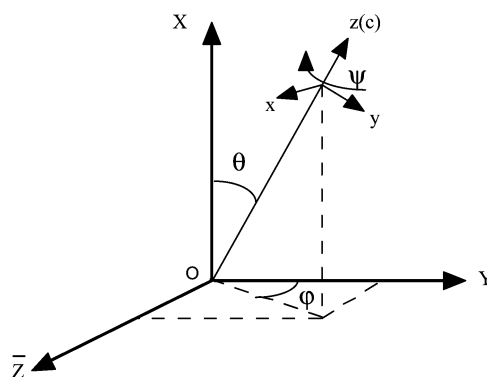


Figure 50. Definition of the Euler angles θ and φ with respect to the laboratory system axes (X , Y , Z).

are calculated from integrals over the various orientations:

$$\langle\alpha_{IJ}^2\rangle \approx \int_0^{2\pi} d\varphi \int_{-1}^{+1} d(\cos \theta) \langle\alpha_{IJ}^2 F(\cos \theta, \varphi)\rangle \quad (125)$$

For simplicity, we assume that the molecular polarizability tensor is diagonal, and because of the cylindrical symmetry of the chromophores and of resonance Raman conditions, we state also that $\alpha_3 \gg \alpha_1 = \alpha_2$. Under these conditions, the two ratios R_1 and R_2 in an anisotropic sample of biaxial symmetry depend not only on the two parameters A and B (functions of the sample refractive index and the NA objective lens) but also on the five coefficients or

Table 10. Values of the Intensity Ratios R_1 , R_2 and Main Orientation Factors in the $\nu_{8a}(\omega(\text{C}=\text{C}))$ and $\nu(\text{N}=\text{N})$ Vibrational Modes of a "P269" Film Sample of Biaxial Symmetry (Adapted from Ref 73)

mode ν/cm^{-1}	$f_{\theta} \equiv \langle F_{2,0} \rangle$	f_{φ}	$2f_{\varphi}(1-f_{\theta}) \equiv \langle F_{2,2} \rangle$ ($\langle P_{2,2,0} \rangle$)	R_1	R_2	$\langle F_{4,0} \rangle$	$\langle F_{4,2} \rangle$ ($\langle P_{4,2,0} \rangle$)	$\langle F_{4,4} \rangle$ ($\langle P_{4,4,0} \rangle$)
$\omega(\text{C}=\text{C})$ (8a) 1599 cm^{-1}	-0.304	+0.341	+0.889 (+0.074)	0.476	0.303	+0.085 \pm 0.027	+0.739 (+0.0041)	-56.80 (-0.034)
$\nu(\text{N}=\text{N})$ 1372 cm^{-1}	-0.321	+0.234	+0.642 (+0.053)	0.580	0.367	+0.094 \pm 0.030	+0.789 (+0.0044)	-91.99 (-0.055)
(infrared data)	(IR)	(IR)	(IR)	(R)	(R)	(R)	(R)	(R)
(Raman data)								

orientation factors, $\langle F_{l,m} \rangle$. After some tedious calculations,⁷³ we obtain the final equations:

$$R_1 = [7(A + B) + 5(A + B)\langle F_{2,0} \rangle - 12(A + B)\langle F_{4,0} \rangle - 2.5(A - B)\langle F_{2,2} \rangle - (A - B)\langle F_{4,2} \rangle] / [7(3A + B) + 5(12A + B)\langle F_{2,0} \rangle + 12(2A - B)\langle F_{4,0} \rangle + 2.5(B)\langle F_{2,2} \rangle + (B)\langle F_{4,2} \rangle] \quad (126)$$

$$R_2 = [7(A + B) + 5(A - 2B)\langle F_{2,0} \rangle - 3(4A - B)\langle F_{4,0} \rangle - 2.5(A)\langle F_{2,2} \rangle - (A)\langle F_{4,2} \rangle - 0.125(B)\langle F_{4,4} \rangle] / [7(3A + B) - 10(3A + B)\langle F_{2,0} \rangle + 3(3A + B)\langle F_{4,0} \rangle - 15(A)\langle F_{2,2} \rangle + (A)\langle F_{4,2} \rangle + 0.125(A - B)\langle F_{4,4} \rangle] \quad (127)$$

Any biaxial systems may then be treated using these expressions for the intensity ratios. However, it is obvious that we cannot estimate values of the five orientation factors from only polarized backscattering Raman experiments. We are thus forced to combine FTIR and Raman results in order to determine all the orientation factors and to establish a complete distribution function.

Actually, two sets of polarized micro-Raman spectra were recorded in the backscattering geometry on a "P269" anisotropic film, namely the $Z(YX)\bar{Z}$ and $Z(YY)\bar{Z}$ spectra to determine R_1 and the $Z(XY)\bar{Z}$ and $Z(XX)\bar{Z}$ spectra to determine R_2 . Experimentally, to avoid any photobleaching or photodegradation effects, we have employed the 752.5 nm red line of a Kr^+ laser with a very weak intensity (0.1–0.2 mW) in conjunction with a wide angle (100X) objective lens. Typical polarized Raman results for an anisotropic film sample are reported in Figure 51. The corresponding values obtained for the intensity ratios and the main orientation factors in two selected vibrational modes are given in Table 10.

In fact, to get estimates of all the orientation factors, we have applied the following procedure: the two coefficients $\langle F_{2,0} \rangle$ and $\langle F_{2,2} \rangle$, respectively equal to f_{θ} and to $2f_{\varphi}(1 - f_{\theta})$, are first determined from infrared results. Then, we adjust the next coefficient $\langle F_{4,0} \rangle$ to its corresponding mean value in the domain of existence of the most probable distributions of Gaussian type in a related uniaxial system (see section 3.2.3). Then, from the knowledge of the A and B optical parameters (calculated from the objective NA and the mean refractive index of the sample), the coefficient $\langle F_{4,2} \rangle$ is calculated directly from the former equation (eq 126) and, consequently, the last coefficient $\langle F_{4,4} \rangle$ is estimated from the latter equation (eq 127).

It must be pointed out that it is mandatory to find physically meaningful values for all the coefficients. In this respect, a simple check is provided by the

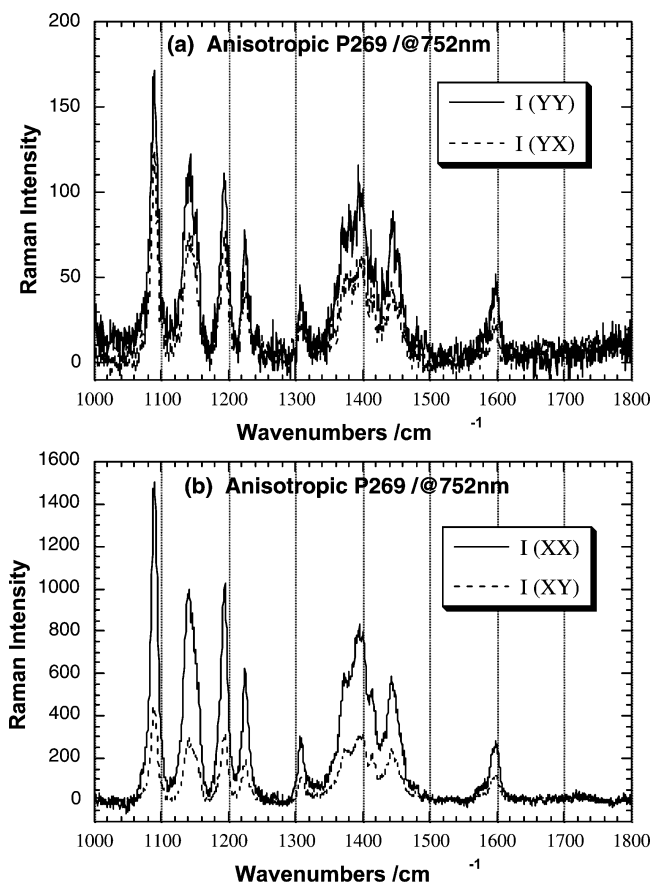


Figure 51. Polarized (a) $Z(YY)\bar{Z}$, $Z(YX)\bar{Z}$ and (b) $Z(XX)\bar{Z}$, $Z(XY)\bar{Z}$ micro-Raman spectra of an anisotropic "P269" film sample. (Adapted from ref 73.)

following inequalities which must be strictly fulfilled:¹³

$$|\langle P_{4,2,0} \rangle| = \frac{1}{180} |\langle F_{4,2,0} \rangle| \leq \frac{3}{56} \quad \text{and} \quad |\langle P_{4,4,0} \rangle| = \frac{1}{1680} |\langle F_{4,4,0} \rangle| \leq \frac{1}{16} \quad (128)$$

Finally, from the knowledge of the five orientation factors and the assumption of a probable azimuthal angle $\varphi = 40^\circ$ (estimated from eq 120), we have established the more likely and physically reasonable orientation distribution functions of some selected vibrational modes. The related result obtained for the $\omega(\text{C}=\text{C})$ ring stretching mode at 1599 cm^{-1} is shown in Figure 52; as expected, the calculated distribution function is always positive, whatever the polar angle θ considered.

In conclusion, we have shown that, from a proper combination of infrared dichroism and polarized micro-Raman measurements, it is possible to afford new relevant information about the molecular sym-

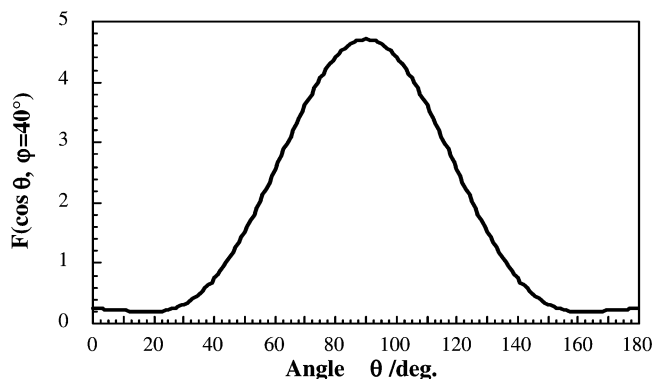


Figure 52. Final distribution function calculated for the $\omega(\text{C}=\text{C})$ mode at 1599 cm^{-1} using the orientation factors $\langle P_{2,0,0} \rangle$, $\langle P_{4,0,0} \rangle$, $\langle P_{2,2,0} \rangle$, $\langle P_{4,2,0} \rangle$, and $\langle P_{4,4,0} \rangle$ equal to -0.304 , $+0.085$, $+0.074$, $+0.004$, and -0.034 , respectively. (Adapted from ref 73.)

metry properties and about the chromophore orientation distribution function in an anisotropic, strongly absorbing polymer film. Nevertheless, this spectroscopic approach is limited and can be applied only to systems of either uniaxial symmetry or simple biaxial symmetry. Moreover, it is worth recalling that great attention must be paid in carrying out such investigations, not only in the recording of the different spectra but also in performing the different analyses and data treatments.

5. Acknowledgments

The author would like to warmly acknowledge all the collaborators who have participated in the experiments, data treatments, and interpretations of the numerous laboratory results described in this manuscript, in particular F. Lagugné-Labarthe, T. Buffeteau, R. Cavagnat, J. L. Bruneel, M. Huber (from Bayreuth University), P. Maraval, and D. Talaga. Also, many thanks are due to J. C. Lassègues for a critical reading of the first version of this article and to a reviewer who suggested numerous relevant corrections to improve the English style and the quality of the whole manuscript. The author is also thankful to M. Dumont (ENS-Cachan, France) and M. Pézolet (Université Laval, Québec) for many fruitful discussions and to Drs. S. Kostromine and T. Bieringer (Central Research Department, Bayer AG, Leverkusen, Germany) for a gift of several azopolymer systems and for the common studies carried out in a collaboration agreement. Finally, the author must emphasize that the financial supports from the CNRS (Chemistry Department) and from the "Région Aquitaine" (France) were always welcome and are gratefully acknowledged.

6. Appendix: Mathematical Expressions for the $P_{l00}(\cos \theta)$ and $P_{lm0}(\cos \theta)$ Type Legendre Polynomials and Orientation Factors

According to eqs 35 and 36, we report here the usual expressions of some orientational order parameters generally encountered in uniaxial and biaxial symmetry systems.

$$(i) \text{ For } P_l^0(\cos \theta) = P_{l00}(\cos \theta)$$

$$P_0^0(\cos \theta) = P_{000}(\cos \theta) = 1.0$$

$$P_1^0(\cos \theta) = P_{100}(\cos \theta) = \cos \theta$$

$$P_2^0(\cos \theta) = P_{200}(\cos \theta) = \frac{1}{2}(3 \cos^2 \theta - 1)$$

$$P_3^0(\cos \theta) = P_{300}(\cos \theta) = \frac{1}{2}(5 \cos^3 \theta - 3 \cos \theta)$$

$$P_4^0(\cos \theta) = P_{400}(\cos \theta) = \frac{1}{8}(35 \cos^4 \theta - 30 \cos^2 \theta + 3) \dots$$

$$(ii) \text{ For } P_l^{|m|}(\cos \theta) = P_{lm0}(\cos \theta) \text{ for } |m| \leq l$$

(averaged over the ψ angle)

$$P_1^1(\cos \theta) = P_{110}(\cos \theta) = \sin \theta$$

$$P_2^2(\cos \theta) = P_{220}(\cos \theta) = 3 \sin^2 \theta = \frac{3}{2}(1 - \cos 2\theta)$$

$$P_3^1(\cos \theta) = P_{310}(\cos \theta) = \frac{3}{2}(5 \cos^2 \theta - 1) \sin \theta = \frac{3}{8}(\sin \theta + 5 \sin 3\theta)$$

$$P_3^3(\cos \theta) = P_{330}(\cos \theta) = 15 \sin^3 \theta = \frac{15}{4}(3 \sin \theta - \sin 3\theta)$$

$$P_4^2(\cos \theta) = P_{420}(\cos \theta) = \frac{15}{2}(7 \cos^2 \theta - 1) \sin^2 \theta$$

$$P_4^4(\cos \theta) = P_{440}(\cos \theta) = 105 \sin^4 \theta \dots$$

7. References

- (1) Placzek, G. In *Handbuch der Radiologie*; Marx, E., Ed.; Akad. Verlag: Leipzig, 1934; Vol. VI-2, p 205.
- (2) Long, D. A. *Raman spectroscopy*; McGraw-Hill: New York, 1977.
- (3) *The Raman Effect: a unified treatment of the theory of Raman scattering by molecules*; John Wiley: Chichester, U.K., 2002.
- (4) Clark, R. J. H.; Stewart, B. *Struct. Bonding* **1979**, *36*, 1.
- (5) Turrell, G. In *Practical Raman Spectroscopy*; Gardiner, D. J., Graves, P. R., Eds.; Springer-Verlag: Berlin, 1989; p 13.
- (6) Fano, U.; Racah, G. *Irreducible tensorial sets*; Academic Press: New York, 1959.
- (7) Pézolet, M.; Nafie, L. A.; Petitcolas, W. L. *J. Raman Spectrosc.* **1973**, *1*, 455.
- (8) Nestor, J.; Spiro, T. J. *J. Raman Spectrosc.* **1973**, *1*, 539.
- (9) Roe, R. J.; Krigbaum, W. R. *J. Chem. Phys.* **1964**, *40*, 2608; *J. Appl. Phys.* **1964**, *35*, 2215.
- (10) Roe, R. J. *J. Appl. Phys.* **1965**, *36*, 2024.
- (11) Bower, D. I. *J. Polym. Sci., Polym. Phys. Ed.* **1972**, *10*, 2135.
- (12) Jarvis, D. A.; Hutchinson, I. J.; Bower, D. I.; Ward, I. M. *Polymer* **1980**, *21*, 41.
- (13) Bower, D. I. *J. Polym. Sci., Polym. Phys. Ed.* **1981**, *19*, 93.
- (14) Ward, I. M. *Advances in Polymer Science*; Springer-Verlag: Berlin, 1985; Vol. 66, p 81.
- (15) Ikeda, R.; Chase, B.; Everall, N. In *Handbook of Vibrational Spectroscopy*; Chalmers, J. M., Griffiths, P. R., Eds.; John Wiley: Chichester, U.K., 2002; Vol. 1, p 716.
- (16) Nomura, S.; Kawai, H. *J. Polym. Sci., A-2* **1970**, *8*, 383.
- (17) Kaito, A.; Nakayama, K.; Kanetsuna, H. *J. Macromol. Sci., Phys.* **1987**, *B26*, 281.
- (18) Lagugné-Labarthe, F.; Sourisseau, C. *J. Raman Spectrosc.* **1996**, *27*, 491.
- (19) Lagugné-Labarthe, F.; Buffeteau, T.; Sourisseau, C. *J. Phys. Chem. B* **1998**, *102*, 5754.
- (20) Lagugné-Labarthe, F.; Buffeteau, T.; Sourisseau, C. *Macromol. Symp.* **1999**, *139*, 75.
- (21) Buffeteau, T.; Pézolet, M. *Appl. Spectrosc.* **1996**, *50*, 948; private communication.

- (21) Pigeon, M.; Prud'homme, R. E.; Pézolet, M. *Macromolecules* **1991**, *24*, 5687.
- (22) Gordeyev, S. A.; Nikolaeva, G. Y.; Prokhorov, K. A. (a) *Laser Physics* **1996**, *6*, 121; **1999**, *9*, 955. (b) *Polym. Sci., Ser. A* **1996**, *38*, 517; *Polym. Sci., Ser. B* **1998**, *40*, 348; *Polym. Sci., Ser. B* **1999**, *41*, 74. (c) *Macromol. Symp.* **2002**, *184*, 123.
- (23) Berne, B. J.; Pechukas, P.; Harp, G. D. *J. Chem. Phys.* **1968**, *46*, 3125.
- (24) Pottel, H.; Herreman, W.; Van der Meer, B. W.; Ameloot, M. *Chem. Phys.* **1986**, *102*, 37.
- (25) Lagugné-Labarthe, F.; Buffeteau, T.; Sourisseau, C. *Appl. Spectrosc.* **2000**, *54*, 699.
- (26) Nobbs, J. H.; Bower, D. I.; Ward, I. M. *J. Polym. Sci., Polym. Phys. Ed.* **1979**, *17*, 259.
- (27) Raha, S.; Bowden, P. B. *Polymer* **1972**, *13*, 174.
- (28) Archer, L. A.; Fuller, G. G.; Nunneley, L. (a) *Polymer* **1972**, *13*, 174; (b) *Macromolecules* **1994**, *27*, 4359.
- (29) Everall, N.; Chalmers, J.; Mills, P. *Appl. Spectrosc.* **1996**, *50*, 1229.
- (30) Voyiatzis, G. A.; Petekidis, G.; Vlassopoulos, D.; Kamitsos, E. I.; Bruggeman, A. *Macromolecules* **1996**, *29*, 2244.
- (31) Deimede, V.; Andrikopoulos, K. S.; Voyiatzis, G. A.; Konstantakopoulou, F.; Kallitsis, J. K. *Macromolecules* **1999**, *32*, 8848.
- (32) Voyiatzis, G. A.; Andrikopoulos, K. S.; Papatheodorou, G. N.; Kamitsos, E. I.; Chryssikos, G. D.; Kapoutsis, J. A.; Anastasiadis, S. H.; Fytas, G. *Macromolecules* **2000**, *33*, 5613.
- (33) Voyiatzis, G. A.; Andrikopoulos, K. S. *Appl. Spectrosc.* **2002**, *56*, 528.
- (34) Paradkar, R. P.; Sakhalkar, S. S.; He, X.; Ellison, M. S. *Appl. Spectrosc.* **2001**, *55*, 534.
- (35) Turrell, G.; Delhaye, M.; Dhamelincourt, P. In *Raman Microscopy: developments and applications*; Turrell, G., Corset, J., Eds.; Academic Press: London, 1996; p 27.
- (36) Delhaye, M.; Dhamelincourt, P. *J. Raman Spectrosc.* **1975**, *3*, 33.
- (37) Rosasco, G. J.; Roeder, E.; Simmons, J. H. *Science* **1975**, *190*, 5557.
- (38) Sourisseau, C.; Maraval, P. *Appl. Spectrosc.* **2003**, *57*, 1324.
- (39) Laureyns, J. Thèse de doctorat (Ph.D.), Université Lille (France), 1987.
- (40) Gard, P.; Cruège, F.; Sourisseau, C.; Gorochoy, O. *J. Raman Spectrosc.* **1986**, *17*, 283.
- (41) Pallister, D. M.; Liu, K. L.; Govil, A.; Morris, M. D.; Owen, H.; Harrison, T. R. *Appl. Spectrosc.* **1992**, *46*, 1469.
- (42) Dilor, S. A. *Technical data Jobin-Yvon (France)*; Internal technical note from Dilor (Lille, France); 1992; T06, T21.
- (43) Brémard, C.; Laureyns, J.; Merlin, J. C.; Turrell, G. *J. Raman Spectrosc.* **1987**, *18*, 305.
- (44) Turrell, G. *J. Raman Spectrosc.* **1984**, *15*, 103.
- (45) Richards, B.; Wolf, E. *Proc. R. Soc. London, Ser. A* **1959**, *253*, 358.
- (46) Török, P.; Varga, P.; Booker, G. R. *J. Opt. Soc. Am. A* **1995**, *12*, 2136.
- (47) Bruneel, J. L.; Lassègues, J. C.; Sourisseau, C. *J. Raman Spectrosc.* **2002**, *33*, 815.
- (48) Dilor, S. A. *Technical data Jobin-Yvon (France)*; Internal technical note from Dilor (Lille, France); Confocal laser Raman; 1990.
- (49) Tabaksblat, R.; Meier, R. J.; Kip, B. J. *Appl. Spectrosc.* **1992**, *46*, 60.
- (50) Everall, N. J. *Appl. Spectrosc.* **2000**, *54*, 773.
- (51) Everall, N. J. *Appl. Spectrosc.* **2000**, *54*, 1515.
- (52) Baldwin, K. J.; Batchelder, D. N. *Appl. Spectrosc.* **2001**, *55*, 517.
- (53) Baia, L.; Gigant, K.; Posset, U.; Schottner, G.; Kiefer, W.; Popp, J. *Appl. Spectrosc.* **2002**, *56*, 536.
- (54) Baia, L.; Gigant, K.; Posset, U.; Petry, R.; Schottner, G.; Kiefer, W.; Popp, J. *Vib. Spectrosc.* **2002**, *29*, 245.
- (55) Campos, F. J.; Mestres, N.; Pascual, J.; Brink, D. J.; Camassel, J. *Proceedings of ANRT Raman Meeting* (private communication from the authors); Montpellier, France, 2001.
- (56) Lagugné-Labarthe, F.; Buffeteau, T.; Sourisseau, C. *J. Phys. Chem. B* **1998**, *102*, 2654.
- (57) Lagugné-Labarthe, F.; Buffeteau, T.; Sourisseau, C. *J. Phys. Chem. B* **1999**, *103*, 6690.
- (58) Lagugné-Labarthe, F.; Bruneel, J. L.; Buffeteau, T.; Sourisseau, C.; Huber, M.; Zilker, S. J.; Bieringer, T. *Phys. Chem. Chem. Phys.* **2000**, *2*, 5154.
- (59) Lagugné-Labarthe, F.; Bruneel, J. L.; Sourisseau, C.; Huber, M.; Börger, V.; Menzel, H. *J. Raman Spectrosc.* **2001**, *32*, 665.
- (60) Lagugné-Labarthe, F.; Buffeteau, T.; Sourisseau, C. *J. Appl. Phys.* **2001**, *90*, 2149.
- (61) Lagugné-Labarthe, F.; Buffeteau, T.; Sourisseau, C. *Appl. Phys. B* **2002**, *74*, 129.
- (62) Lagugné-Labarthe, F.; Buffeteau, T.; Sourisseau, C. *Phys. Chem. Chem. Phys.* **2002**, *4*, 4020.
- (63) Lagugné-Labarthe, F.; Buffeteau, T.; Sourisseau, C. *J. Opt. A: Pure Appl. Opt.* **2002**, *4*, S235.
- (64) Lefin, P.; Fiorini, C.; Nunzi, J. M. *Pure Appl. Opt.* **1968**, *7*, 71.
- (65) Barrett, J. C.; Natansohn, A. L.; Rochon, P. L. *J. Phys. Chem. B* **1996**, *100*, 8836.
- (66) Barrett, J. C.; Rochon, P. L.; Natansohn, A. L. *J. Chem. Phys.* **1998**, *109*, 1505.
- (67) Zilker, S. J.; Bieringer, T.; Haarer, D.; Stein, R. S.; Van Egmond, J. W.; Kostromine, S. G. *Adv. Mater.* **1998**, *10*, 855.
- (68) Zilker, S. J.; Huber, M. R.; Bieringer, T.; Haarer, D. *Appl. Phys. B* **1999**, *68*, 893.
- (69) Cimrova, V.; Neher, D.; Kostromine, S.; Bieringer, T. *Macromolecules* **1999**, *32*, 8496.
- (70) Lagugné-Labarthe, F.; Bruneel, J. L.; Rodriguez, V.; Sourisseau, C. *J. Phys. Chem. B* **2004**, *108*, 1264.
- (71) Buffeteau, T.; Pézolet, M. *Macromolecules* **1998**, *31*, 2631.
- (72) Sabi, Y.; Yamamoto, M.; Watanabe, H.; Bieringer, T.; Haarer, D.; Hagen, R.; Kostromine, S.; Berneth, H. *Jpn. J. Appl. Phys.* **2001**, *40*, 1613.
- (73) Buffeteau, T.; Lagugné-Labarthe, F.; Sourisseau, C.; Kostromine, S.; Bieringer, T. *Macromolecules* **2004**, *37*, 2880.

CR030042G

